

# Nonlinear Instability and Turbulence Suppression in Stratified Flows

A Thesis

Submitted to the  
Tata Institute of Fundamental Research, Mumbai  
for the degree of Doctor of Philosophy  
in Physics

by

Ritabrata Thakur

International Centre for Theoretical Sciences  
Tata Institute of Fundamental Research  
Bengaluru, Karnataka

August 2020  
Final Version Submitted in November, 2020



## DECLARATION

This thesis is a presentation of my original research work. Wherever contributions of others are involved, every effort is made to indicate this clearly, with due reference to the literature, and acknowledgement of collaborative research and discussions.

The work was done under the guidance of Professor Rama Govindarajan at the International Centre for Theoretical Sciences, Bengaluru.



Ritabrata Thakur

In my capacity as supervisor of the candidate's thesis, I certify that the above statements are true to the best of my knowledge.



Rama Govindarajan

4 Aug 2020

Date:

To *Maa*, *Deuta*, Babu, and Dimpy.

# Acknowledgements

This thesis would not have been possible without the unwavering support of my advisor, Prof Rama Govindarajan. I owe a major part of my PhD to my advisor and ICTS who provided all the guidance and exposure I could ask for and helped me financially and with computational resources during my research works. It has been a pleasure working in Rama's group, where I got to learn a lot during productive group meetings. One of the best things about this group is that most people do varied things and this allows for opportunities to learn many different things during discussion meetings. Rama's ability to break down complex problems to the simplest possible case and then working backwards is what I have come to admire very much and will try to implement in my works. Her critical comments have helped shape this thesis. I thank Profs Debasis Sengupta, Vishal Vasan, and Amit Apte, who were the members of my thesis committee, and over the years gave their invaluable suggestions and critical feedback on my work. I also thank the Indian Ministry of Earth Sciences and Department of Atomic Energy for financial support during my PhD through the Ocean Mixing and Monsoon program. I am also thankful to the Indian Institute of Science and the Infosys Foundation for supporting some of my travels for collaborations and conferences.

My admission into a TIFR Physics program would not have been possible without the liberal ideas of the director and deans of Centre for Interdisciplinary Sciences (TCIS) in Hyderabad to admit and support students from different backgrounds other than Physics. TCIS is where I started my PhD and transferred to ICTS after two years of course works. Specifically, I am indebted to Prof Sriram Ramaswamy, the then director of TCIS, Rama, and the members of my selection committee. My transfer to ICTS would not have been possible without the support of my advisor Rama and director Professor Rajesh Gopakumar.

Prof Emily Shroyer has been a collaborator for about four years now. She has ensured her calm, unwavering, ever enthusiastic and happy response at every single online work discussion. She had also hosted me several times in Oregon State University, and I am thankful for the financial help and computational resources while at OSU. I am also thankful to Profs James Moum and Jonathan Nash who let us use  $\chi$ pod data in our study. I am happy to have had many engaging scientific discussions with Vishal. Rama, Emily, and Debasis had made it possible for me to go on research cruises into the Bay of Bengal to learn oceanographic data collection, and some of that data is used in one half of this thesis. Experimenting in the middle of the ocean is quite a unique learning experience.

My parents, fiancée Akhyarika, brother Subrata, and cousin Sudhakar have been my backbone through thick and thin. My foray into Physics from engineering would not have been possible without the support of my family. Akhyarika made sure that she would provide her best support, care, and love every single moment I needed, and talked me out of difficult times. I owe most of my stability during these PhD years to my family and Akhyarika as they never lost faith in me and I could turn to them every time I needed. I am thankful to my school and college teachers, specifically Drs. Bhoop Singh, K.M Pandey, A. Biswas, Subrat Barik, D.H. Das, and late Satish Thakur for their support. Due to the unfortunate covid-19 pandemic, I had to work from home for the last five

months, and this would not have been possible without the warm support of my family and of course the exceptional internet service of Jio India. Through this thesis, I offer my sincere gratitude to all the doctors, nurses, scientists, and other frontline members of this fight against covid-19 who are toiling to bring back life to normalcy as soon as possible putting their own lives at risk. As I gear up to submit my thesis, I remember my grandfather who passed a long time ago but had been my best friend since my childhood and would support every endeavour of mine. My grandmother passed away just a couple of months ago, and I am sure she would have been elated to hear that I am at the final stage of my thesis. It is a blessing to have such a supportive family.

My friends had a very positive influence on me during my PhD tenure. Ganga, Pranav and I shared a flat in Bangalore for quite a long time and it had been quite a unique learning experience. I could collaborate with Arjun for about two years now to develop the fluid flow solver, and hopefully, this continues to produce interesting results. Only due to his ever-optimistic outlook I could get past times where I almost made myself believe that I could not make the solver work. Nilanjan and Amitakhya, who have been friends since my school days, taught me how to live the other aspects of life despite work pressure. Our long drives to exotic places, where we covered a significant part of the beautiful Indian South, will remain in memory for long. Dipanjan and Sree Lekha helped my foray into oceanography as I could turn to them with even the silliest of doubts. On the other hand, Jose helped me during my transition to fluid stability and numerical techniques of fluid flow with his ever-helpful comments and suggestions. Rahul Chajwa has been a good friend, tea- and walk-buddy. I would also like to thank Varun, Adhip, Hemanta, Sunil, and Priyanka for engaging and funny discussions over lunch and dinner at the beautiful ICTS canteen. I am thankful to Arjun, Priyanka, and Deepak for willing to have a look at my thesis chapters and their critical comments. Some part of my PhD was spent in TCIS Hyderabad and I remember fondly the good times with my close friends Indrajit, JK, Dheeraj, Jishan, Ryan, Subhendu, Debdeep, Sudeshna, Manohar, Raju, and Roshan. I had also worked in the “surface science & interface engineering” laboratory of Prof T N Narayanan and I am thankful for that opportunity.

The administration and the IT cell of ICTS have been phenomenal to work with. I have to specifically mention the names of Prashanth and Hemanta who made super-computing so much easier at ICTS. The beautiful campus of ICTS in the outskirts of Bangalore has been an amazing place to work, learn, and play (the beautiful swimming pool deserves a special mention). Apart from an excellent peer group, one of its other highlights is the culture of discussion meetings and schools that try to bring the best of the world’s minds to ICTS to engage with students and ignite collaborations. I could also be a part of its outreach group which was quite fun and I thank Anupam and others for the opportunity. I am also thankful to Jeeva, Basavaraj, and Suresh for helping me out in many different occasions. Bangalore as a whole act as a nice scientific hub with some very good research institutes.

At last, this thesis is a product of invaluable inputs from my advisor and a long list of helpful and caring collaborators, friends, and colleagues, and unwavering support of my family. I offer my sincere gratitude to all of them. I wish for a speedy recovery of humankind from the covid-19 pandemic.

## List of publications

1. **Ritabrata Thakur**, Emily L. Shroyer, Rama Govindarajan, J. Thomas Farrar, Robert A. Weller, and James N. Moum. “Seasonality and buoyancy suppression of turbulence in the Bay of Bengal.” *Geophysical Research Letters* 46.8 (2019): 4346-4355.
2. **Ritabrata Thakur\***, Arjun Sharma\*, and Rama Govindarajan. “Early evolution of optimal perturbations in a viscosity-stratified channel”. Under review (\* equal contribution). <https://arxiv.org/abs/2007.03628>
3. **Ritabrata Thakur**, Emily L. Shroyer, Rama Govindarajan, and James N. Moum. “Evidence of month-long diurnal turbulence in the Bay of Bengal”. (work in progress)

# Contents

\*\*\*

<b>1</b>	<b>Introduction</b>	<b>1</b>
1.1	Transition to turbulence . . . . .	1
1.2	Fluid stability . . . . .	2
1.2.1	Energy growth of disturbances . . . . .	3
1.3	Viscosity variations . . . . .	8
1.4	Earth's oceans . . . . .	9
1.5	Methods of Ocean Observation . . . . .	10
1.5.1	Oceanographic mooring . . . . .	11
1.5.2	Research expeditions to the Bay of Bengal . . . . .	12
1.6	Some properties of oceanic flows . . . . .	14
1.7	Bay of Bengal and Indian monsoon . . . . .	16
1.7.1	Ocean-Atmosphere coupling in Indian ocean . . . . .	16
1.8	Ocean Turbulence . . . . .	17
1.8.1	Need for parametrisation . . . . .	18
1.9	Outline of the thesis . . . . .	19
<b>2</b>	<b>Nonlinear instability and numerics</b>	<b>21</b>
2.1	Introduction . . . . .	21
2.2	Modal stability analysis . . . . .	22
2.3	Nonmodal stability analysis . . . . .	25
2.4	Dynamical systems approach to fluid flow . . . . .	29
2.5	Definition of adjoints . . . . .	29
2.6	Variational method of nonmodal analysis . . . . .	30

2.6.1	Application to the Navier-Stokes equations . . . . .	31
2.7	Adjoint Equations . . . . .	36
2.7.1	Looping algorithm for Navier-Stokes . . . . .	38
2.7.2	Change in cost functional . . . . .	39
2.8	Optimisation . . . . .	39
2.8.1	Trusting the optimal . . . . .	43
2.9	Numerical method . . . . .	44
2.9.1	Homogeneous directions . . . . .	45
2.9.2	Wall normal direction . . . . .	45
2.9.3	Temporal Discretisation . . . . .	46
2.9.4	Run-time of the code . . . . .	48
2.9.5	Parallel processing using OpenMP . . . . .	49
2.10	Outputs: optimal structures . . . . .	50
2.11	Validation . . . . .	54
2.11.1	Linear validation . . . . .	54
2.11.2	Nonlinear validation . . . . .	55
<b>3</b>	<b>Viscosity-stratified optimal perturbations</b>	<b>58</b>
3.1	Introduction . . . . .	59
3.2	Governing equations and problem formulation . . . . .	61
3.2.1	Viscosity model and the base state . . . . .	64
3.2.2	The Reynolds number . . . . .	65
3.2.3	Direct-adjoint looping . . . . .	65
3.3	Evolution of stratified optimal perturbations . . . . .	69
3.3.1	The linear optimal and its evolution . . . . .	69
3.3.2	The non-linear optimal perturbation and its evolution . . . . .	76
3.3.3	Effect of Prandtl number . . . . .	87
3.4	Conclusions . . . . .	88
<b>4</b>	<b>Ocean turbulence with <math>\chi</math>pods</b>	<b>90</b>
4.1	Introduction . . . . .	90
4.2	$\chi$ pods . . . . .	91
4.3	Theoretical principles . . . . .	93

4.3.1	Mixing efficiency $\Gamma$ . . . . .	95
4.3.2	Spectrum of turbulence . . . . .	96
4.4	Iterative procedure to calculate $\chi$ . . . . .	98
4.4.1	Temperature fluctuations . . . . .	102
4.4.2	Speed past thermistor . . . . .	103
<b>5</b>	<b>Seasonality and suppression of turbulence</b>	<b>106</b>
5.1	Introduction . . . . .	107
5.2	Data and Methods . . . . .	109
5.3	Results from the Bay of Bengal . . . . .	110
5.4	Observed Upper-Ocean Turbulence . . . . .	114
5.4.1	Seasonality in Turbulence Near the Base of the Mixed Layer . . . . .	120
5.4.2	Seasonality in Turbulence Below the Mixed Layer . . . . .	120
5.5	Buoyancy Suppression of Turbulence . . . . .	122
5.6	Conclusions . . . . .	124
5.7	Appendix . . . . .	125
5.7.1	Wavelet Transforms . . . . .	125
5.7.2	Accessing the dataset . . . . .	126
<b>6</b>	<b>A diurnal signal in turbulence</b>	<b>127</b>
6.1	Introduction . . . . .	128
6.2	Diurnal turbulence in the Bay of Bengal . . . . .	130
6.3	Periodicity in the winds . . . . .	138
6.4	Why this diurnal turbulence? . . . . .	139
6.4.1	Convective origin of mixing . . . . .	140
6.4.2	Tidal mixing . . . . .	141
6.4.3	Biogenically-forced mixing . . . . .	143
6.4.4	Wind-induced shear mixing . . . . .	144
6.5	Attempt at MITgcm modelling . . . . .	146
6.6	Conclusions . . . . .	149
<b>7</b>	<b>Conclusions</b>	<b>151</b>
7.1	Future directions . . . . .	153

# Introduction

\*\*\*

This thesis consists of two distinct areas of work, and is divided into five chapters. The first half of the thesis is a theoretical and numerical investigation of nonlinear nonmodal analysis of fluid flow. The second half is concerned with measurements and analysis of geophysical turbulence in the Bay of Bengal. The first half was motivated by observations in the Bay of Bengal, and future work will be aimed at connecting the two studies, as described at the end of this chapter. This chapter gives a general background on the areas of work connected to this thesis.

## 1.1 Transition to turbulence

The transition of a flow from a laminar to turbulent state has been an age-old problem, studied ever since Reynolds (1883) investigated ‘sinuous’ motion of fluids and the transition to same from a ‘straight’ (or laminar) flow. Turbulence is characterised by the existence of vortical motions (eddies) of different sizes, ranging from the size at which energy is imparted into the flow to the size at which dissipation by molecular action happens. The transition from a laminar to a turbulent state typically occurs when the Reynolds number ( $Re$ ), (which is a ratio of inertial to viscous forces), is increased beyond a certain value. We define a critical Reynolds number  $Re_{cr}$  as one below which all small (linear) normal mode perturbations decay exponentially. Shear flows, under certain conditions, display a supercritical transition, where transition to turbulence occurs beyond, even well above,  $Re_{cr}$ . But often in shear flows, the transition from laminar flow to turbulence is subcritical, in that it occurs below  $Re_{cr}$ , but above an energy critical

Reynolds number  $Re_E$ , defined as the Reynolds number below which the total energy in any general perturbation will decay monotonically. In a subcritical transition, thus, both laminar and the turbulent states of the flow can coexist as equilibrium solutions between  $Re_{cr}$  and  $Re_E$ . For certain wall-bounded shear flows,  $Re_{cr}$  is infinite, i.e., the flow is stable to small disturbances at every Reynolds number, e.g., the flow between two infinite and parallel sheared plates (called Couette flow), or flow through straight pipes. However, depending on the type of the flow and the exact definition of the Reynolds number, these flows transition to turbulence somewhere between  $Re \sim \mathcal{O}(100 - 1000)$ , and this transition a spatio-temporal process (Barkley, 2016).

## 1.2 Fluid stability

Studying the stability of flow provides understanding about its possibility to undergo a transition to turbulence or its propensity to continue in the laminar state. Transition is initiated when disturbances are imposed over the flow. This can either be ambient noise or perturbations due to the set-up of an experiment, or numerical disturbances in a simulated flow, either injected deliberately or in the form of numerical round-off errors. The stability study of a system when the disturbances are of infinitesimal amplitude is called linear stability analysis (Kelvin, 1887; Rayleigh, 1880). When the amplitude of disturbances is large, a nonlinear stability analysis would become appropriate. A quantity of interest here could be the evolution of some measure of the amplitude of the disturbances to the flow. A natural choice is the square of the perturbation amplitude, which is often a measure of the energy in the disturbances. So, in our stability study, we wish to ascertain how much energy growth in the disturbances can occur within a certain period of time. A natural follow-up question would be whether that growth in energy is capable of triggering a transition to turbulence, but that question is beyond the scope of this thesis, and constitutes our next planned study.

Every disturbance to the flow can be decomposed into a combination of modes. Linear stability analysis, as noted, is concerned with infinitesimal amplitude disturbances, and often examining the behaviour of individual modes. By the very definition of stability, we are looking for the response of a system to being perturbed away from an equilibrium state. In our case, the equilibrium state is the laminar base flow. We can understand

this growth using a cartoon of flow between two steady and infinite parallel walls as in figure 1.1. A disturbance (in red) is imposed on the base flow of the system which has a magnitude  $u$  at the centerline. As noted, this perturbation has origins in experimental or numerical noise. The base state shown in black line in figure 1.1 (I) is the laminar state of the flow. This combination of the base flow and the perturbation can evolve in time to either of two cases: figure 1.1 (II) or (III). When the perturbation cannot survive and dies down from its initial magnitude, we have case II where the flow has settled to its base state or the laminar state. In an alternative situation, the perturbation could grow in magnitude. This happens when the perturbations extract energy from the base or laminar state of the flow. In figure 1.1 (III), we can see this alternative happening. When the perturbations grow in magnitude, the mean velocity magnitude shrinks (i.e., the value of  $u$  in (III) is less than that in (II)) and the mean profile of the flow is much flatter as compared to the original laminar profile between the two walls. What has been described with this cartoon is a very crude version of transition to turbulence in flow between two parallel walls driven by a pressure gradient, called a channel flow. Case (II) presents a scenario when the flow did not transition and settled back to its original laminar state while case (III) is a transition scenario with the flow becoming turbulent and the perturbations growing in magnitude. Some shear flows could also settle down into a state which is not a steady laminar flow, but is also not fully turbulent. Such states are unsteady and may be termed as ‘transitional.’

### 1.2.1 Energy growth of disturbances

The process of investigating the individual behaviour of the modes of a disturbance is called a modal analysis. The linearised system is cast in the form of an eigenvalue problem and stability analysis consists of finding the least unstable eigenmode of the system. The writing down of such a linear equation was first accomplished for viscous parallel shear flows by Orr (1907) and Sommerfield (1908) and were solved accurately for a channel flow using spectral methods by Orszag (1971). This idea has existed in the hydrodynamic stability theory for a long time and has successfully described instabilities and transition in flows like Rayleigh-Bénard convection. Eigenvalue analysis, however, fails to reproduce the experimentally observed transition to turbulence due to infinitesimal perturbations in shear flows like the Couette flow, pipe flow and channel flow. For decades it was

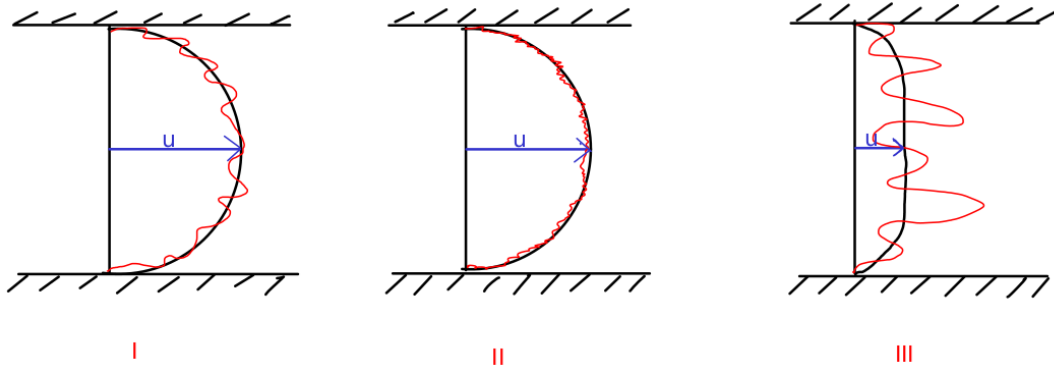


Figure 1.1: A cartoon of disturbance decay and growth over a base state in a parallel shear flow between two walls. The disturbance is in red and the base state in black. (I) A disturbance is imposed over the laminar base state. The disturbance can either die down as in (II) or grow in magnitude as in (III). The mean profile in (III) is flatter as compared to (I) and (II).

assumed that these flows undergo a nonlinear instability but later it was found (Butler and Farrell, 1992; Ellingsen and Palm, 1975; Landahl, 1980; Reddy and Henningson, 1993; Trefethen et al., 1993) that disturbances could grow algebraically to significant amplitudes by a linear mechanism. This happens when the linear stability operator is nonnormal, as will be discussed later in this thesis. In fact, in unbounded parallel flows of constant properties, it can be shown that the initial growth must be linear (Schmid et al., 2002). This is termed “nonmodal growth of perturbation” and we shall refer to “nonmodal analysis” in this thesis. Nonmodal growth is also referred to as transient growth or optimal growth across literature. In this viewpoint of stability, individual eigenmodes of the system are not considered alone but various combinations of these modes are studied to understand their effective behaviour. In a system described by a nonnormal matrix, the perturbation energy could always decay monotonically. This, in shear flows, happens below a particular Reynolds number, which we have referred to above as  $Re_E$ . Above  $Re_E$ , the behaviour depends on the nature of the perturbation. Certain perturbations decay monotonically. When perturbations are such that they contain a linear combination of certain eigenmodes in the correct range of initial amplitudes, they can (i) grow algebraically for some time before decaying (ii) grow algebraically to such an extent that nonlinear behaviour is initiated, and the system can go into a transitional or even a turbulent state. The latter also needs some minimum initial amplitude of

perturbations, not just the right linear combination. Nonmodal growth can occur only when the eigenvectors of the linear system are not all orthogonal to each other. Here, even when each individual mode is decaying, their resultant can grow for a short time. A schematic taken from Schmid (2007) as shown in figure 1.2 shows how even decaying nearly colinear vectors  $\Phi_1$  and  $\Phi_2$  can allow for their resultant  $f = \Phi_1 - \Phi_2$  to grow. With increasing time, as in each of the four frames of figure 1.2,  $\Phi_1$  decreases by 20% while  $\Phi_2$  decreases by 50%. The nonmodal analysis (looking at the combination of  $\Phi_1$  and  $\Phi_2$  rather than individually) shows the possibility that at intermediate times, some measure of a norm or resultant of vectors can grow. It also shows that the resultant progressively orients itself in the direction of the least stable eigenvector  $\Phi_1$  as time progresses. This growth in norm can also be translated to growth in energy and such intermediate-time energy growth can be enough for the transition of flow from laminar to turbulence.

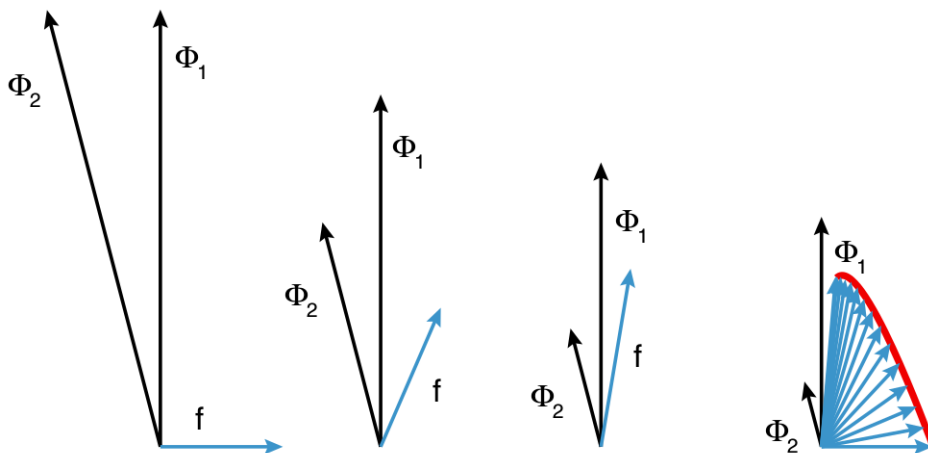


Figure 1.2: A schematic of nonmodal growth. While vectors  $\Phi_1$  and  $\Phi_2$  decay in time from left to right by 20% and 50% respectively in every frame,  $f = \Phi_1 - \Phi_2$  grows because of non-orthogonality of the two vectors, and directs itself to the direction of the least stable vector  $\Phi_1$ . The red line shows the change in magnitude of the resultant  $f$  with time. Adapted from Schmid (2007). Used with permission from the Annual Review of Fluid Mechanics.

So, essentially, nonmodal analysis is the study of an initial value problem, often in a subcritical system, and concerned with finding the initial condition that can cause the highest transient growth of some measure. For example, we can look at the maximum amplification of the energy from its initial value. It becomes obvious here that the time over which we want to maximise the energy enters into the stability calculations and

a disturbance that causes the maximum growth over a fixed time interval may not be the most dangerous initial condition when we analyse a different time horizon. This technique of nonmodal analysis is helpful when the eigenvectors of the flow operator are not orthogonal to each other and the most unstable mode of the system as uncovered by the linear modal stability fails to address the short-time dynamics of the system. Böberg and Brosa (1988); Butler and Farrell (1992); Reddy and Henningson (1993) among others calculated optimal disturbances for nonmodal energy growth. Butler and Farrell (1992) calculated the three-dimensional perturbations that gain the most energy in a given time period. They pointed out that the disturbance that grows in energy the most is not of the modal form but is in the form of elongated vortices in the flow direction and is oriented opposite to that of the mean flow. We underline that the most unstable perturbation often has a specific structure, which most often does not resemble that of the least stable eigenmode found by eigenvalue analysis. The nonmodal energy growth can be as large as  $\mathcal{O}(1000)$  in channel and Couette flows even with small amplitude perturbations (Reddy and Henningson, 1993).

These traditional analyses are based on the premise that the base flow of the system is independent of time, i.e., the mean flow as shown in figure 1.1 does not change over time. And then the growth of the perturbations over and above this base state is calculated. But this does not have to be the case with many real-life complex flows. The base flows can be time-periodic or even be slowly varying in time. Still, nonmodal analysis can be conducted for such flows but not in its current form. To analyse such time-varying flows, it is required to formulate the stability of the flow as a variational problem (Hill, 1995). Rather than using matrix decomposition techniques, an iterative algorithm in time can be constructed and applied to any generic flow to study nonmodal energy growth of disturbances (Schmid, 2007). The outcome of such an analysis is the optimal disturbance that is responsible for the highest nonmodal growth and under some conditions can cause the transition to a different state like turbulence.

In the recent years, this generalised technique of using variational principles to study nonmodal energy growth and calculating the most energetic disturbance, called the optimal, has been applied to a range of complex flows and reviewed in Kerswell (2018). It involves an iteration to maximise or minimise a certain quantity of interest, e.g., the kinetic or potential energy of velocity perturbations or scalar etc. Foures et al. (2014) worked on

optimising for mixing of temperature in a two-dimensional channel flow. Despite being in the linearly stable regime, due to nonmodal energy growth, mixing of temperature was observed to be enhanced. The optimal disturbance found using this technique was also found to enhance the transport of temperature across the breadth of the channel. Marcotte and Caulfield (2018) extended the above study to a stratified channel flow by including gravity in the governing equations of the flow. They also observe something similar to Foures et al. (2014) where mixing is enhanced due to the nonmodal growth induced by the optimal disturbance, and with an increase in the strength of stratification, this energy growth was reduced.

When the initial energy of the perturbation goes to zero, i.e., the amplitude of the disturbances are infinitesimal, we must recover the results of the linear nonmodal analysis. Kaminski et al. (2014) studied linear optimal perturbations for a stratified shear layer. They studied nonmodal growth both in stable and unstable regimes as dictated by linear stability analysis. They found that despite linear stability analysis suggesting that for a flow with a Richardson number (nondimensional ratio of buoyancy to shear)  $> 1/4$  being stable, the linear optimal undergoes transient growth due to the nonnormality of the flow operator. The growth in energy was shown to be greater than what would be expected out of the singular value decomposition of the linearised stratified governing equations. They found that over long times, the nonmodal growth was dependent on the degree of temperature stratification and approached an increasingly two-dimensional form (as opposed to the three-dimensional form in the case of short-time analysis), similar to what had been found by Arratia et al. (2013) for an unstratified time-evolving mixing layer.

Nonmodal analysis, when applied to a nonlinear system, constitutes the theory of nonlinear nonmodal analysis. Nonlinearity can, of course, introduce physics in the system which will be missed if we consider only the linearised version of the equations. Pringle and Kerswell (2010) studied the nonlinear optimal for a pipe flow and found it to be different from the linear optimal. The linear optimal is two dimensional and independent of the length of the pipe, whereas the nonlinear optimal is three-dimensional and localized. They also found the nonlinear three-dimensional optimal to be more dangerous than the linear optimal to trigger turbulence in pipe flow. Cherubini et al. (2010) studied nonlinear optimal perturbations in a boundary layer and found localised structures for the transition to turbulence. This points to the importance of nonlinearity in the nonmodal analysis.

This is the reason why we carry out full nonlinear nonmodal analysis in a part of this thesis. The geometry of our interest is the canonical channel flow.

The study of nonlinear nonmodal analysis in this thesis is carried out with a numerical solver which was developed to solve the governing equations in a parallel processing mode in a computer. The variational method, that we have already commented upon, introduces a certain set of equations called the adjoint equations, which can be solved using numerical techniques similar to the governing equations. The governing equations of the flow are the Navier-Stokes equations, and the adjoint of the Navier-Stokes needs to be derived to formulate the nonmodal analysis. The Navier-Stokes equations can also be coupled to the temperature equation. This happens when the density or the viscosity of the flow varies due to changes in temperature. The temperature equation is a proxy for any time varying passive quantity and is a generic equation that can represent concentration of any scalar in a flow. But the effect of this scalar on the flow is particular to the nature of the scalar.

### 1.3 Viscosity variations

In multi-component flows, the viscosity of the fluid is not constant. This can happen when the flow is laden with particulates like polymers or sediment, or some quality of the flow varies. Most of the flows that are observed in nature are of varying viscosity. For example, viscosity variations can happen in flows like oceanic and atmospheric flows. In the simplest case, this happens when the temperature changes in the flow. To study a simple case of viscosity variation, we study laminar flow in a channel. It is to be expected that the stability calculations could be modified by the presence of viscosity variations in the flow. This is because viscosity, and its variations, (Ranganathan and Govindarajan (2001) and other later works reviewed in Govindarajan and Sahu (2014)), at high Reynolds number, act as a singular perturbation in the stability equations (Govindarajan, 2004). It is because the inverse of the Reynolds number (a small quantity) is multiplied by the highest derivative in the governing equations. In a part of this thesis, we have analysed the effects of viscosity variations on stability properties of a three-dimensional channel flow. As noted earlier, the nonmodal energy growth calculations are dependent on the time during which we are interested in the growth of perturbations. So, it is to

be expected that the optimal disturbances that cause transient growth at different time intervals would be different.

The nonmodal energy growth and its ability to transition a flow from laminar to turbulence is a broad topic of interest in itself. In this thesis, we touch upon both the concepts of stability of a flow and the properties of turbulence. Next, we study the turbulent properties of geophysical flows with special focus on the Bay of Bengal, a part of the Indian ocean. We elucidate the various turbulence signals in the Bay and attempt to study its importance in the Indian monsoon system. We first present an overview of our motivation to make the jump from nonmodal stability analysis to geophysical turbulence.

## 1.4 Earth's oceans

The storage and transport of heat in the ocean around the globe is a matter of concern and scientific study because of its importance in global climate. Water has a much higher heat capacity than air. Hence the oceans, which cover more than 70% of the earth's surface, store a major portion of the heat. To put into context the importance of oceans, we point out that the upper few metres of the ocean contain as much heat as the whole atmosphere above it (which is  $\mathcal{O}(\text{km})$ ). The oceans also absorb a large amount of heat without any significant increase in their temperature. Evidently, the oceans play a major role in the heat balance, and understanding the physical mechanisms that maintain this balance is evidently of great importance. Major events like the 1997-98 El Niño have had a strong impact in the world's climate (McPhaden, 1999). Studying and quantifying the effects of oceanic processes is important to understanding their interaction and feedback to the atmosphere. With gradual warming of the world oceans (Levitus et al., 2000), a need for more dedicated understanding of the ocean-atmosphere coupling is required. Projects like the Tropical Ocean-Global Atmosphere (TOGA) Program (McPhaden et al., 1998) had tried to decipher some of the air-sea interactions, in what has become currently a well-studied subject like the El Niño Southern Oscillation.

Long term observations of the oceans have provided significant understanding of their annual cycle. There are various ways to undertake the observational task of the oceans and the atmosphere, and depending on the method undertaken, the temporal and the spatial

extent varies. Properties of the oceans that have been traditionally measured include temperature, conductivity (to infer salt content), speed of the flow, current direction, and turbulence.

## 1.5 Methods of Ocean Observation

One of the first recorded oceanographic measurements began with measuring ocean velocity and temperature with flowmeter and thermistors behind a ship and on a submarine (Grant et al., 1959, 1968, 1962). The experiments of Woods (1968) introduced dye in the ocean with the purpose of investigating thin sheets of high temperature gradient in the thermocline - the portion of the ocean just below the upper mixed layer where the mean temperature decreases with depth. A few other investigations (e.g., Bowden (1965)) derived estimates of turbulent mixing in the ocean from distributions of temperature and salt content (salinity) and from the results of a few earlier dye releasing experiments. It was inferred from studies of Grant et al. (1968) that the temperature structure in the ocean is not uniform as the thermistor sampled turbulent patches where temperature showed small scale variations. They found turbulence to be of more intensity in the upper 50m which then decreased to almost negligible values by 200m depth. Stommel and Fedorov (1967) and Woods (1968) observed staircases in temperature and salinity measurements in the ocean where the properties varied in a small depth range. These tried to establish that the ocean was not laminar and turbulence in the ocean occurred routinely to be observed by various experiments across different oceans. These turbulent fine-scale structures in the ocean were further explored by freely-falling vertical profilers by Osborn and Cox (1972). They dropped the thermistors from a ship which would measure the vertical profile of the ocean mostly focusing on the thermocline. These early studies gave rise to the research area of physical oceanography.

With developments in various technologies, the oceans began to be explored more and with the already available theoretical understanding, these explorations provided knowledge about the dynamics of the oceans and their impact on weather systems. Some of the common ways in which ocean observations have been carried out are

1. Oceanographic mooring,
2. Shipboard measurements,

3. Argo floats, and
4. Satellite observations.

Each of these ocean observation techniques have limitations, but when used in concert help in a better understanding of the oceans. As we use only mooring measurements in this thesis and I had collected data from shipboard instruments, I describe only those two in detail here.

### 1.5.1 Oceanographic mooring

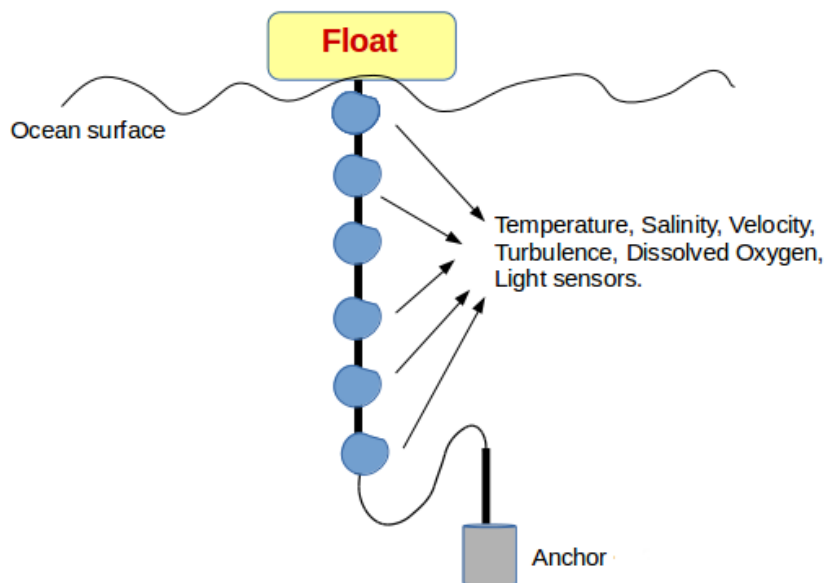


Figure 1.3: A schematic of a mooring. A float, made of a buoyant material, stays over the ocean surface and the anchor at the end of the mooring wire lies on the ocean bed to keep it at a fixed location. Various instruments to measure oceanic properties are fitted to the mooring wire. Sometimes instruments are also fitted to the float to measure meteorological data.

A mooring is a float (figure 1.3) that has various instruments on its wire and can be deployed in the ocean for long periods of time ( $> 1$  year) to collect data. A mooring thus allows for long time oceanic observations without continuous human effort. Moorings have been successful in studying extreme events like cyclones if they are situated in their paths where human presence is not possible. Apart from oceanographic instruments, a mooring float can be fixed with sensors that can measure atmospheric properties like humidity, wind speed, wind direction, rainfall, heat flux among others.

Research Moored Array for African-Asian-Australian Monsoon Analysis and Prediction (RAMA; (Mcphaden et al., 2009)) is an array of moorings in the Indian Ocean for better observation of the Indian monsoon, and has been active for almost two decades now (see e.g., Beal et al. (2020)). It has provided an extensive understanding of the intraseasonal oscillations in the Indian monsoon and the seasonality in the properties of the Indian Ocean (Sengupta et al., 2007), and also its response to extreme events like tropical cyclones. The Tropical Atmosphere Ocean (TAO) array of moorings (Hayes et al., 1991) have been in the Pacific Ocean for more than three decades and a similar mooring array in the Atlantic Ocean (Prediction and Research Moored Array in the Tropical Atlantic (PIRATA) (Servain et al., 1998)) have studied the long-term air-sea interactions, with potential consequences to droughts, floods, hurricanes etc. Apart from providing many years of data, they also provide information about the spatial variation in the oceanic properties and that of air-sea fluxes across the globe.

### 1.5.2 Research expeditions to the Bay of Bengal

Oceanographic data collecting instruments can also be carried on board research vessels, i.e., ships designed to carry out research expeditions. This method, however, is limited by the maximum amount of time the ship can afford to be in the ocean at one go. I was a part of two research expeditions to the Bay of Bengal to collect oceanographic and atmospheric data. The data from these research cruises have not been directly used for the turbulence analysis presented in this thesis but have helped initial preliminary understanding about the Bay, like spatial variations in salinity and temperature, air-sea fluxes etc. I describe briefly these expeditions here since they were a learning experience, and also importantly they informed my understanding of the turbulence measurements studied in this thesis, and helped immensely in handling the data. The mooring whose data a part of this thesis is based on was recovered during one of the cruises. The first cruise was in January-February of 2016 and was on the Oceanic Research Vessel (ORV) *Sagar Kanya*. It was a joint effort by the National Centre for Polar and Ocean Research, National Institute of Ocean Technology (NIOT), and Woods Hole Oceanographic Institution (WHOI). The second cruise in the southwest monsoon month of July 2019 was a part of the Monsoon Intraseasonal Oscillation in the Bay of Bengal (MISO-BoB) project, funded by the US Office of Naval Research and participated by Oregon State University, Scripps Institution

of Oceanography, WHOI, NIOT among others. I briefly describe the two cruises I was a part of.

### ORV *Sagar Kanya*

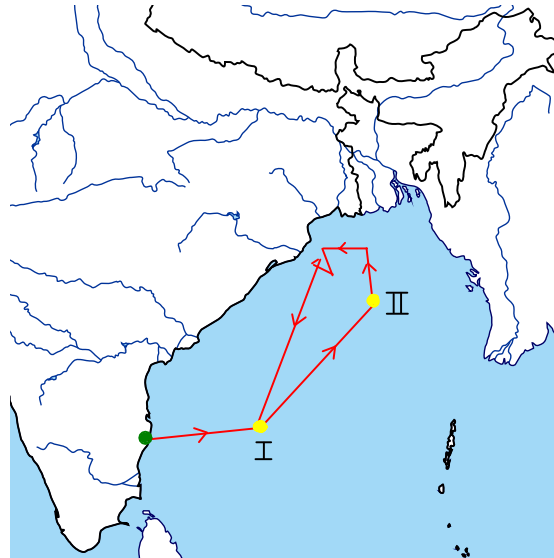


Figure 1.4: An approximate track of the *Sagar Kanya* in the Bay of Bengal in January-February 2016 is shown as red lines with arrows denoting directions. Two moorings are marked “I” and “II”, and Chennai port is marked as green filled circle.

This research expedition was for 17 days starting from the Chennai port (India) on 23 January 2016 with 21 scientists on board. The surveyed path of this cruise is shown as red line in figure 1.4. The yellow filled circles mark the locations of moorings that were recovered. Some of the objectives of the expedition were

1. to recover the Woods Hole Oceanographic Institute mooring from  $18^{\circ}$  North,  $89.5^{\circ}$  East (yellow circle in figure 1.4 marked II) which was deployed in December 2014. The data obtained from instruments fitted on this mooring have been extensively used in this thesis. These data include temperature, salinity, velocity, turbulence, air-sea fluxes, wind speeds etc., in the Bay of Bengal.
2. Extensive upper ocean survey of the North Bay of Bengal. The ship itself is equipped with thermosalinograph, underway CTD (conductivity, temperature, and depth probe) and acoustic Doppler current profiler (ADCP) to carry out ocean observations. We collected temperature and salinity data by continuously profiling the Bay using vertically falling underway CTDs.

3. Deployment of seven Argo floats, and recovery of a mooring in south Bay (marked I in figure 1.4) and deployment of another mooring at the same location.

### ORV *Sally Ride*



Figure 1.5: Recovery of a drogue buoy in the Bay of Bengal from the *Sally Ride* in July 2019. Photo courtesy of San Nguyen (Scripps Institution of Oceanography). Used with permission.

The research expedition on ORV *Sally Ride* started on 06 July and ended on 04 August 2019. We started from Chennai port and did many transects of the Bay of Bengal to measure ocean temperature, salinity, velocity, and turbulence in the  $15^{\circ}$ - $17^{\circ}$  North region along with other meteorological measurements. The main objective was to study the evolution of the ocean's surface boundary layer under strong atmospheric forcing during the summer monsoon and collecting extensive dataset to better sample the monsoon intraseasonal oscillations. We also recovered a RAMA mooring that had been in the Bay for more than a year. Sixty-nine radiosondes were launched from the ship to have concurrent atmospheric measurements to estimate the air-sea fluxes.

## 1.6 Some properties of oceanic flows

Because the Earth rotates about its axis, oceanic flows are governed by the Navier-Stokes equations in a rotating frame of reference. Many mechanical forcing agents like winds, the differential gravitational attraction of the moon and the Sun (tidal forces), and solar

heating, act to set the ocean in motion. Depending on the scale of these motions, the apparent force due to earth's rotation, also known as the Coriolis force, may or may not affect the motion. Winds can generate fluid motions in the upper hundreds of meters of the ocean. But the deep ocean water is also recirculated albeit in timescales of thousands of years due to the differential heating at the poles and the equator. The Coriolis force turns the oceanic currents to their right in the northern hemisphere and to their left in the southern hemisphere. If winds steadily blow over a surface, steady motion can be generated and is termed as Ekman flow (Ekman, 1905). The net Ekman transport of water can be derived to be at right angles to the wind direction in both the hemispheres. These steady motions can cause local convergences and divergences in the ocean surface. When constantly blowing wind moves surface waters from a given place, deeper water comes up to conserve mass. This is called upwelling. If the opposite happens, the process is called downwelling. Both are observed near land boundaries and also in the open ocean like currents near the equator (e.g., Johnson et al. (2001)). Vertical velocities associated with both are of the order of metres per day and hence present a challenge to accurate measurements but are nevertheless an important component of oceanic flows with importance linked to the biogeochemical cycle (Chavez et al., 1999).

The currents in the ocean can undergo instabilities and form eddies that can extend to hundreds of metres deep into the ocean can be as large as  $\sim 100$  km (Gordon et al., 2017). These are an important part of the ocean because they transport heat, salt, sediments, and carbon, determine the density structure of the oceans, and play an important role in the global circulation (Hallberg and Gnanadesikan, 2006). These eddies can range from  $\mathcal{O}(\sim 1\text{km})$  to  $\mathcal{O}(100\text{km})$  and are termed submesoscale and mesoscale eddies, respectively (Thomas et al., 2008). Mesoscale flows are mostly governed by the balance between the Coriolis force and the pressure gradient (geostrophic balance) and are essentially two-dimensional. Submesoscale flows, on the other hand, have one or two orders of magnitude higher vertical velocities (Capet et al., 2008) and act to extract the energy from the geostrophically balanced flows. They disintegrate to small-scale three-dimensional motions that eventually cause turbulence.

Sea-surface temperature (SST) is the temperature of the top surface of the ocean. SST is one of the most important parameters controlling an air-sea coupled system and is fed into climate prediction numerical models (Moore and Kleeman, 1999). In the review of

Schott et al. (2009), it has been pointed out that due to the failure to represent oceanic processes correctly like the SST, the ocean models have discrepancies in the Indian Ocean. The mixed layer of the ocean is defined as the upper ocean which is actively mixed by wind action. This mixing is done via turbulence. SST is greatly affected by the seasonal depth of the mixed layer. The role of vertical mixing in the seasonal cycle of the SST has been established in the equatorial pacific with subsurface turbulence measurements (Moum et al., 2013). Similar spatial and temporal understanding from long-time oceanographic mooring deployments is required to understand the role of the Bay of Bengal in the active and break periods of the Indian monsoon. The Bay of Bengal monsoon experiment was an attempt towards that understanding by a huge collaborative effort (Bhat et al., 2001).

## 1.7 Bay of Bengal and Indian monsoon

The surface waters of the Bay of Bengal are among the lowest salinity (or freshness) in the tropics. In the Bay, surface salinity can dip to 25 practical salinity units (psu; measured as grams of salt per kilograms of seawater) due to the freshwater outflow from rivers and monsoonal precipitation. The Indian monsoon affects a significant portion of the world's population. Fluctuations in the intensity of the Indian monsoon system propagate northward from the equator towards the Indian subcontinent (Sikka and Gadgil, 1980), bringing intervals of relatively wet and dry conditions. Precipitation associated with monsoon both feeds many rivers that discharge into the northern Bay of Bengal and provides close to 2m of rainfall each year over the Bay. The freshwater persists as a shallow layer in the Bay for 3-5 months starting around July (the latter half of the summer monsoon). This shallow, freshwater layer adjusts quickly to changes in air-sea heat fluxes but also limits atmospheric forcing of the ocean below. It is important to understand the upper oceanic layer as it plays a major role in the inputs to the coupled climate models. Monsoon convective activities have been suggested to be affected by the presence of this low-salinity water.

### 1.7.1 Ocean-Atmosphere coupling in Indian ocean

Numerical modeling studies have shown that the coupled dynamics of the ocean-atmosphere system, at timescales as short daily variations (diurnal), strongly affect the structure and

variability of the large-scale tropical atmosphere (Woolnough et al., 2007). Simultaneous observations have further demonstrated the co-evolution of the atmosphere and ocean in response to monsoon forcing in the Indian Ocean (Sengupta et al., 2001), including within the Madden-Julian Oscillation (McPhaden and Foltz, 2013; Moum et al., 2014), and during the northern hemisphere summer intraseasonal oscillations (Li et al., 2017). While sea surface temperature controls coupling at the air-sea interface, SST is itself influenced by net atmosphere-ocean heat flux, turbulent entrainment of typically cooler deep water into the mixed layer, horizontal and vertical advection, and the ocean's mixed layer depth.

Indian Ocean dipole (Saji et al., 1999) could have a strong impact on the Indian monsoon and is an evidence of the existence of a coupled ocean-atmosphere system over the northern Indian Ocean. Saji et al. (1999) showed a strong coupling of temperature differences between the eastern and western Indian ocean with the winds and precipitation, which is a strong indicator of ocean-atmosphere coupling. Inclusion of these interactions have helped improve prediction models but they are not ideal. Particularly interesting with regard to Indian ocean is to capture the salinity stratification at the surface of the Bay of Bengal and parametrisation of mixing in the upper ocean. A lack of better parametrisation potentially contributes to poor modelling (Rahaman et al., 2014). The spatial and temporal details lost due to averaging and interpolation, and hence inhibiting better parametrisation, can be improved upon by better and higher frequency measurements.

## 1.8 Ocean Turbulence

Flows in the ocean, by virtue of being in large spatial scales, are of high Reynolds number, defined as  $Re = UL/\nu$ , where  $U$  is the flow speed (usually  $\mathcal{O}(\text{m/s})$ ),  $L$  is a length scale appropriately chosen to be representative of the flow, and  $\nu$  is the kinematic viscosity of water. As the density of water in the ocean varies primarily owing to changes in temperature and salinity, the Richardson number is also another important nondimensional parameter that govern the dynamics of the flows. These flows display many types of instabilities when a nondimensional parameter is varied and, under certain conditions, undergo a transition from laminar to turbulence. Turbulent overturns are a source of

transport of oceanic heat and can carry nutrients to the deeper ocean. Its large size (i.e.,  $L$  in the definition of Reynolds number could be the depth of the ocean ( $\mathcal{O}(\text{kms})$ ) which is much larger than laboratory-scale experiments) and complexity, allow for a big range of time and length scales to develop.

Turbulence is a major player in heat transfer to the deeper ocean and has been known to have a seasonal nature. Bursts of turbulent events are interleaved with steady laminar flows and have been postulated to be important for the global meridional circulation (Munk, 1966; Wunsch and Ferrari, 2004). The two main drivers of turbulence are winds and tides with  $\sim 2$  terawatt of energy input into the oceans (Munk, 1966). Other small energetic candidates include surface buoyancy forcing and geothermal heating at the ocean abyss. Tidal flows over topography generate internal waves (Varma and Mathur, 2017) that either break near the generation sites (Alford et al., 2012), lose energy by nonlinear triadic interactions to small scales that eventually break (MacKinnon et al., 2013) or survive and travel for thousands of kilometers before hitting coastal regions and eventually breaking (Nash et al., 2004; Ray and Mitchum, 1996). Climate models are sensitive to the presence of internal waves in the ocean models (Melet et al., 2013). Because of the varied flavour in which they present themselves, they are difficult to be represented in models and hence the turbulent mixing they induce is not parametrised well.

### 1.8.1 Need for parametrisation

Turbulence in the ocean varies by many orders of magnitude in both space and time as reviewed recently in Moum (2020). Because of the large range of scales of motion, replicating the full dynamical properties of oceans in computations and laboratory experiments are not possible. The minimum vertical resolution in the ocean models ranges from 1-10m. Viscous dissipation by the turbulent cascade in the oceans can however occur in the range of  $< 1$  cm and hence there is a need to parametrise dynamics which are smaller than the vertical grid size of the models. The spatial and temporal variability of turbulent mixing gives rise to the ocean variability and incorrect parametrisation are a primary source of error in ocean models. These errors become more pronounced in places of strong currents and sharp changes in the topography like coasts, estuaries, and lakes (Durski et al., 2004; Stacey et al., 1999).

To this end, large scale ocean turbulence measurements have been conducted for a number of years. And only due to huge efforts to sample turbulence extensively in the ocean, it has led to the current level of understanding in its variability and its importance in controlling the feedback to the atmosphere. We present in this thesis turbulence measurements from the Bay of Bengal which we hope will add to the current repository of understanding and help improve turbulence parametrisation in coupled monsoon prediction models.

## 1.9 Outline of the thesis

The two halves of this thesis are contained in five chapters. The first half is on nonlinear nonmodal stability analysis of the viscosity stratified flows while the second part describes oceanic turbulence in the Bay of Bengal using moored mixing meters called  $\chi$  pods. These two parts are organised into different chapters as follows.

In chapter 1, we describe the principles of nonlinear nonmodal stability analysis. We describe the numerical technique of ‘direct-adjoint looping’ to formulate this stability study. We apply this technique to the full nonlinear Navier-Stokes equations and derive the adjoint Navier-Stokes equations. We describe the numerical methods used to solve the equations and also a numerical method of nonlinear optimisation. We then briefly describe some optimal disturbances found using our solver that cause maximum transient growth.

In chapter 2, we apply the nonlinear stability techniques developed in the first chapter to derive the viscosity stratified adjoint Navier-Stokes equations. We show that viscosity stratification plays a big role in the localisation of the optimal disturbances on the walls of the three-dimensional channel. We see that nonlinearity is a crucial ingredient because certain mechanisms are totally missed when the optimal disturbances are found for linear disturbance energies. We attempt to provide a physical mechanism of nonmodal energy growth in this system and comment on the existence of well-known lift-up and Orr mechanisms.

In chapter 3, we make a jump from nonmodal analysis to understanding geophysical turbulence. We detail the theoretical principles of geophysical turbulence measurements and describe the instrument  $\chi$  pod that had been used to measure turbulence in the Bay

of Bengal.  $\chi$  pods are moored turbulence measuring instruments fitted to oceanographic moorings and have provided year-long data in many different parts of the world. Turbulence data obtained from  $\chi$  pods in the Bay of Bengal forms the basis of analysis in the rest of the thesis.

In chapter 4, we detail the turbulence data obtained from the first year-long measurements in the Bay of Bengal at 18 °N and 89.5 °E at four different depths. We show that there is a seasonality to geophysical turbulence in this climatically important region. This seasonality is linked to the Indian monsoon system. We also show a surprising phase of suppressed geophysical turbulence that can have potential consequences to vertical heat transport and hence convective activities in the post-monsoon season.

In chapter 5, we delve deeper into a particular diurnal signal in turbulence observed in the Bay during the transition period (the month of May) to the southwest (summer) monsoon. This turbulence varies by two orders of magnitude in turbulent diffusivity and persists for about a month. We see a hitherto unobserved diurnal land-sea breeze that is present at the WHOI mooring location which is about 400-500 km from the land boundaries. This might be due to the unique topography and we strongly suspect that this land-sea breeze might be responsible for generating this diurnal signal in turbulence. However, we still discuss many other possible mechanisms which may have caused this diurnal signal. Even though we have a strong suspect, this is ongoing work and we do not have a complete understanding of the signal.

The thesis thus combines (a) an observational study of turbulence suppression and a resulting long-term laminar state at some depths in the Bay of Bengal, where the eddy viscosity in our region of interest varies by orders of magnitude, and (b) a theoretical and numerical study in a much simpler well-defined flow (pressure-driven flow through a channel) and how a variation of molecular viscosity affects instability and a departure from the laminar state. The entire process of disturbance growth in the latter, as we find, appears to be nonlinear, and this thesis develops the theoretical apparatus to study disturbance growth in viscosity-varying flows in this regime. A theoretical study of turbulence suppression by nonlinear stabilisation on a simple one-dimensional model of the upper Bay of Bengal, during different times of year, is a natural next step.

# Nonlinear instability and numerics

\*\*\*

In this chapter we first briefly describe the well-known concepts of linear modal and nonmodal analysis for simple operators. We then extend the concept of nonmodal analysis for nonlinear fluid flow problems. We describe a variational technique which could be used for complex time-varying flows for nonlinear nonmodal analysis by optimising for a desired cost functional. We introduce the adjoint of the Navier-Stokes equations. The analysis is then employed to study the nonmodal growth associated with the Navier-Stokes equations, subject to the boundary conditions appropriate to a three-dimensional plane Poiseuille flow (channel flow). Then, we describe the development of numerical techniques for solving the Navier-Stokes equations and their adjoints. We also describe a nonlinear optimisation technique to arrive at the nonlinear optimal perturbations of a channel flow which maximises a desired cost functional. This is a collaborative work with Arjun Sharma of Cornell University. The equations in section 2.6 are independently derived by the author and Arjun Sharma, and the numerical solver development and validation is a joint effort with Arjun Sharma.

## 2.1 Introduction

A matrix  $M$  which commutes with its own transpose (or its conjugate transpose in case the matrix  $M$  is complex), can be mathematically described as

$$MM^T = M^T M. \tag{2.1}$$

If all the eigenvalues of the matrix  $M$  in equation (2.1) are real, then  $M$  is also called Hermitian or self-adjoint.  $M$  can also be an operator and the same definition would hold. Fluid flow systems at various approximations can be assumed to be governed by different flow equations, like the Navier-Stokes equations, Euler equations etc. We can express these equations in the form of corresponding differential operators acting on flow variables governing their evolution. When energy is considered, the presence of mean shear most often makes the flow operator non-normal (this may, however, not hold for other kinds of norms; see Held (1985)). In this case,  $M$  is not diagonalisable, its eigenvectors are not pairwise orthogonal in the sense of energy, and hence they do not form a complete basis. On the other hand, a normal operator in the sense of an appropriate norm would have eigenvectors that are pairwise orthogonal. Normal operators can either be Hermitian and satisfy (2.1) or satisfy  $MM^T = -M^T M$  (skew-Hermitian operators).

## 2.2 Modal stability analysis

Let  $u$ ,  $v$ , and  $w$  be the  $x$ -,  $y$ - and  $z$ -component of a three dimensional disturbance to a shear flow  $\mathbf{U}_i = U(y)\delta_{i1}$  as shown in figure 2.1. Then, the  $y$ -component of vorticity (or the curl of velocity) can be defined as,

$$\eta = \frac{\partial u}{\partial z} - \frac{\partial w}{\partial x}. \quad (2.2)$$

We can express the  $y$ -components of disturbance velocity and vorticity in the normal mode form as  $v = \tilde{v}(y)e^{\iota(\alpha x + \beta z - \omega t)}$  and  $\eta = \tilde{\eta}(y)e^{\iota(\alpha x + \beta z - \omega t)}$ . Using these forms in the linearised governing equations of  $v$  and  $\eta$ , following Schmid et al. (2002), the resulting equations can be cast in velocity-vorticity formulation for the shear flow as

$$\frac{\partial}{\partial t} \begin{pmatrix} \tilde{v} \\ \tilde{\eta} \end{pmatrix} = \begin{pmatrix} \mathcal{L}_{OS} & 0 \\ \iota\beta U' & \mathcal{L}_{SQ} \end{pmatrix} \begin{pmatrix} \tilde{v} \\ \tilde{\eta} \end{pmatrix}. \quad (2.3)$$

Here  $\alpha$  and  $\beta$  are the streamwise ( $x$ ) and spanwise ( $z$ ) wavenumbers,  $\omega$  is the frequency, and a prime ( $'$ ) denote a  $y$ -derivative. Boundary conditions that should be imposed are  $\tilde{v} = \frac{\partial \tilde{v}}{\partial y} = \tilde{\eta} = 0$  at the walls.  $\mathcal{L}_{OS}$  is the Orr-Sommerfeld operator which governs the dynamics of the normal velocity  $\tilde{v}$  and  $\mathcal{L}_{SQ}$  is the Squire operator that governs the

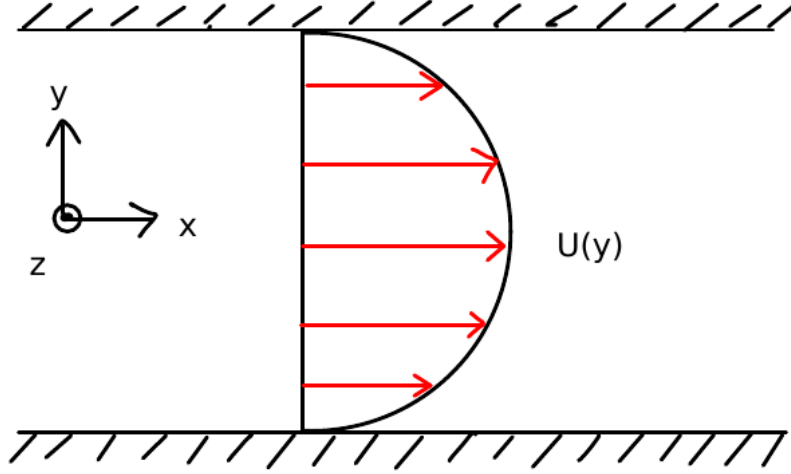


Figure 2.1: A schematic of a three-dimensional shear flow through two parallel walls in the  $y$ -direction. The base profile is  $U(y) = 1 - y^2$  and hence has shear  $U'(y) \equiv dU/dy$ .  $x$  is the streamwise direction,  $y$  the wall-normal and  $z$  the spanwise direction.

dynamics of the normal vorticity  $\tilde{\eta}$ . They are of the form

$$\mathcal{L}_{OS} = \iota\alpha U(k^2 - \mathcal{D}^2) + \iota\alpha U'' + \frac{1}{Re}(k^2 - \mathcal{D}^2)^2 \quad (2.4)$$

and

$$\mathcal{L}_{SQ} = \iota\alpha U + \frac{1}{Re}(k^2 - \mathcal{D}^2), \quad (2.5)$$

with  $k = \sqrt{\alpha^2 + \beta^2}$ ,  $\mathcal{D} = \partial/\partial y$ ,  $Re$  is the Reynolds number as defined in the previous chapter. The characteristic length scale is most often half the height of the channel. The formulation in equation (2.3) allows a recasting as an eigenvalue problem with the frequency  $\omega$  appearing as the complex eigenvalue

$$-\omega \begin{pmatrix} k^2 - \mathcal{D}^2 & 0 \\ 0 & 1 \end{pmatrix} \begin{pmatrix} \tilde{v} \\ \tilde{\eta} \end{pmatrix} + \begin{pmatrix} \mathcal{L}_{OS} & 0 \\ \iota\beta U' & \mathcal{L}_{SQ} \end{pmatrix} \begin{pmatrix} \tilde{v} \\ \tilde{\eta} \end{pmatrix} = 0. \quad (2.6)$$

We may then solve this eigenvalue problem to find if initial perturbations of any wavelength can grow in time as  $t \rightarrow \infty$  assuming real  $\alpha$  and  $\beta$ . This is also called modal analysis.

The same eigenvalue problem (2.3) can also be compactly written in the form

$$\frac{\partial \mathbf{q}}{\partial t} = M\mathbf{q} \quad (2.7)$$

where

$$\mathbf{q} = \begin{pmatrix} \tilde{v} \\ \tilde{\eta} \end{pmatrix} \text{ and } M = \begin{pmatrix} \mathcal{L}_{OS} & 0 \\ \iota\beta U' & \mathcal{L}_{SQ} \end{pmatrix}. \quad (2.8)$$

From (2.7), the solution  $\mathbf{q}$  after time  $t$  when initialised with a random initial condition  $\mathbf{q}_0$  can be written in the matrix exponential form as

$$\mathbf{q} = e^{Mt} \mathbf{q}_0. \quad (2.9)$$

The Reynolds number  $Re$  is the control parameter here, and with the above modal analysis, the critical Reynolds number  $Re_{cr}$  above which an exponentially growing mode exists, i.e., the system is unstable, can be predicted. Modal analyses predicts unconditional stability of laminar pipe and Couette flow, i.e., these flows should be linearly stable to modal perturbations at all Reynolds numbers. However, these flows go to turbulence at finite Reynolds number. This is thus a failure of modal analysis in describing the dynamics for such flows.

However, modal analysis is successful in many cases too. A good example is the buoyancy-driven Rayleigh-Bénard convection. Nondimensionalising the governing equations for this flow will introduce the control parameter Rayleigh number (nondimensional ratio of diffusion transport rate to advective transport rate) (Rayleigh, 1916) as opposed to the Reynolds number. A modal analysis of this system correctly predicts the critical Rayleigh number at which the flow becomes unstable and can transition to turbulence.

This success of modal analysis for Rayleigh-Bénard convection is due to the absence of mean shear. Because of this, the governing operator is normal, i.e., the equality in equation (2.1) holds true and the eigenvectors of the operator are pairwise orthogonal. The system is therefore fully governed by its eigenvalues. For shear flows, this is not the case. From the flow operator in equation (2.3), it can be seen that solution of the normal-velocity  $\tilde{v}$  acts as a forcing to the equation of the wall-normal vorticity  $\tilde{\eta}$  via the linear coupling term  $\iota\beta U'$ . The resulting stability operator is non-normal due to the presence of shear ( $U'$ ), and the equality in equation (2.1) does not hold. The Orr-Sommerfeld operator as defined in equation (2.4) is itself non-normal, and can give rise to transient growth. But the coupling term  $\iota\beta U'$  often makes a bigger contribution. Even though the eigenvectors of the Orr-Sommerfeld operator for a bounded domain form a complete basis (Di Prima and Habetler, 1969), because the operator is non-normal, the eigenvectors are

not pairwise orthogonal and are very sensitive to perturbations (Reddy et al., 1993). Shear flows like channel flow, pipe flow, and Couette flow are collectively governed by non-normal governing operators of form (2.3) with different boundary conditions.

While modal or eigenvalue analysis predicts the long-time behaviour of the flow but due to the existence of suitably-arranged non-orthogonal eigenvectors of non-normal operators, shear flows can instead experience intermediate-time energy growth (or transient growth). The failure of modal analysis in shear flows is due its inability to reveal this intermediate-time dynamics. That means modal or eigenvalue analysis does not convey the full dynamics of a shear flow. Even in the linear limit, this necessitates the study of a combination of eigenmodes and not individual eigenmodes in isolation. This study of a combination of eigenmodes is called nonmodal analysis.

## 2.3 Nonmodal stability analysis

Linear modal analysis for unstratified parallel model shear flows like channel flow predicts the critical Reynolds number as 5772.22 (Orszag, 1971). Only for  $Re > 5772.22$ , an unstable eigenvalue exist on the spectrum of the Orr-Sommerfeld operator. The corresponding disturbance is called the Tollmien-Schlichting (TS) wave (Schlichting, 1933; Tollmien, 1930). For  $Re < 5772.22$  called the subcritical range, same modal analysis predicts that every disturbance should die down as  $t \rightarrow \infty$ . In other words, all the eigenvalues of the flow operator are negative and hence no single eigenmode can grow in isolation. But experimentally, turbulent spots appear even at  $Re < 1000$  (Tuckerman et al., 2014), and the flow is usually fully turbulent by  $Re \sim 1500$ . According to modal analysis, pipe flow should be stable up to infinite Reynolds number, but experimentally it goes to turbulence in the range of 1760-2300 (Eckhardt et al., 2007; Kerswell, 2005). Also, Couette flow is linearly stable to all disturbances but this again is not observed experimentally as Couette flow shows turbulent patterns at Reynolds number as small as 350 (Barkley and Tuckerman, 2005). The shortcomings of modal or eigenvalue analysis when applied to Couette flow was first recorded by Case (1960) and it was suggested that this problem be handled as an initial value problem. Non-modal analysis, as noted in the previous chapter, is essentially an initial value problem where the evolution of a

disturbance, which could be a combination of different eigenmodes, is analysed. Initial value analysis can uncover any short-time or transient growth in energy that can occur in the flow due to the superimposition of eigenmodes even though they are individually decaying as described with figure 1.2 in the previous chapter. The discrepancies in experimental observations and theoretical predictions for channel, pipe, and Couette flow are a manifestation of non-modal energy growths in these flows. For such shear flows, non-modal analysis complement modal analysis in fully understanding their behaviour. The method of nonmodal analysis was refined over the years and applied to canonical shear flows by Böberg and Brosa (1988); Butler and Farrell (1992); Trefethen and Embree (2005); Trefethen et al. (1993) (for a review, see Schmid (2007)) and could settle some of the discrepancies between experiments and observations. Recent developments have helped further the application of nonmodal analyses technique to identify the importance of coherent structures and their role in short-time energy growth as will be elucidated in the next chapter.

While modal analysis deals with exponential growth of instabilities, non-modal instabilities are algebraic in nature. To define stability in a finite time interval of  $t \in [0, T]$ , we define a certain quantity which is representative of growth of disturbances over any equilibrium state. We are aiming at a general initial value problem by examining the growth of any disturbance over this finite time interval and not just the asymptotic behaviour of the eigenmodes of the system. Short-time dynamics is of importance for processes with a finite lifetime related to some characteristic time in the flow like eddy turnover timescale (Schmid and Brandt, 2014) and looking at only the long-time limit is not helpful as it may not capture the full dynamics of the system. One of the most commonly used quantities for nonmodal analysis in a system is the spatial integral (over a volume  $V$ ) of the square of the  $l^2$ -norm of vector  $\mathbf{q}$  which is the energy in the perturbations,

$$E(q(t)) = \int_V (\mathbf{q}(\mathbf{x}, t) \cdot \mathbf{q}(\mathbf{x}, t)) d\mathbf{x} \equiv \|\mathbf{q}(\mathbf{x}, t)\|_V^2. \quad (2.10)$$

To examine stability of the system over an equilibrium state due to any random initial condition  $\mathbf{q}_0$ , we define a quantity,

$$G(t) = \frac{E(q(t))}{E(q_0)} \quad (2.11)$$

which is the perturbation kinetic energy growth after some time when the system is perturbed with  $\mathbf{q}_0$ . When this growth is optimised over all initial conditions we have

$$G_{\max}(t) = \max_{\mathbf{q}_0} \frac{E(q(t))}{E(q_0)}, \quad (2.12)$$

which is the envelope of energy growth over all initial conditions. The maximum growth at different times would most likely be caused by different initial conditions  $\mathbf{q}_0$ . A linear non-modal study often optimises for the energy growth of an infinitesimal initial perturbation over all possible initial conditions, and from the singular value decomposition (SVD) of the linear operator, reveals the optimal perturbation, i.e., the initial perturbation that leads to the largest transient growth in the linear regime at a certain time  $t = \mathcal{T}$ . Hence,  $G(\mathcal{T})$  as defined above can be obtained by SVD of the matrix exponential in equation (2.9) and the optimal growth is the square of the  $l^2$ -norm of the matrix exponential  $e^{Mt}$ , if  $M$  is autonomous (see, e.g., Schmid and Brandt (2014)).

In a channel flow (at  $Re = 2000$ ) and in Couette flow (at  $Re = 1000$ ), the most amplified disturbance found via nonmodal analysis is a streamwise-independent structure with the spanwise wavenumber  $\beta \approx 2$  appearing in the form of a pair of streamwise counter-rotating vortices. However, the most unstable eigenmode, the TS wave is a streamwise-dependent two-dimensional mode. Hence, the optimal disturbances, as recovered from nonmodal analysis, may not have any structural similarity with the most unstable or the least stable eigenmode of the system recovered via modal analysis. The highest energy transfer due to this optimal disturbance happens from cross-stream velocities to streamwise velocity (Schmid and Brandt, 2014). This is a linear energy transfer phenomenon and is called the lift-up mechanism, described for inviscid shear flows by Ellingsen and Palm (1975); Landahl (1980) and reviewed for various flows in Brandt (2014). In this process, streamwise-independent  $v$  and  $w$  perturbations (the cross-stream velocities) induce growth in streamwise-independent  $u$  perturbations (streamwise velocity) giving rise to streaks which grow in energy. Apart from the structural dissimilarity, it has also been shown that TS instability is susceptible to variations in the base flow but the nonmodal growth via lift-up mechanism due to this optimal structure (streamwise vortices) is more stable to such variations.

Lift-up mechanism is hence a robust nonmodal growth mechanism in shear flows and is often responsible for the subcritical transition to turbulence. Even in the presence of

modal or exponential instabilities, this nonmodal growth mechanism can still be relevant, especially if the former is slow. This growth is algebraic in nature and is most relevant in subcritical Reynolds numbers, and can eventually induce instability in the flow despite the flow not having any initial inflectional profile or not having any modal instability.

In channel flow, this lift-up process has been established to be the first growth mechanism in the subcritical transition to turbulence via generation of low and high speed streaks (Henningson et al., 1993; Reddy et al., 1998). After these streaks grow in energy, nonlinear effects become important and they modify the base laminar velocity profile. This introduces inflectional quality in the wall-normal and spanwise velocities that undergo secondary instabilities that further appear as streak oscillations (Brandt and Henningson, 2001) and finally turbulent puffs.

The consequence of the linear coupling term  $\iota\beta U'$  in the flow operator (as discussed in the previous subsection) is not just limited to introducing non-modal growth in transitional flows but also in maintenance of near-wall turbulent structures in full-developed wall-bounded turbulence. Turbulence being a highly nonlinear process, the importance of a linear coupling term in its sustenance seems counter-intuitive. However, a mechanism has been described (Jiménez, 2013) where the inviscid Orr mechanism causes transient growth of disturbances near the walls in fully-developed turbulence and could be responsible for energetic events like bursts. The disturbance that causes transition to turbulence with the least kinetic energy has been termed the minimal seed (Pringle and Kerswell, 2010) and shows this lift-up mechanism apart from another transient energy growth process called the Orr mechanism (Orr, 1907). In other flows like boundary layers, Cherubini et al. (2011) have identified mechanism of energy transfer analogous to the lift-up and have termed it the modified lift-up mechanism.

Transition to turbulence in the absence of modal instability has also been termed bypass transition because transition occurs without the supposedly traditional route of growth and eventual breakdown of unstable TS waves. The existence of various intermediate-time growth mechanisms, as briefly mentioned above, in transitional flows as well as fully-developed turbulence, necessitates viewing flow stability from an initial value perspective of non-modal growth rather than just eigenvalue analysis. SVD has been shown to be the tool to optimise over initial conditions if the linear flow operator is autonomous. But in the case of time-periodic or unsteady base flows, the nonmodal

analysis is conducted by formulating a variational technique which views the flow as a dynamical system.

## 2.4 Dynamical systems approach to fluid flow

One of the earliest attempts to understand laminar-turbulent transition from a dynamical systems point of view is attributed to Hopf (1948). The state of the fluid is analysed as a vector field in the ‘fluid space’, which is an infinite dimensional phase space, and the flow evolves in this phase space. This phase space could have different possible attractors, that are approached by nearby trajectories. The laminar and the turbulent states are such attractors. In some flows and in some ranges of Reynolds number, these can co-exist in the same phase space. Every attractor is surrounded by a basin of attraction and the transition from an attractor  $\Lambda_1$  to another  $\Lambda_2$  would need an energy change that is capable of taking the system out of the basin of attraction of  $\Lambda_1$ .  $\Lambda_1$  and  $\Lambda_2$  can be either laminar or turbulent state and the routes from one to the other could be uncountable.

This means that the dynamical systems approach of stability inherently includes the concept of energy of perturbations in the analysis. When applied to a nonnormal system which experiences nonmodal growth, it establishes a theory of nonlinear nonmodal stability analysis. The most general approach is to formulate the stability analysis as an adjoint optimisation problem using variational calculus which exploits the ability of the adjoint fields to provide sensitivity to initial conditions. When combined with a gradient optimisation technique like steepest descent or conjugate gradient, it can find the optimal initial condition to optimise for any desired cost functional, not necessarily perturbation kinetic energy (Arratia et al., 2013; Cherubini et al., 2010; Foures et al., 2014; Luchini and Bottaro, 2014; Vermach and Caulfield, 2018).

## 2.5 Definition of adjoints

The adjoint and the adjoint operator are defined as

$$\int \mathbf{u}^*(X) A \mathbf{u}(X) dX = \int \mathbf{u}(X) A^* \mathbf{u}^*(X) dX. \quad (2.13)$$

Here  $\mathbf{u}^*$  and  $A^*$  are the adjoints of vector  $\mathbf{u}$  and any operator  $A$ , respectively, and  $X$  could be a spatial variable or time. The definition (2.13) is applicable to any system of choice. We shall apply this definition to the full Navier-Stokes equations. In that case, the operator  $A$  would be the Navier-Stokes operator and  $\mathbf{u}$  would be the velocity field. As the velocity field is both space and time varying,  $\mathbf{u}(X)$  would now be  $\mathbf{u}(x, y, z, t)$  and the integral in (2.13) will be an integral over the whole flow volume and all times, i.e.  $\int \int (\dots) dV dt$ , where  $dV$  is a volume element in the domain of the flow and  $t$  is time. A procedure involving integration by parts of the left side of (2.13) will lead us to find the adjoint operator  $A^*$  and when similar arguments are applied to the Navier-Stokes operator, it will lead us to find the adjoint Navier-Stokes operator. When the same operation is applied to the temperature equation it will lead us to find the adjoint temperature equation. The application of this definition of adjoint to the Navier-Stokes and temperature equations will be discussed in this chapter and how they help formulate a problem of nonlinear nonmodal analysis.

## 2.6 Variational method of nonmodal analysis

Adjoint equations (Hill, 1995) are sensitivity equations and can be applied to both discrete and continuous fields, and has been used in a range of studies, not just limited to fluid mechanics (reviewed in Luchini and Bottaro (2014)). It has found profound use in optimisation problems where there are many inputs and the interest is in a certain optimal input which would maximise or minimise a certain cost functional. The optimisation problem is developed from principles of variational calculus which involves defining a Lagrangian of the flow which is the cost functional constrained by the governing equations and other system-related constraints. These constraints are imposed with the help of adjoint variables which were briefly defined in the previous section. In this thesis, we have assumed that our cost functional is the kinetic energy of the perturbations. There is, however, no restriction on what the cost functional can be, e.g., it can be potential energy in the flow or turbulent kinetic energy or dissipation, and the exact choice would depend on the problem of interest.

To analyse the nonmodal energy growth in any generalised fluid flow system, we start by forming a Lagrangian to find an optimal perturbation that maximises the perturbation

kinetic energy which is subject to the constraints such as Navier-Stokes and temperature equation, the initial conditions of the flow, and the total initial energy in the perturbations. These constraints are put in place with the help of adjoint variables. Equating the variations of the Lagrangian with respect to flow variables to zero give us the evolution equations of the adjoints. The variations with respect to the initial condition give us a direction to the optimal perturbation. At optimality, the derivative with respect to initial condition goes to zero (or below some numerical tolerance) and we have the optimal perturbation that causes the maximum perturbation kinetic energy growth.

This variational problem using adjoints is hence an optimisation in time as is represented in a schematic in figure 2.2. The aim of this loop is to find the optimal condition. At the very first loop we have to guess an initial condition which in most of our simulations is a random noise. Adjoint equations, as will be seen later, are well-posed only in ‘backward’ time evolution. A loop in time is completed when the governing equations are solved from  $t = 0$  to  $t = \mathcal{T}$  and the adjoint equations are solved in backward time from  $t = \mathcal{T}$  to  $t = 0$ . At the end of the looping, i.e. step (d) in figure 2.2, the gradient of the Lagrangian with respect to the initial conditions at time  $t = 0$  gives us the direction towards the optimal condition and we use a gradient descent method (step (e)) to update our guess and gradually march towards the optimal perturbation. We have to repeatedly do the looping in figure 2.2 until the gradient with respect to initial condition is below a certain numerical tolerance.

### 2.6.1 Application to the Navier-Stokes equations

The variational method of nonmodal analysis can be essentially applied to any system. We elucidate how this can be applied to the Navier-Stokes and temperature equations. The nondimensional equations governing mass conservation, momentum and temperature of a fluid subjected to a pressure gradient are written in terms of the perturbations (about a chosen laminar flow) evolution in equations (2.14)-(2.16). This set of equations will be called the ‘direct’ equations and the variables as ‘direct’ variables. It is assumed that the velocity field and pressure satisfies the homogeneous boundary condition, i.e., nonslip on walls and periodicity in unbounded directions.

$$\frac{\partial u_i}{\partial x_i} = 0, \quad (2.14)$$

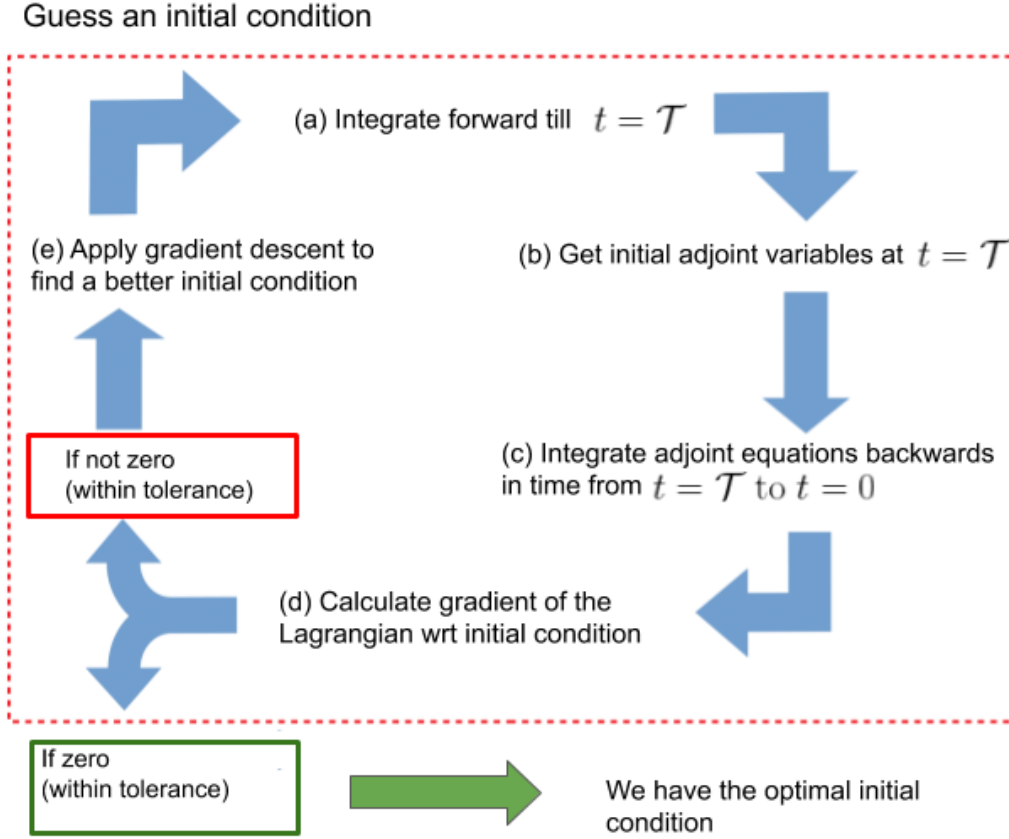


Figure 2.2: Schematic of the direct-adjoint looping problem is shown inside the red dashed box. The aim of this loop is to find the optimal initial condition or optimal perturbations that maximises a cost functional of interest. To calculate optimal perturbations of the Navier-Stokes equations, this loop has to run somewhere between  $\mathcal{O}(10)$  to  $\mathcal{O}(100)$  times depending on the amplitude of the perturbations in the “guess an initial condition” step.

$$\frac{\partial u_i}{\partial t} + (U_j + u_j) \frac{\partial u_i}{\partial x_j} + u_j \frac{\partial U_i}{\partial x_j} = -\frac{\partial p}{\partial x_i} + Ri_b T n_i + \frac{2}{Re} \frac{\partial}{\partial x_j} (s_{ij} + S_{ij}), \quad (2.15)$$

$$\frac{\partial T}{\partial t} + (U_j + u_j) \frac{\partial T}{\partial x_j} + u_j \frac{\partial (\bar{T} + T_0)}{\partial x_j} = \frac{1}{RePr} \frac{\partial^2 T}{\partial x_j^2}. \quad (2.16)$$

$U_j$  are the components of the base (laminar) velocity profile whose stability we study.  $u_i$  are fluctuation velocities (imposed on the flow),  $p$  is the pressure,  $Re$  is the Reynolds number defined as

$$Re = U_c H / \nu, \quad (2.17)$$

where  $U_c$  is the maximum velocity of the unperturbed and unstratified flow,  $H$  is the half of the channel height, and  $\nu$  is the kinematic viscosity of the fluid.

$$Ri_b = \frac{g}{\rho} \frac{\partial \rho / \partial y}{(\partial U / \partial y)^2} \quad (2.18)$$

is the Richardson number and is a ratio of buoyancy and shear, where  $\rho$  is the density that can change only due to temperature.  $S_{ij}$  and  $s_{ij}$  are the base and the perturbation velocity strain tensors

$$S_{ij} = \frac{1}{2} \left( \frac{\partial U_i}{\partial x_j} + \frac{\partial U_j}{\partial x_i} \right) \quad \text{and} \quad s_{ij} = \frac{1}{2} \left( \frac{\partial u_i}{\partial x_j} + \frac{\partial u_j}{\partial x_i} \right). \quad (2.19)$$

$T$  is the fluctuation temperature,  $\bar{T}$  and  $T_0$  (here taken as 290 K) are the background laminar and the reference temperature respectively. We set a subcritical  $Re = 500$  and  $Pr = 7$  in all our simulations.  $Ri_b$  has been currently set to zero but study with non-zero  $Ri_b$  is a work in progress. Hence we keep  $Ri_b$  in the derivations. We emphasize that these equations are fully nonlinear and hence the perturbations  $u_j$  can be of any arbitrary magnitude. The initial perturbation  $u_{0,i}$  is defined as

$$u_i(0) = u_{0,i}. \quad (2.20)$$

We define the total kinetic energy of perturbations as

$$E(t) = \frac{1}{2V} \int_V u_i(t)^2 dV. \quad (2.21)$$

Where  $\int_V dV$  is the volume integral over the whole domain of flow.

Using this, we can define a cost functional  $\mathcal{J}(\mathcal{T})$  as an integral over time in the range  $t \in [0, \mathcal{T}]$  of the normalised perturbation kinetic energy

$$\mathcal{J}(\mathcal{T}) = \frac{1}{E_0 \mathcal{T}} \int_0^{\mathcal{T}} E(t) dt, \quad (2.22)$$

where the normalisation factor  $E_0$  is the energy in the initial perturbations defined as

$$E_0 = \frac{1}{2V} \int_V u_i(0)^2 dV. \quad (2.23)$$

As mentioned above, the Lagrangian  $\mathcal{L}$  can now be defined as the cost functional  $\mathcal{J}(\mathcal{T})$

constrained by the governing equations (2.14)-(2.16) and the initial condition (2.20).

$$\begin{aligned} \mathcal{L} = \mathcal{J}(\mathcal{T}) - & \left[ \frac{\partial u_i}{\partial t} + (U_j + u_j) \frac{\partial u_i}{\partial x_j} + u_j \frac{\partial U_i}{\partial x_j} + \frac{\partial p}{\partial x_i} - Ri_b T n_i - \frac{2}{Re} \frac{\partial}{\partial x_j} (s_{ij} + S_{ij}), v_i \right] \\ & - \left[ \frac{\partial T}{\partial t} + (U_j + u_j) \frac{\partial T}{\partial x_j} + u_j \frac{\partial (\bar{T} + T_0)}{\partial x_j} - \frac{1}{RePr} \frac{\partial^2 T}{\partial x_j^2}, \tau \right] - \left[ \frac{\partial u_i}{\partial x_i}, q \right] - \langle u_i(0) - u_{0,i}, v_{0,i} \rangle. \end{aligned} \quad (2.24)$$

Where the parentheses are defined as

$$[a_i, b_i] \equiv \frac{1}{\mathcal{T}} \int_0^{\mathcal{T}} \langle a_i, b_i \rangle dt, \quad \langle a_i, b_i \rangle \equiv \frac{1}{V} \int_V a_i b_i dV, \quad (2.25)$$

and the Lagrange multipliers  $v$ ,  $\tau$  and  $q$  are adjoint velocity, temperature and pressure, and  $v_{0,i}$  is the adjoint of the initial velocity  $u_{0,i}$ . As the enforcement of the flow equations are local in space and time, the adjoint variables will also have evolution equations (which are functions of space and time) and are derived from variations of the Lagrangian  $\mathcal{L}$  and using integration by parts as detailed below.

We define the variation of the functional,  $\mathcal{L}$ , w.r.t. a particular function,  $l$ , as

$$\frac{\delta \mathcal{L}}{\delta l} \cdot \delta l \equiv \lim_{\epsilon \rightarrow 0} \frac{\mathcal{L}(l + \epsilon \delta l) - \mathcal{L}(l)}{\epsilon}. \quad (2.26)$$

The variation of  $\mathcal{L}$  with respect to all the flow variables and their corresponding adjoints are independent of each other. The vanishing variational derivatives with respect to  $p$ ,  $u_i$ , and  $T$  give us the adjoint continuity, adjoint momentum, and adjoint temperature equations governing the time evolution of adjoint variables,  $v_i$ ,  $q$ , and  $\tau$ , and the ‘initial’ conditions of these adjoint variables at  $t = \mathcal{T}$ . Similarly, the vanishing derivatives of  $\mathcal{L}$  with respect to the adjoint variables, give us back the direct equations (2.14)-(2.16). In subsections (a)-(d) below, we take variations of the Lagrangian  $\mathcal{L}$  with respect to each and every independent direct variable and succinctly show how the adjoint equations emerge in section 2.7.

### (a) Variation with pressure

$$\frac{\delta \mathcal{L}}{\delta p} \cdot \delta p = - \left[ \frac{\partial(\delta p)}{\partial x_i}, v_i \right]. \quad (2.27)$$

By definition of the operator [...], this can be expanded as

$$= -\frac{1}{\mathcal{T}V} \int_0^{\mathcal{T}} \int_V v_i \frac{\partial(\delta p)}{\partial x_i} dV dt. \quad (2.28)$$

Using multidimensional equivalent of integration by parts

$$\begin{aligned} \frac{\delta \mathcal{L}}{\delta p} \cdot \delta p &= -\frac{1}{\mathcal{T}V} \int_0^{\mathcal{T}} \left( \oint_S v_i n_i \delta p dS - \int_V \frac{\partial v_i}{\partial x_i} \delta p dV \right) dt \\ &= -\frac{1}{\mathcal{T}V} \int_0^{\mathcal{T}} \left( \oint_S v_i n_i \delta p dS \right) dt + \left[ \frac{\partial v_i}{\partial x_i}, \delta p \right]. \end{aligned} \quad (2.29)$$

Where  $S$  is the surface of the volume  $V$ .

### (b) Variation with velocity

$$\begin{aligned} \frac{\delta \mathcal{L}}{\delta u_i} \cdot \delta u_i &= \frac{1}{2E_0} \lim_{\epsilon \rightarrow 0} \left( \frac{1}{\epsilon} \left[ u_i(t) + \epsilon \delta u_i(t), u_i(t) + \epsilon \delta u_i(t) \right] - \frac{1}{\epsilon} \left[ u_i(t), u_i(t) \right] \right) - \left[ \frac{\partial(\delta u_i)}{\partial t} \right. \\ &\quad \left. + U_j \frac{\partial(\delta u_i)}{\partial x_j} + u_j \frac{\partial(\delta u_i)}{\partial x_j}, v_i \right] + \left[ \delta u_j \frac{\partial(u_i + U_i)}{\partial x_j}, v_i \right] + \left[ \frac{1}{Re} \frac{\partial}{\partial x_j} \left( \frac{\partial \delta u_i}{\partial x_j} \right. \right. \\ &\quad \left. \left. + \frac{\partial \delta u_j}{\partial x_i} \right), v_i \right] - \left[ \delta u_j \frac{\partial(T + \bar{T} + T_0)}{\partial x_j}, \tau \right] - \left[ \frac{\partial \delta u_i}{\partial x_i}, q \right] - \langle \delta u_i(0), v_{0,i} \rangle. \end{aligned} \quad (2.30)$$

We can again make use of multidimensional integration by parts and expand the volume and time integrals as defined in (2.25). This will generate surface integral terms as in (2.29).

### (c) Variation with temperature

$$\frac{\delta \mathcal{L}}{\delta T} \cdot \delta T = \left[ Ri_b n_i \delta T, v_i \right] + \left[ \frac{\partial \delta T}{\partial t} + (U_j + u_j) \frac{\partial \delta T}{\partial x_j} - \frac{1}{Re Pr} \frac{\partial^2 \delta T}{\partial x_j^2}, \tau \right] - \langle \delta T(0), \tau_0 \rangle. \quad (2.31)$$

### (d) Variation with initial velocity

$$\frac{\delta \mathcal{L}}{\delta u_{0,i}} \cdot \delta u_{0,i} = \langle \delta u_{0,i}, v_{0,i} \rangle. \quad (2.32)$$

## 2.7 Adjoint Equations

At the maximum of the cost functional and hence  $\mathcal{L}$ , all the above first derivatives of  $\mathcal{L}$  go to zero identically. Equating the surface integrals to zero we obtain that the adjoint velocity and pressure also satisfy the homogeneous boundary conditions similar to the direct variables, i.e., no-slip on walls and periodic in unbounded directions. Equating other independent integrals give us the adjoint equations and the initial and final conditions of the adjoint variables. The adjoint equations are as follows.

### Adjoint continuity equation (from variations with pressure)

When adjoint velocity  $v_i$  satisfies the boundary conditions of the direct velocity, equating the volume integral in equation (2.29) to zero, we get

$$\frac{\partial v_i}{\partial x_i} = 0. \quad (2.33)$$

That is, the adjoint velocity is also incompressible similar to the direct velocity.

### Adjoint velocity equation (from variations with velocity)

When variations with respect to velocity in (b) above are set to zero, we get the following equation which is the adjoint momentum equations

$$\begin{aligned} \frac{\partial v_i}{\partial t} + v_j \frac{\partial(u_j + U_j)}{\partial x_i} + \frac{\partial(v_i(U_j + u_j))}{\partial x_j} + \frac{1}{Re} \frac{\partial}{\partial x_j} \left( \left( \frac{\partial v_i}{\partial x_j} \right. \right. \\ \left. \left. + \frac{\partial v_j}{\partial x_i} \right) \right) - \tau \frac{\partial(T + \bar{T} + T_0)}{\partial x_i} + \frac{\partial q}{\partial x_i} + \frac{1}{E_0} u_i = 0, \end{aligned} \quad (2.34)$$

The diffusion term above (involving Reynolds number) has opposite sign to that of the diffusion term in direct equation (2.15) and hence the time marching of the above equation is well-posed only when the sign of time is reversed, i.e., backward time evolution. Another particular interesting quality of this equation is that despite the direct momentum equations being nonlinear, this adjoint equation is linear in adjoint velocity.

We also obtain the adjoint initial and final conditions as

$$-\frac{1}{\mathcal{T}} v_i(\mathcal{T}) = 0, \quad (2.35)$$

$$v_{0,i} - \frac{1}{\mathcal{T}} v_i(0) = 0, \quad (2.36)$$

### Adjoint temperature equation (from variations with temperature)

Similarly from (c) above we have the adjoint temperature equation as

$$\frac{\partial \tau}{\partial t} + Ri_b n_i v_i + \frac{\partial(\tau(U_j + u_j))}{\partial x_j} + \frac{1}{RePr} \frac{\partial^2 \tau}{\partial x_j^2} = 0, \quad (2.37)$$

and we also obtain the adjoint initial and final temperature conditions as

$$\frac{1}{\mathcal{T}} \tau(\mathcal{T}) = 0, \quad (2.38)$$

$$\tau_0 - \frac{1}{\mathcal{T}} \tau(0) = 0. \quad (2.39)$$

### Sensitivity to initial condition

At optimality, equating the derivative of Lagrangian with respect to the initial condition as in (d), we get

$$\frac{\delta \mathcal{L}}{\delta u_{0,i}} = v_{0,i} := 0. \quad (2.40)$$

$u_{0,i}$  is the only control parameter in this optimisation routine. Only at optimality, this variation with respect to initial condition goes to zero. If the initial condition is not the optimal condition, for the current choice of cost functional, this derivative is precisely the adjoint velocity at time  $t = 0$ . This would, however, not hold when we change the cost functional as then the derivative with respect to the initial condition would change because the Lagrangian would be different. So, when we start with a random noise as in the loop shown in figure 2.2, we will of course be far away from optimality. Hence,  $v_{0,i} > 0$  for any random guess. This provides us with the direction of descent in which we need to update our guess such that we move closer to the optimal condition. This update is done using a rotation technique as in section 2.8. This whole procedure forms the optimisation in time for the Navier-Stokes and temperature equations and can be summarised as below.

### 2.7.1 Looping algorithm for Navier-Stokes

- Start with a guess of the initial perturbation  $u(0)$ . This is mostly a random noise.
- Solve the direct equations for momentum (2.15) subject to the incompressibility condition (2.14), and the temperature equation (2.16) from time  $t = 0$  to  $t = \mathcal{T}$ .
- ‘Initialise’ the adjoint velocity  $v_i$  and temperature  $\tau$  at time  $\mathcal{T}$  from (2.35) and (2.38).
- Integrate backwards in time from  $t = \mathcal{T}$  to  $t = 0$  the adjoint equations for momentum (2.34) subject to incompressibility (2.32), and the temperature equation (2.37).
- Check if the gradient with respect to the initial conditions in equation (2.40) is zero. Otherwise, it provides the next guess for the optimal perturbation and we update our guess as in section 2.8.
- When the gradient in equation (2.40) is zero, we have the optimal condition that maximises the cost functional  $\mathcal{J}(\mathcal{T})$  in equation (2.22) which represents the time-integrated energy growth in  $t \in [0, \mathcal{T}]$ .

This time-looping optimisation algorithm is same as the looping schematic shown in figure 2.2 but now we have provided the exact equations that needs to be solved to complete this iteration for the fluid equations. This optimisation procedure has been termed direct-adjoint looping. Another constraint that is missing in the constrained Lagrangian in equation (2.24) is the imposition of a fixed initial perturbation kinetic energy  $E_0$ . This could have been done with a Lagrange multiplier in equation (2.24), but that has been found to be numerically expensive and delicate (Foures et al., 2013). Hence, only during the update of the initial perturbation as in the section 2.8 below, this constraint of a fixed  $E_0$  is imposed.

It is underlined here that this procedure is applicable to any perturbation amplitude and hence applies equally well to both linear and nonlinear equations. Whether or not nonlinear mechanisms will be important will depend on  $E_0$ . With  $E_0 = \mathcal{O}(10^{-2})$ , as used in nonlinear optimisation studies of Cherubini et al. (2010); Vermach and Caulfield (2018),

this whole procedure would be a nonlinear optimisation problem as the perturbations are only an order of magnitude smaller than the laminar base flow.

### 2.7.2 Change in cost functional

The cost functional as defined in equation (2.22) consists only of the time-averaged perturbation kinetic energy. By including the potential energy of the flow, we can form a new cost functional

$$\mathcal{J}_b(\mathcal{T}) = \frac{1}{E_0\mathcal{T}} \int_0^{\mathcal{T}} E(t)dt + \frac{1}{2V} \int_V Ri_b \frac{T(t)^2}{T_{ref}(t)^2} dV. \quad (2.41)$$

With the choice of this cost functional, the adjoint momentum and temperature equations can be derived using the same algorithm as above. We arrive at the same adjoint momentum and temperature equations as in (2.34) and (2.37). We also arrive at the same momentum initial conditions as in equation (2.35). However, the adjoint temperature initial condition (at  $t = \mathcal{T}$ ) with  $\mathcal{J}_b(\mathcal{T})$  as the cost functional changes to (compare with (2.38))

$$\frac{Ri_b}{E_0 T_{ref}^2} T(\mathcal{T}) - \frac{1}{\mathcal{T}} \tau(\mathcal{T}) = 0. \quad (2.42)$$

The choice of cost functional would depend on the problem of interest and there could be various combinations of kinetic and potential energy (e.g., Vermach and Caulfield (2018)) that could lead us to uncover interesting dynamics of the flow. However, for the rest of the chapter and next, we stick to  $\mathcal{J}(\mathcal{T})$  as defined in (2.22) as the cost functional of choice.

## 2.8 Optimisation

The aim of this section is to reach the optimal perturbation using a rotation technique and a conjugate gradient method such that equation (2.40) is zero. To find the optimal perturbation within a set numerical tolerance, we have to iterate repeatedly and gradually march according to the gradient information and monitor a residual (which is equivalent to the gradient defined in (2.40) but suited for this update method), as defined in other studies like Vermach and Caulfield (2018), which denotes whether we have converged to

the actual optimal or not.

We also have to ensure in this step that the initial energy of the perturbations  $E_0$  is constant during each update of our guess of  $u_{0,i}$ . We maximise the cost functional and hence  $\mathcal{L}$  in equation (2.24) such that at optimality,

$$\frac{\delta \mathcal{L}}{\delta u_{0,i}} = v_{0,i} := 0. \quad (2.43)$$

To enforce the initial energy constraint and hence keep the perturbation amplitude constant, we try (numerically) to stay on a  $\zeta$  dimensional hypersphere as shown for  $\zeta = 3$  in figure 2.3. This method has been applied to Navier-Stokes optimisation problems, e.g., by Foures et al. (2013). The dimension  $\zeta$  is the dimension of a particular variable, and in this case is the combined dimension of the velocity variable in all the grid points. The initial energy of the perturbations  $E_0$  is proportional to the square of the radius of the  $\zeta$ -dimensional hypersphere. To simplify this geometric method of initial energy constraint and update of initial conditions, we look only at a great hypercircle (figure 2.4) of the  $\zeta = 3$  hypersphere (figure 2.3). The gradient at each time step as in equation (2.40), which is the adjoint variable  $v_0$  at time  $t = 0$ , gives the direction in which we need to update to get to the optimal. A schematic of this update via rotation of the initial condition is shown in figure 2.4.

With reference to figure 2.4, to make sure the new update  $\mathbf{u}'_i$  lies on the hypersphere, we remove the hypersurface normal, i.e., the component of  $v_0$  along  $\mathbf{u}_0$  and we are left with  $v_0^\perp$ , as

$$v_0^\perp = v_0 - \frac{(u_0, v_0)}{(u_0, u_0)} u_0. \quad (2.44)$$

And then to ensure that we have the same initial energy  $E_0$ , we normalise this gradient and then scale it by the radius of the hypersphere (which is proportional to the square root of energy  $E_0$ ) as

$$R = (E_0)^{1/2} \frac{v_0^\perp}{\|v_0^\perp\|}. \quad (2.45)$$

We can then update the initial condition by rotating it by an angle  $\theta_j$

$$u'_j = u_{0,i} \cos \theta_j + R \sin \theta_j, \quad (2.46)$$

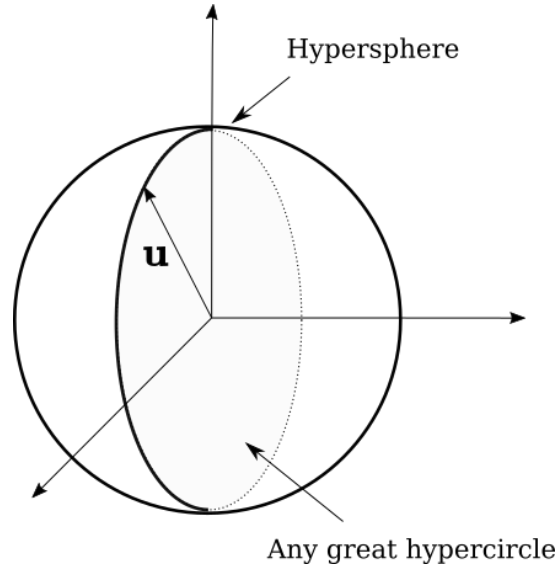


Figure 2.3: A  $\zeta = 3$  dimensional energy hypersphere with the velocity field  $\mathbf{u}$  as the radius. (After Foures et al. (2013, Fig 11).)

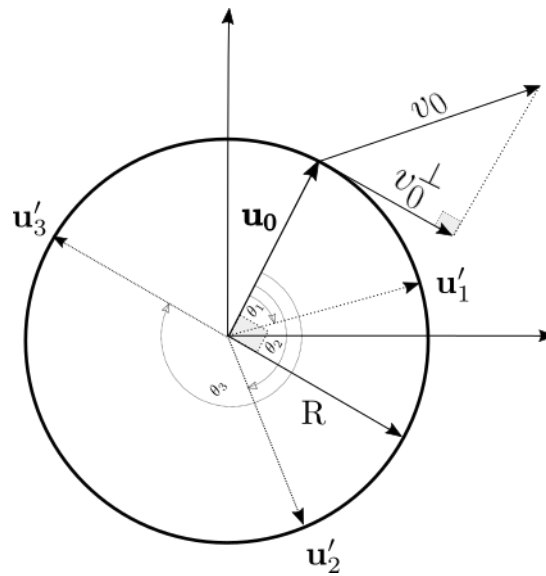


Figure 2.4: The great hypercircle from figure 2.3 shows the update procedure to find a better guess of the optimal by rotation.

where  $u_{j=1,2,3,\dots,N}$  are the updates corresponding to choice of angle  $\theta_j$ . This technique is combined with conjugate gradient algorithm (Polak, 1971) for a robust update. This is done by redefining the descent direction  $R$  as  $\mathcal{R}$  in every iteration ( $n$  denoting iteration number),

$$\mathcal{R}_n = R_n + \beta_n \mathcal{R}_{n-1}^\perp. \quad (2.47)$$

$\beta_n$  at every iteration is given by Polak-Ribiere formula (Polak and Ribiere, 1969)

$$\beta_n = \frac{(R_n, (R_n - R_{n-1}))}{(R_{n-1}, R_{n-1})}, \quad (2.48)$$

and the initial value (i.e., in the first iteration) of  $\mathcal{R}_{n=0} \equiv \mathcal{R}_0 = R_0$ .

And then update the velocity field as,

$$u'_j = u_{0,i} \cos \theta_j + \mathcal{R} \sin \theta_j. \quad (2.49)$$

We still have an unknown variable  $\theta_j$  which is chosen with a line search algorithm (Den- nis Jr and Schnabel, 1996). This amounts to first updating the direct variables at  $t = 0$  after the  $n^{th}$  iteration by an angle  $\theta_j$ , between  $0^\circ$  and  $360^\circ$  as

$$u_i^{n+1} = u_i^n \cos \theta_j + \mathcal{R}_n \sin \theta_j. \quad (2.50)$$

The next step involves evolving the direct equations with  $u_i^{n+1}$  for each update angle  $\theta_j$  and noting the cost functional  $\mathcal{J}(\mathcal{T})$ . The update angle that provides the largest cost functional is chosen as our desired update angle  $\theta_{max}$ . The whole optimisation procedure continues with the final updated guess:

$$u_i^{n+1} = u_i^n \cos \theta_{max} + \mathcal{R}_n \sin \theta_{max}. \quad (2.51)$$

We generally have to do this iteration in time a few number of times to reach the optimal. To have an idea of how ‘far’ we are from the optimal after an update, we monitor the residual following Rabin et al. (2012). This is the normalised gradient of the Lagrangian with respect to the initial velocity but projected onto a plane tangent to the hypersphere defined as

$$r = \frac{\|\nabla_{u_0} \mathcal{L}^\perp\|^2}{\|\nabla_{u_0} \mathcal{L}\|^2}. \quad (2.52)$$

Following recent works (e.g. Vermach and Caulfield (2018)), when the residual is  $\mathcal{O}(10^{-3} - 10^{-4})$ , we decree the optimiser to have found the optimal perturbation that maximises the cost functional.

### 2.8.1 Trusting the optimal

As we approach optimality, the need for higher accuracy schemes and how well we can calculate the gradients become increasingly important. This means it gets harder and harder to approach the ‘true’ optimal (i.e. one found with infinite accuracy), when we are near it. We also cannot claim to have found the global optimal but what the optimal we have converged to would be a local in a certain region of the energy landscape. To have some confidence in our optimal, we start with different random noise. If we converge to the same optimal, we assume it to be a robust one. It might also be the case that we may be stuck at an optimal where small variations produce the same cost functional (within numerical tolerance) and hence numerically not resolvable. Nonlinear optimisation is inherently non-convex (Kerswell, 2018) and attaining a global maximum cannot be concluded with certainty. This will, however, keep the main aim of the optimisation true, i.e. we converge to optimal disturbances, which will later be shown to be organised structures, even when the guess was an absolute random noise. For a non-dimensionalised channel of streamwise length  $2\pi$ , spanwise length  $\pi$ , and channel height 2, it is noted that we optimise for  $\mathcal{O}(10^6)$  variables and hence this procedure could be termed as a highly-intensive numerical search.

The whole set of equations is solved for a channel flow in this thesis using numerical techniques as described below. For the highest  $E_0 = 10^{-2}$ , we obtain the same nonlinear optimal with our solver as in Vermach and Caulfield (2018) and the structures are shown later in this chapter. Given that both are nonlinear optimisation problems solved on independently written solvers (Vermach and Caulfield (2018) is based on *Diablo* (Taylor, 2008)), this provides a very strong validation of our solver.

On the other hand, with a small  $E_0$  of  $\mathcal{O}(10^{-8})$ , nonlinear mechanisms remain unimportant throughout our chosen time horizon, perturbations being several orders of magnitude smaller than the laminar base flow, and their products vanishingly small. It takes  $\mathcal{O}(100)$  iterations to converge to the nonlinear optimal perturbation ( $E_0 = 10^{-2}$ ), similar to what is noted in Vermach and Caulfield (2018), while it takes less than 50 iterations to converge to the linear optimal perturbation when starting from random initial conditions as guesses. This ease of convergence to the linear optimal has also been reported in the studies cited earlier. We find that even when we solve the viscosity-stratified equations

as in the next chapter, this convergence remains similar.

## 2.9 Numerical method

We describe here the numerical techniques used in developing the three-dimensional Navier-Stokes and adjoint Navier-Stokes solver in a channel. We also solve the temperature equation and its adjoint. The solver we describe here is a fully nonlinear and capable of parallel computation (using OpenMP) and has been used for the nonlinear nonmodal analysis. It employs the rotation technique of nonlinear optimisation to numerically calculate the optimal of time-integrated perturbation kinetic energy. We discuss the spatial discretisation and the time integration schemes used in the solver. Bewley (2012, p 413-432) describes in much detail the numerical method for solving the unstratified Navier-Stokes equations. For all the analysis, we use a nondimensional size of  $L_x = 2\pi$ ,  $L_y = 2$ , and  $L_z = \pi$  in which the streamwise extent is smaller than in Vermach and Caulfield (2018), while the spanwise extent is the same. Our channel in  $x$  and  $y$  direction is the same as in the 2D study of Foures et al. (2013). The direct and adjoint equations solver and the optimiser have been written from scratch in Fortran.

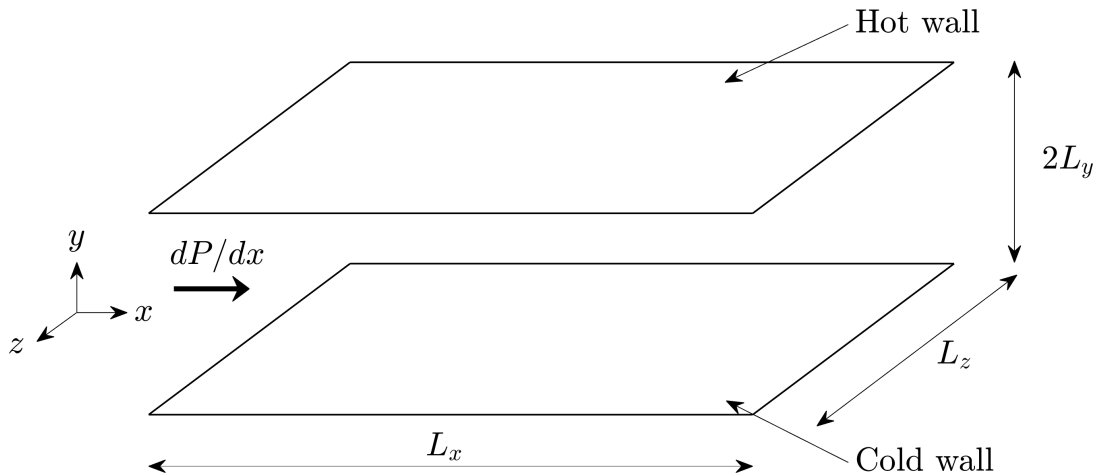


Figure 2.5: The domain of integration with the pressure gradient  $dP/dx$  directing the mean flow towards the positive  $x$  direction. The top wall is always hotter than the bottom wall. The  $x$  and the  $z$  directions are periodic at the domain boundaries.

### 2.9.1 Homogeneous directions

The equations are numerically solved in a domain as shown in figure 2.5. The  $x$  and  $z$  directions are the homogeneous directions. We define periodic boundary conditions on both of these directions. Wavenumbers in the homogeneous directions are

$$kx = 2\pi/Lx \quad \text{and} \quad kz = 2\pi/Lz. \quad (2.53)$$

The gradients in the velocity and temperature fields are higher with nonlinear initial energy ( $E_0 = 10^{-2}$ ) when compared to linear initial energy ( $E_0 = 10^{-8}$ ). Hence in  $x$ ,  $y$ , and  $z$ , we use  $100 \times 209 \times 50$  grid points for  $E_0 = 10^{-2}$ , while we use  $50 \times 209 \times 25$  grid points for  $E_0 = 10^{-8}$ . This makes the grid spacing in the  $x$  and  $z$  directions equal, at 0.06 for  $E_0 = 10^{-2}$  and at 0.12 for  $E_0 = 10^{-8}$ .

### 2.9.2 Wall normal direction

The wall normal or the  $y$ -direction is discretised into a staggered combination of base and fractional grids (see e.g. Bewley (2012)). The base grid points ( $y_j$ ) are shown as filled black squares and labelled in blue and the fractional grid points ( $y_{j+1/2}$ ) are shown as black crosses and labelled in red in figure 2.6. There are a few ghost points (0, 1, and NY+1 in base grid and 0 and NY+1 in fractional grid) which are used only during wall-normal derivative calculations. The grid points are aligned such that the fractional points 1 and NY lie on the top and bottom wall respectively. This is left as a choice and even the base grid could be placed on the walls. The fractional grids are exactly at the mid-location between the base grid points. Hence,

$$y_{j+1/2} = \frac{1}{2}(y_j + y_{j+1}) \quad (2.54)$$

The streamwise ( $x$ ) and spanwise ( $z$ ) velocities, pressure, and temperature are discretised on the fractional grid and the wall-normal velocity ( $v$ ) on the base grid.

A hyperbolic tangent function

$$y_j = \tanh \left( k \left[ \frac{2(j-1)}{N_Y} - 1 \right] \right), \quad j = 1, 2, \dots, N_Y, \quad (2.55)$$

where  $N_Y$  is the number of grids in the wall-normal direction, is used to cluster both the

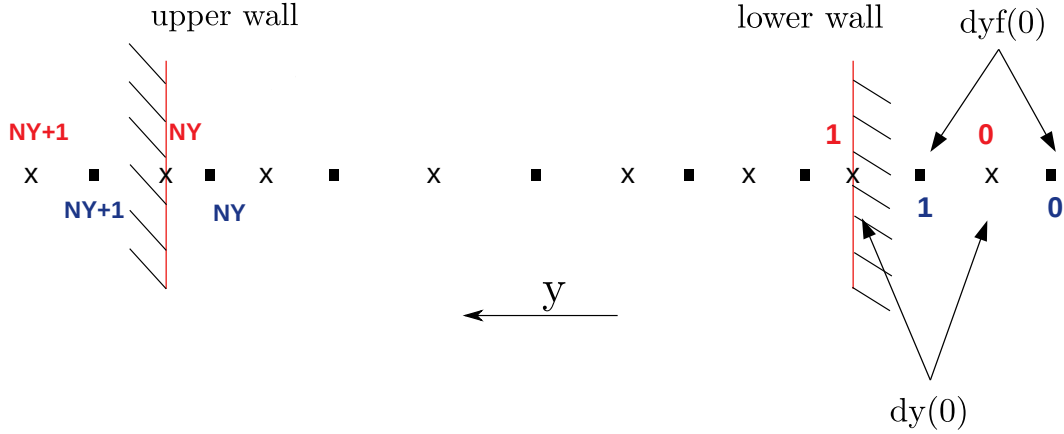


Figure 2.6: The base (solid squares) and fractional (crosses) grid in the  $y$  direction. Both the grids are clustered towards the walls. The distance between adjacent fractional grid points is  $dy$  while the distance between adjacent base grid points is  $dyf$ .

fractional and the base grid points towards the walls. This is to make sure that we are able to capture the small scale near wall dynamics because gradients become high towards the walls. The value of  $k$  in equation (2.55) has been kept constant at 1.5 and it creates a  $y$ -grid with  $\Delta y_{max} = 0.0159$  (near the centre of the channel) and  $\Delta y_{min} = 0.0029$  (near both the walls).

The wall normal spatial derivatives are computed using second order central finite difference method. The spatial derivatives in  $x$  and  $z$  are calculated using Fast-Fourier transform and we truncate the Fourier series using the 2/3-rule to prevent aliasing (see e.g. Canuto et al. (2007)).

### 2.9.3 Temporal Discretisation

We employ a time-stepping algorithm which is a combination of an explicit method (Runge-Kutta-Wray) for the nonlinear (convective) terms and an implicit method (Crank-Nicolson) for the linear (viscous) terms and the wall-normal derivatives.

If we have a partial differential equation of form

$$\frac{\partial \phi}{\partial t} = N(\phi) + A(\phi), \quad (2.56)$$

where  $N(\phi)$  have the terms that need to be treated explicitly and  $A(\phi)$  have terms that

need to be handled implicitly,  $A(\phi)$  must be either linear or linearised appropriately.

The time advancement scheme we use requires three sub-steps for a  $\Delta t$  advancement in time from  $t \rightarrow t + \Delta t$  and they can be compactly written as

$$\phi^{rk} = \phi^{rk-1} + \gamma_{rk}\Delta t N(\phi^{rk-1}) + \zeta_{rk}\Delta t N(\phi^{rk-2}) + \alpha_{rk}\Delta t \frac{A(\phi^{rk}) + A(\phi^{rk-1})}{2}. \quad (2.57)$$

Where the coefficients are specific to this numerical scheme and are (Bewley, 2012),

$$\gamma_1 = \frac{8}{15}, \gamma_2 = \frac{5}{12}, \gamma_3 = \frac{3}{4}, \zeta_1 = 0, \zeta_2 = -\frac{17}{60}, \zeta_3 = -\frac{5}{12}, \alpha_1 = \frac{8}{15}, \alpha_2 = \frac{2}{15}, \alpha_3 = \frac{1}{3}. \quad (2.58)$$

We will consider the terms involving spatial derivatives in the  $x$  and  $z$  directions (parallel to the wall) explicitly as they are calculated spectrally. It is not impossible to treat them implicitly as one could write the spectral derivatives as a product with spectral derivative matrix. However, such a matrix will be dense and hence inverting it would not be efficient. Also, due to the stretched grid used, the grid size is largely reduced near the wall (i.e.,  $\Delta y$  becomes smaller). This would require a very small step size  $\Delta t$  for numerical stability if  $y$ -derivatives are treated explicitly. Hence, the terms involving the wall normal derivatives are treated implicitly. In the solver, the scalar equation is solved first, followed by the  $y$ -momentum equation. The  $x$ - and  $z$ - momentum equations are solved simultaneously at the end. As the equations are sequentially solved, some of the terms are available for the next equations to be treated implicitly during time evolution.

### Momentum Equations

The momentum equations with this combination of Runge-Kutta-Wray and Crank-Nicolson scheme can be written as,

$$\begin{aligned} \mathbf{u}^{rk} = & \mathbf{u}^{rk-1} + \gamma_{rk}\Delta t N(\mathbf{u}^{rk-1}) + \zeta_{rk}\Delta t N(\mathbf{u}^{rk-2}) + \alpha_{rk}\Delta t \frac{A(\mathbf{u}^{rk}) + A(\mathbf{u}^{rk-1})}{2} \\ & - \alpha_{rk}\Delta t \frac{\delta p^{rk-1}}{\delta x_i} - \alpha_{rk}\Delta t \frac{\delta q}{\delta x_i} \end{aligned} \quad (2.59)$$

where

$$q := p^{rk} - p^{rk-1} \quad (2.60)$$

A fractional step strategy is employed to break the momentum equation into two distinct steps. The first step involves neglecting the influence of the term  $\delta q/\delta x_i$  and calculating an intermediate velocity field  $\mathbf{v}^{rk}$  with the same boundary conditions as  $\mathbf{u}$ .

$$\mathbf{v}^{rk} = \mathbf{u}^{rk-1} + \gamma_{rk}\Delta t N(\mathbf{u}^{rk-1}) + \zeta_{rk}\Delta t N(\mathbf{u}^{rk-2}) + \alpha_{rk}\Delta t \frac{A(\mathbf{v}^{rk}) + A(\mathbf{u}^{rk-1})}{2} - \alpha_{rk}\Delta t \frac{\delta p^{rk-1}}{\delta x_i}, \quad (2.61)$$

and then update the velocity by adding this neglected pressure update term  $q$  as

$$\mathbf{u}^{rk} = \mathbf{v}^{rk} - \alpha_{rk}\Delta t \nabla q. \quad (2.62)$$

This pressure update  $q$  is calculated such that the updated velocity field  $\mathbf{u}^{rk}$  is divergence free as

$$\nabla \cdot (\mathbf{u}^{rk}) = 0 = \nabla \cdot (\mathbf{v}^{rk}) - \alpha_{rk}\Delta t \nabla^2 q. \quad (2.63)$$

This is ensured by defining  $q$  as the solution of the Poisson equation (2.64) solved with homogeneous Neumann boundary conditions on  $q$

$$\nabla^2 q = \frac{1}{\alpha_{rk}\Delta t} \nabla \cdot (\mathbf{v}^{rk}). \quad (2.64)$$

The pressure at the current time step  $rk$  is then updated as

$$p^{rk} = p^{rk-1} + q. \quad (2.65)$$

## 2.9.4 Run-time of the code

About 40% of the run-time of the solver is due to input-output processes to the machine hard disk. This is after optimising for cache misses. We employ a pseudo-spectral method in which the nonlinear terms are not calculated in the Fourier space. We first inverse transform the complex fields in the Fourier space to real space, multiply them in the real space, and again transform the product into the Fourier space. These Fourier transform take up significant amount of time and of course scales with the number of grid points. We have optimised for the number of Fourier transforms in our solver. The adjoint equations contain more terms to be calculated and hence backward time marching is slower than the forward time marching. While marching backwards in time from  $t = \mathcal{T}$  to  $t = 0$ , we also need information of the direct velocity fields at each and every time

step. This is required for calculating the product of direct and adjoint velocities. It means that we have to store the real velocities in the computer memory or hard disk, and it presents a huge computational challenge given that we solve the equations in a three-dimensional channel. Also, as illustrated in figure 2.7, the time marching scheme that we have adopted involves an unequal subdivision of the time-step in both the directions. So, while marching backwards we do not encounter direct velocities at the corresponding time step. So during “adjoint iteration” as in figure 2.7, we do a linear interpolation to calculate the direct velocities at the location of red dots from the black dots. We tried a cubic spline interpolation technique but it renders the solver numerically unstable.

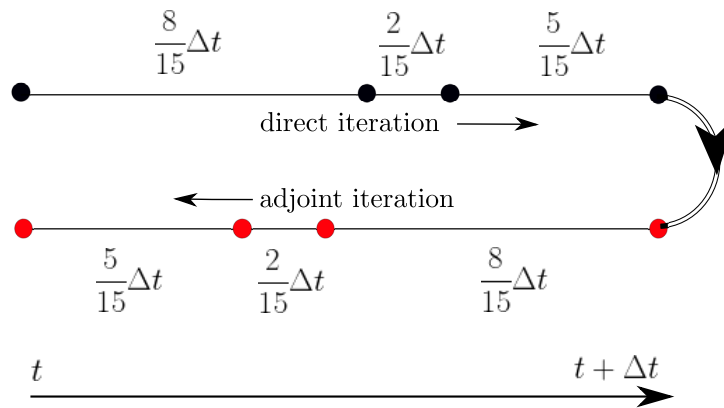


Figure 2.7: Only a looping in  $[t, t + \Delta t]$  is shown to explain the interpolation. The RKW3/CN time stepping in both the direction divides a time step ( $\Delta t$ ) into three unequal subdivisions. The sum of all the subdivisions is  $\Delta t$ . The black dots are the locations where we store the direct velocities.

### 2.9.5 Parallel processing using OpenMP

OpenMP is a programming interface for shared memory processing. This means the threads (of computer cores) of computation should be using the same physical memory (random access memory (RAM)). OpenMP suffices for our purpose because our memory requirement is within the available single RAM capability at the ICTS supercomputing facility. For more memory intensive operations, distributed memory sharing interface like the message passing interface (MPI) would be required for parallel computing. A certain section of Thomas matrix algorithm for matrix solution is shown below to show the use of OMP directives. A, B, C, and D are three dimensional matrices. The `!$OMP PARALLEL`

starts the parallel processing by allowing a processor thread to act as a master and others as ‘slaves’ to the master thread. `!$OMP END PARALLEL` is the directive to end the parallel process and the operations after that are done only on a single thread. It is advisable to use the `!$OMP DO` directive separately from the `!$OMP PARALLEL` directive. The `!$OMP END DO` directive ends the parallel do-loop. The `NO WAIT` clause turns off synchronisation among threads. It is also advisable to iterate the matrix indices in reverse order (i.e the K loop before J loop, and I loop as the innermost loop) to avoid cache misses and thereby speed up calculations.

```
!$OMP PARALLEL
  DO K = 2,NY-1
!$OMP DO
  DO J = 1, NZ
  DO I = 1, NX/2+1
    C(I,J,K) = C(I,J,K)/(B(I,J,K)-A(I,J,K)*C(I,J,K-1))
    D(I,J,K) = (D(I,J,K)-A(I,J,K)*D(I,J,K-1))/(B(I,J,K)-A(I,J,K)*C(I,J,K-1))
  END DO
  END DO
!$OMP END DO NOWAIT
  END DO
!$OMP END PARALLEL
```

## 2.10 Outputs: optimal structures

After the detailed exposition of the whole theory of nonmodal analysis and the numerical technique used for the same, we show some output of the whole process of optimisation. For a fixed optimisation time of  $\mathcal{T} = 8$ , we find that the optimal disturbances are oblique vortices on both the walls of the channel as shown in figure 2.8. These structures have been obtained from absolute random noise and are responsible for maximum time-integrated energy growth in the channel at the specified parameters.

The convergence of the optimisation routine is shown in figure 2.9. We see that the residual has reached values  $< \mathcal{O}(10^{-4})$  in (a). When the residual goes to such low

values, the angle of update  $\theta$  defined in earlier sections, also go to zero (within numerical tolerance) as shown in (c). This means there is no update angle  $\theta$  that can be chosen by the optimiser as we have already found the optimal disturbance. The cost functional as shown in (b) is a measure of the nonmodal growth and is seen to continuously increase until the optimiser finds the optimal when the nonmodal growth is the highest. This was the ultimate aim of the optimiser we started with, i.e., to find the structure or disturbance that causes maximum nonmodal energy growth. We also compare the linear and nonlinear optimal disturbances in figure 2.10 for the same optimisation time of  $\mathcal{T} = 4$  and for subcritical Reynolds number of 500. We see that both the structures vary a lot in that the linear has well defined wavenumbers while the nonlinear optimal is elongated tubes in the  $x$ -direction. It is also to be mentioned that the linear optimal shown in figure 2.10(a) takes  $< 30$  iterations to converge but the nonlinear optimal in figure 2.10(b) takes  $\mathcal{O}(100)$  iterations. In figure 2.11, we show the iteration in progress and how with more number of iterations, we get closer and closer to the actual optimal disturbance. After 10 iterations, when started from random noise, the elongated structures had not formed as can be seen from figure 2.11(a). But by 22 iterations as in (b), some of these disconnected structures get connected and by 100 iterations we have the nonlinear optimal disturbance (figure 2.11(c)).

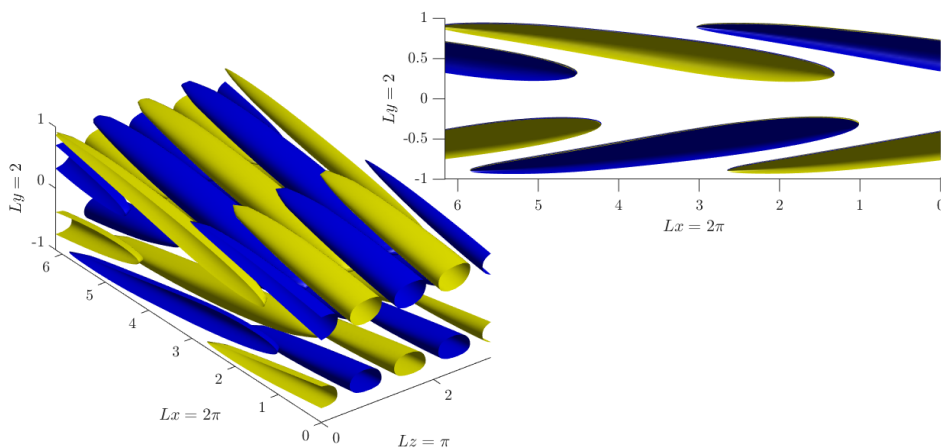


Figure 2.8: Two views of the linear optimal perturbations with  $E_0 = 10^{-8}$ ,  $Re = 500$ , and time of optimisation  $\mathcal{T} = 8$ . The colours are the 40% isosurfaces of the maximum (yellow) and minimum (blue) values of the streamwise velocity ( $u$ ) perturbations.

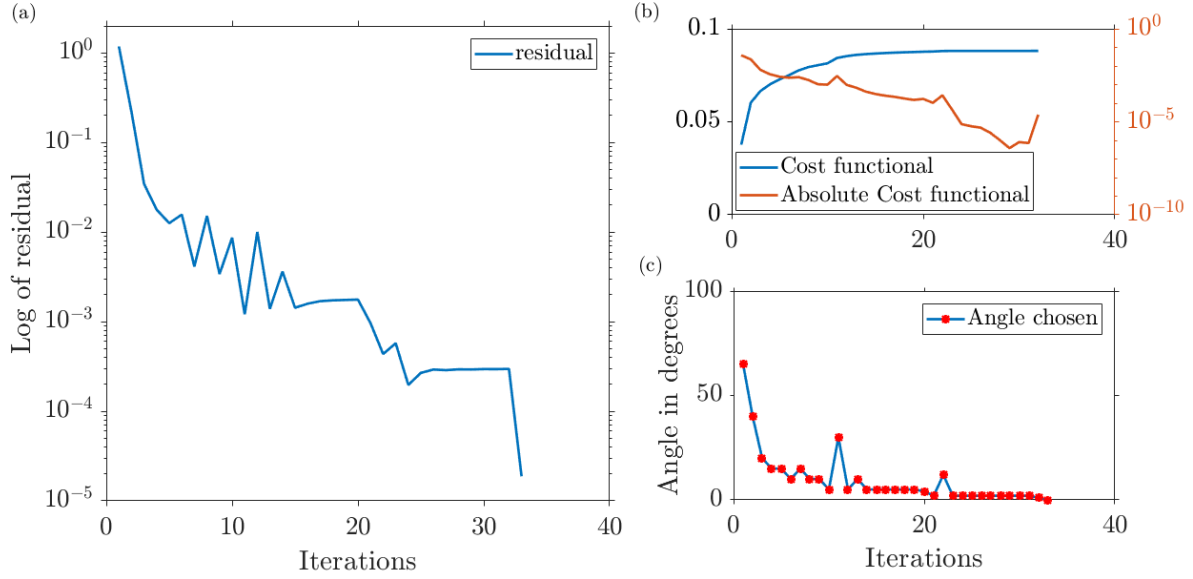


Figure 2.9: (a) The residual as defined in equation (2.52) is shown to go below  $\mathcal{O}(10^{-4})$  value when optimal condition as shown in figure 2.8 is found after 33 iterations. (b) The cost functional (blue) is seen to continually increase and then reach a constant value (within set numerical tolerance) after we find the optimal. The cost functional is the measure of nonmodal energy growth that is brought about by the optimal structure. (c) The angle of update  $\theta$  hits zero (within a numerical tolerance) after we have found the optimal perturbation. The use of a line search to choose  $\theta$  is for the objective function to monotonically increase and residual to continuously decrease.

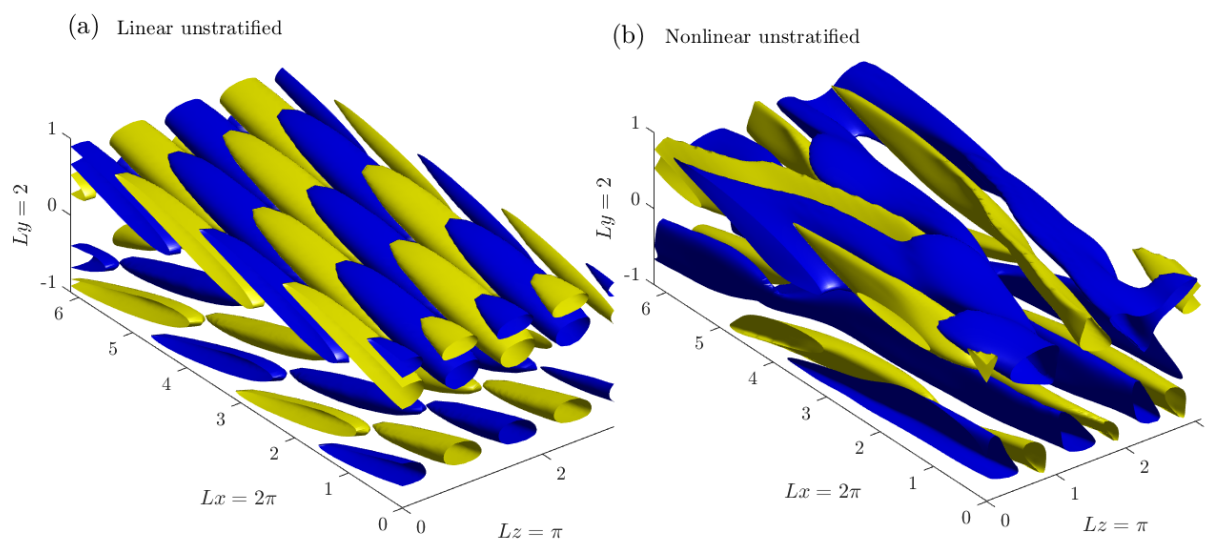


Figure 2.10: (a) Linear optimal and (b) nonlinear optimal perturbations for  $\mathcal{T} = 4$  and  $Re = 500$ . The linear optimal perturbations are oblique vortices whereas the nonlinear optimal perturbations are elongated vortex tubes on both the walls of the channel.

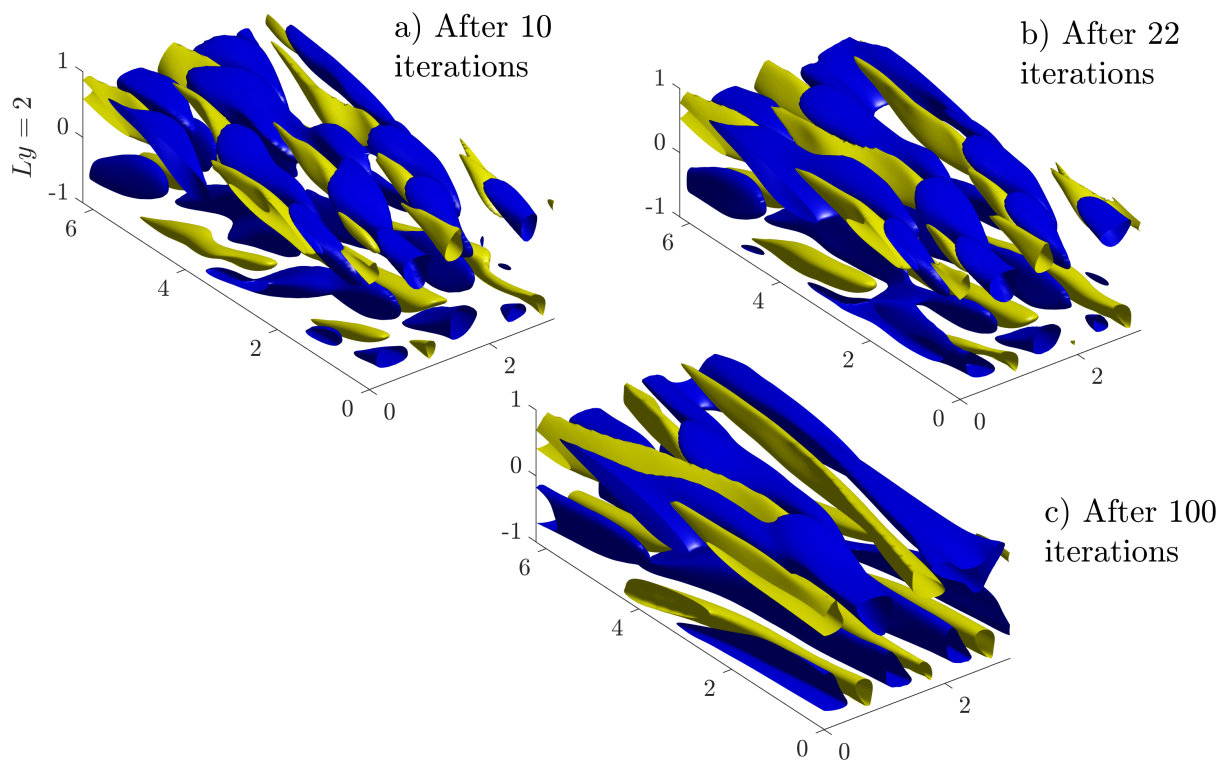


Figure 2.11: The optimisation loop in progress. (a) The nonlinear optimal for  $\mathcal{T} = 4$  after 10 iterations, (b) after 22 iterations and (c) after 100 iterations.

## 2.11 Validation

### 2.11.1 Linear validation

To validate our optimisation (or direct-adjoint looping) solver, we compare our results with the linear global maximum of channel flow for  $Re = 1000$ . The maximum transient growth  $G_{max}(t) = G(t_{max}) \sim 196$  and occurs for  $t_{max} \sim 76$  and is obtained via singular value decomposition of the governing operator (Schmid et al. (2002)). When our solver is run at very low initial energies of  $E_0 = 10^{-8}$ , and when the cost functional is defined as the final-time energy growth, we find streamwise rolls which uses the lift-up mechanism to transiently grow in energy which is much more efficient than the Orr mechanism (lift-up has been briefly described in the previous chapter. Also see Brandt (2014)). We reproduce both the optimal shape and the transient growth as can be seen in figures 2.12 and 2.13. The wavenumbers in  $x$  and  $z$  directions are  $k_x = 0$  and  $k_z \sim 2$ , quantised with respect to the channel dimensions, as predicted by SVD of the governing operator.

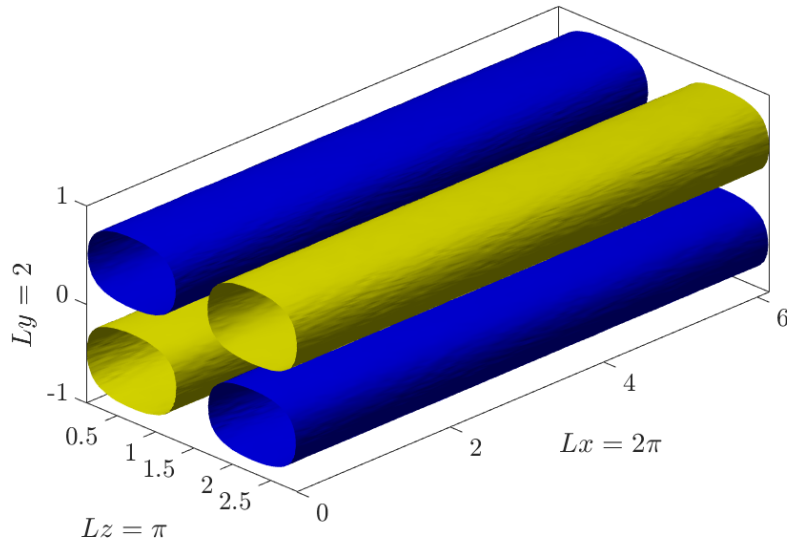


Figure 2.12: Linear global optimal perturbations are streamwise rolls visualised as iso-surfaces of 40% of the maximum (yellow) and minimum (blue) streamwise component of the perturbation velocity.  $Re = 1000$ , time of optimisation  $\mathcal{T} = 76$ .

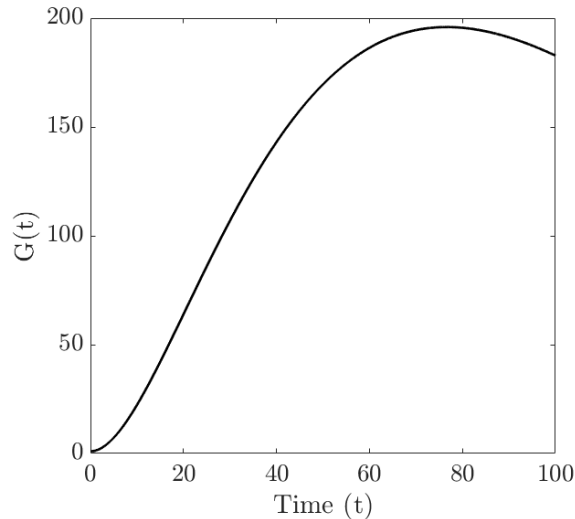


Figure 2.13: Transient energy growth  $G(t) \sim 196$  for the linear optimal in figure 2.12 recovered from our solver. The maximum energy growth occurs at  $t \sim 76$  and the corresponding  $G(t) \sim 196$  as also predicted by SVD.

### 2.11.2 Nonlinear validation

We also need to validate our code at nonlinear energies because we are not yet sure the nonlinear coupling terms (which were suppressed in low-energy case) have been correctly coded. When the direct-adjoint looping is run at a higher initial energy of  $E_0 = 10^{-2}$ , we also recover the unstratified optimal as obtained recently by Vermach and Caulfield (2018) for a channel of  $L_x = 4\pi$ ,  $L_y = 2$ , and  $L_z = \pi$  which incidentally is the only existing study to our knowledge on nonlinear optimal perturbation in unstratified three dimensional channel flow. When we optimise for time-integrated energy maximisation as in Vermach and Caulfield (2018) for a final time of  $\mathcal{T} = 2$ , in an unstratified channel, achieve a  $\mathcal{J}(\mathcal{T})$  of over 93% of that of Vermach and Caulfield (2018) as shown in figure 2.14. When the optimal structure is evolved with the direct equations, the maximum in  $\mathcal{J}(\mathcal{T})$  is obtained at  $t \sim 8.5$  from our solver whereas it occurs at  $t \sim 8.1$  for Vermach and Caulfield (2018). The isosurfaces of the streamwise velocity that we obtain for the nonlinear optimal perturbation with  $E_0 = 10^{-2}$ , closely agree with those of Vermach and Caulfield (2018). In particular, both computations result in optimal perturbations which are elongated in the streamwise direction, with streamwise wavelength far larger than can be accommodated in the channel of  $4\pi$  length, spanwise wavenumber of  $k_z = 6$ , and very similar levels of obliqueness as can be visually inspected in figure 2.15. We

have achieved a very good match with a completely independently developed solver. A check we performed to make sure we have converged to a local optimal is to start from different initial conditions of random noise of the desired amplitude, as well as an optimal perturbation from a different parameter set, to ensure that the optimal perturbations we arrive at are the same within the finite-difference errors ( $O(10^{-4})$ ). Also, given the lack of any other numerical or analytical tool to arrive at the nonlinear optimal, this is probably one of the best validation we can do at present.

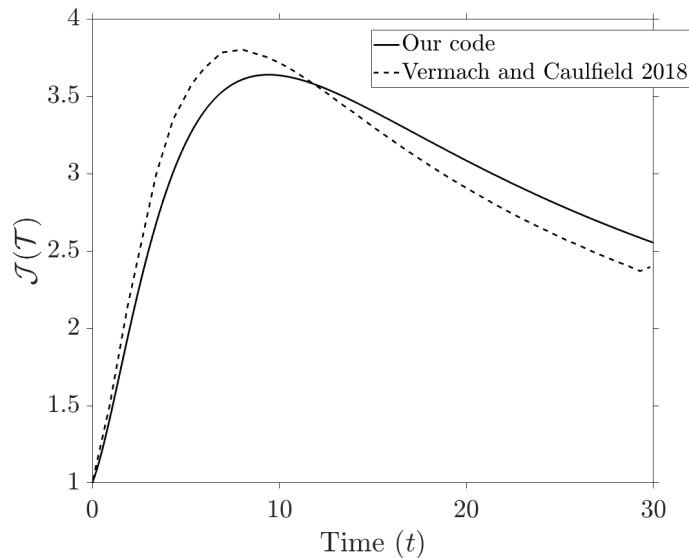


Figure 2.14: Cost functional  $\mathcal{J}(\mathcal{T})$  of the nonlinear unstratified optimal compared with Vermach and Caulfield (2018) for time of optimisation  $\mathcal{T} = 2..$  A perfect match is not expected, as discussed in the text.

The theory of nonmodal analysis and the numerical technique to calculate the optimal disturbances described in this chapter will be used in the next chapter to calculate the viscosity-stratified optimal perturbations. In the sections above we have only shown the optimal disturbances when the flow was unstratified. We will show how the introduction of viscosity stratification changes the qualitative structures of both the linear and the nonlinear optimal perturbations.

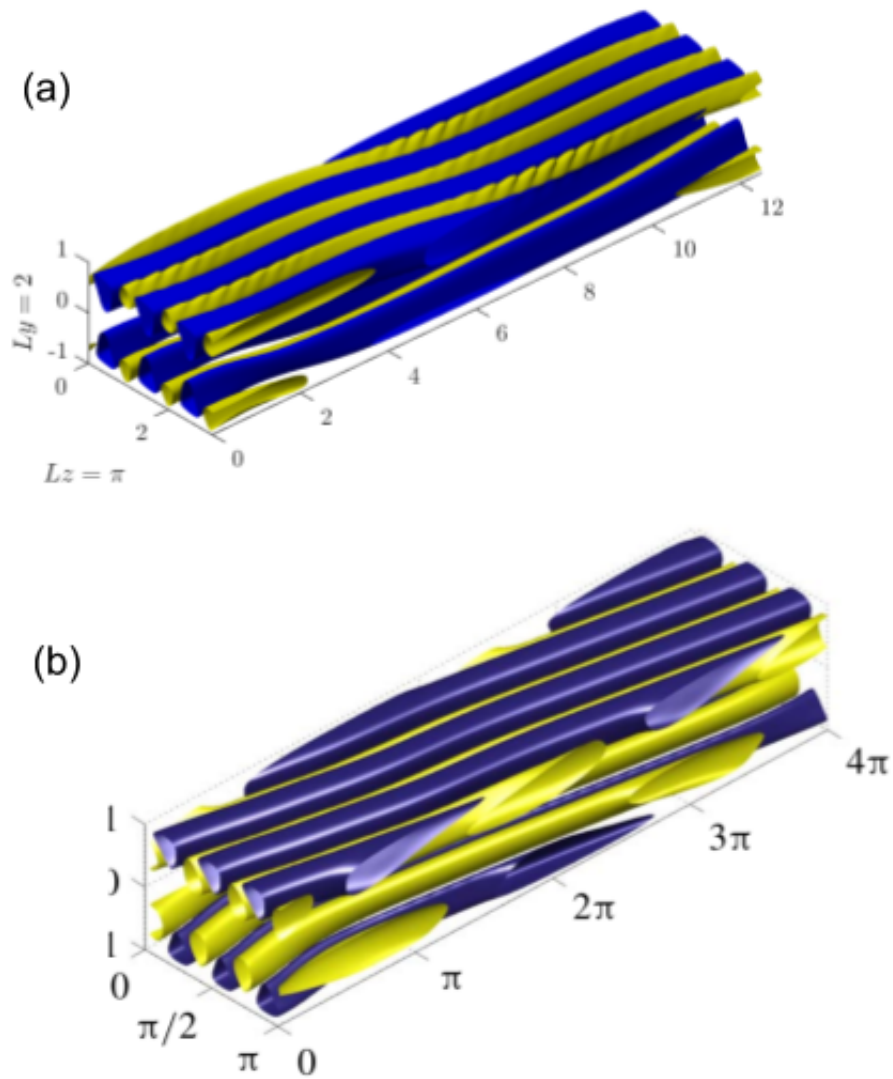


Figure 2.15: (a) Nonlinear optimal perturbations ( $E_0 = 10^{-2}$ ) for  $Re = 500$ , time of optimisation  $t = 2$  in an unstratified channel. (b) Nonlinear optimal perturbations obtained by Vermach and Caulfield (2018) for the same parameters as in (a). Colors mean the same as in figure 2.12.

# Viscosity-stratified optimal perturbations

\*\*\*

This chapter is a modified version of a submitted paper: Thakur, R\*, Sharma, A\*, & Govindarajan, R. Early evolution of optimal perturbations in a viscosity-stratified channel. (\* equal contribution) <https://arxiv.org/abs/2007.03628>

In this chapter, we study the early stages of perturbation growth in a viscosity-stratified flow and how they are different from those in a constant-viscosity flow. We will apply the theoretical and numerical methods developed in the previous chapter to viscosity-stratified flows. We will show how nonlinearity (in velocity perturbations) is a crucial ingredient in this energy growth. We derive the viscosity-varying adjoint Navier-Stokes equations, where gradients in viscosity force both the adjoint momentum and the adjoint temperature. By the technique of direct-adjoint looping as already described in the previous chapter, we obtain the nonlinear optimal perturbations which maximises the perturbation kinetic energy of the nonlinear system. While we study three-dimensional channel flow with the walls at different temperatures, and a temperature-dependent viscosity, our findings are general for any flow with viscosity variations near walls. The Orr and modified lift-up mechanisms are in operation at low and high perturbation amplitudes respectively at our subcritical Reynolds number of 500. The nonlinear optimal perturbation contains more energy on the hot (less-viscous) side, with a stronger initial lift-up.

However, as the flow evolves, the important dynamics shifts to the cold (more-viscous) side, where wide high-speed streaks of low viscosity grow and persist, and strengthen the inflectional quality of the velocity profile. We provide a physical description of this process, and show that the evolution of the linear optimal perturbation misses most of the physics. The Prandtl number does not qualitatively affect the findings. The study of nonlinear optimal perturbations is still in its infancy, and viscosity variations are ubiquitous. We hope that this first work on nonlinear optimal perturbations with viscosity variations will lead to wider studies on transition to turbulence in these flows.

## 3.1 Introduction

A variation of viscosity in space and time occurs in a vast range of flows. Practically all flows where composition or temperature are not constant are of varying viscosity. Changes in viscosity are known to affect the stability of the flow dramatically. While an enormous literature is available on viscosity stratification and its effect on linear instability, far less is studied about how it impacts the nonmodal growth of perturbations. Understanding the transition to turbulence in shear flow requires understanding how nonmodal perturbations grow and propagate. In recent years, it has been recognised (Cherubini et al., 2010; Pringle and Kerswell, 2010; Pringle et al., 2012) that studying the nonlinear optimal perturbations is essential to this effort. The present study is the first to our knowledge on nonlinear optimal perturbations in viscosity-stratified flows. Our interest is in a gentle variation of viscosity rather than a sharp one, and we choose a pressure-driven channel flow with the walls maintained at different temperatures as a prototypical model flow to reveal the essential physics. Further, we are interested in short term optimisation, to underline how viscosity varying flows already depart considerably from constant viscosity flows. We set gravity to zero in this study to isolate the effects of viscosity variation.

The interaction of viscosity stratification and shear can lead to both suppression and enhancement of flow instabilities (for a review, see Govindarajan and Sahu (2014)). A viscosity jump across an interface can give rise to linear instability at any Reynolds number (see e.g. Yih (1967)), i.e., the flow is always unstable. On the other hand, a lowering of viscosity near a wall has been studied for decades as a means to stabilise shear flow and to thus achieve drag reduction, e.g., in lubricating oil pipelines (Preziosi

et al., 1989). Composition variation and the introduction of polymers, whence besides elasticity, viscosity variations resulting due to shear thinning can be important, have been explored over the years. In aerospace applications (Mack, 1984), a viscosity reduction near the wall in a boundary layer can provide a fuller and more stable velocity profile. By virtue of viscosity and its spatial gradients (Govindarajan, 2004; Schmid et al., 2002) being multiplied by the highest derivatives in the stability equations, we are presented with a singular perturbation problem. In other words, however high the Reynolds number (or however small the viscosity), viscosity and its variations can have a large effect on the flow. For example, Ranganathan and Govindarajan (2001) showed that a ten percent change in viscosity across a thin layer can, if overlapped with the critical layer of the least stable eigenmode, give rise to an order of magnitude change in the critical Reynolds number  $Re_c$  of 5772.22 in a channel. The effect of wall heating and subsequent viscosity changes on a fully developed turbulent flow has been studied using direct numerical simulations (DNS) for both a boundary layer (Lee et al., 2013) and a channel flow (Zonta et al., 2012). Zonta et al. (2012) find vortical structures to be more populated near the colder (more viscous) wall as compared to the hotter (less viscous) wall, while Lee et al. (2013) find that vortical structures near the heated wall are unaffected, whereas away from the wall, they become sparser with wall heating. The effects of a continuous variation of viscosity have also been investigated in the linear stability studies of Potter and Graber (1972); Sameen and Govindarajan (2007); Schäfer and Herwig (1993); Wall and Wilson (1996).

For a channel flow below  $Re_c$ , a traditional normal-mode analysis as discussed in earlier chapters predicts that there is no modal stability. However, the linear stability operator of the flow, obtained by linearising the Navier-Stokes equations about a laminar flow and posing the resulting Orr-Sommerfeld and Squire equations as an eigenvalue problem, is non-normal. This has already been described in the previous chapter where we see how shear introduces non-normality. Hence, a transient (algebraic) growth in energy can occur in the flow due to the superimposition of suitably arranged eigenmodes at intermediate time (Reddy and Henningson, 1993; Trefethen et al., 1993). If the transient growth is large enough, nonlinear mechanisms could be activated. For such flows, non-modal analysis is extremely necessary to improve our understanding of short-time behaviour (Schmid, 2007).

For any amplitude of initial perturbation, the optimal perturbation can be obtained by an adjoint-based iterative optimisation procedure called direct-adjoint looping with the full, or linearised, Navier-Stokes equations as has been described in detail in the earlier chapter. It has been applied to the Navier-Stokes equations for control of fluid flow by Abergel and Temam (1990); Bewley et al. (2000); Zuccher et al. (2004) among others, and to numerically calculate the optimal perturbations and the associated transient growth, within the framework of the linearised as well as of the nonlinear Navier-Stokes equations, as in Monokrousos et al. (2011), Foures et al. (2013), Kaminski et al. (2014), Marcotte and Caulfield (2018), Vermach and Caulfield (2018) (for a review, see Kerswell (2018)). We have also mentioned why studying the nonlinear equations is important to fully uncover the nonmodal energy growth mechanisms.

In this chapter, we investigate the sole effects of viscosity stratification on the optimal perturbation and the resultant transient growth at early times. Our central idea is to investigate how the process of subcritical perturbation energy growth in the nonlinear regime is affected by viscosity variations. We consider the full nonlinear Navier-Stokes equations, modified to account for varying viscosity, and derive the adjoint viscosity-stratified Navier Stokes equations. We then use the direct-adjoint looping described earlier to calculate the optimal perturbation for a fixed target-time. Performing studies with very small and more significant initial perturbation amplitudes, our findings show how nonlinearity is a crucial part of the initial evolution, although the Orr and lift-up mechanisms in operation have linear underpinnings. The evolution of initial perturbation which maximises linear energy growth is restricted to the hot (low viscous) wall, whereas optimising for nonlinear energy growth shows how the cold (high viscous) wall is more important, with persistent streaks and velocity profiles becoming increasingly inflectional.

## 3.2 Governing equations and problem formulation

We study pressure-driven flow through a three-dimensional channel bounded by two parallel walls, kept fixed at  $y = \pm L_y$  as depicted in figure 3.1. This figure has been reproduced from the previous chapter just for ease of description. The mean pressure gradient  $dP/dx$  forces the flow in the  $x$  direction. Hence,  $x$  is the streamwise direction and  $z$  the spanwise direction. The temperature of both walls is kept constant, with the wall

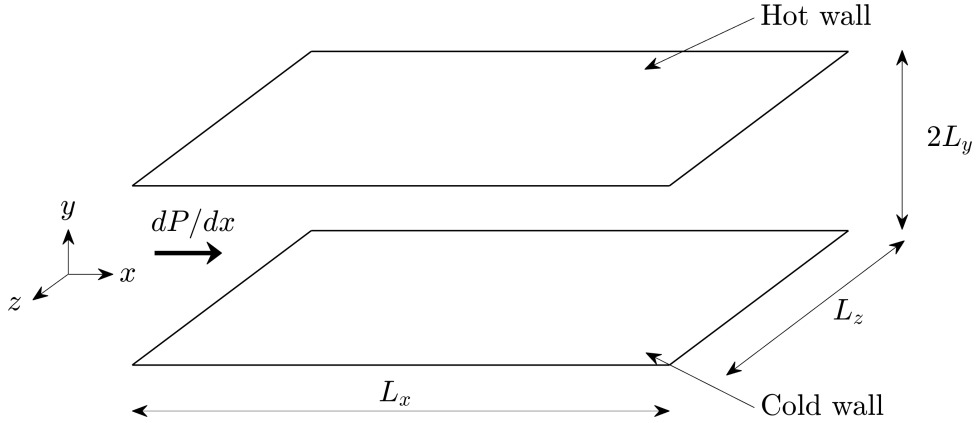


Figure 3.1: The flow domain being studied. The flow is from left to right, driven by the mean pressure gradient  $dP/dx$ .  $L_x = 2\pi L_y$  is the streamwise length,  $L_z = \pi L_y$  is the spanwise length, and  $L_y$  is the half-width of the channel. The hot and the cold walls at  $y = \pm L_y$  are kept at constant but different temperatures.

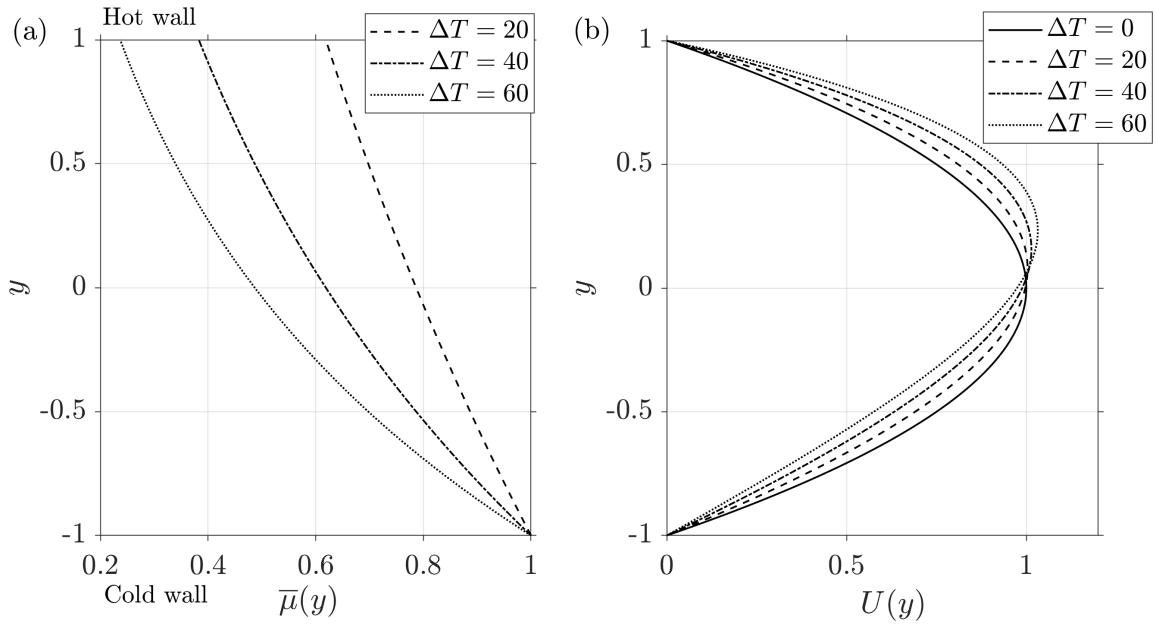


Figure 3.2: The wall-normal ( $y$ ) profiles, for various temperature differences  $\Delta T$  between the walls, of (a) base viscosity  $\bar{\mu}(y)$  as given by equation (3.5). The profile for  $\Delta T = 0$  is a vertical line at  $\mu(y) = 1$ . The ratios of viscosity between the top (hot) and the bottom (cold) wall are 0.61 for  $\Delta T = 20$  K (dashed line), 0.38 for  $\Delta T = 40$  K (dash-dotted line), and 0.23 for  $\Delta T = 60$  K (dotted line). (b) The unperturbed streamwise laminar velocity  $U(y)$ , normalised to have equal volumetric flux through the channel for unstratified case (solid line) and different  $\Delta T$ .

at  $y = L_y$  at a higher temperature than the wall at  $y = -L_y$ . There is no gravity in this problem, and non-Boussinesq effects arising from density change due to temperature variations are neglected. The half-width,  $L_y$ , of the channel is chosen as our length scale. The nondimensional size of the channel is fixed at  $2\pi, 2, \pi$  in the  $x, y$ , and  $z$  directions, respectively.

The unperturbed laminar flow through the channel is our base state. Three-dimensional perturbations are introduced over this base state. The nondimensional governing equations for a viscosity-stratified flow read as,

$$\frac{\partial u_i}{\partial x_i} = 0, \quad (3.1)$$

$$\frac{\partial u_i}{\partial t} + (U_j + u_j) \frac{\partial u_i}{\partial x_j} + u_j \frac{\partial U_i}{\partial x_j} = -\frac{\partial p}{\partial x_i} + \frac{2\beta}{Re} \frac{\partial}{\partial x_j} [\mu(s_{ij} + S_{ij}) + \bar{\mu}s_{ij}], \quad (3.2)$$

$$\frac{\partial T}{\partial t} + (U_j + u_j) \frac{\partial T}{\partial x_j} + u_j \frac{\partial (\bar{T} + T_0)}{\partial x_j} = \frac{1}{RePr} \frac{\partial^2 T}{\partial x_j^2}. \quad (3.3)$$

Here  $U_j = \delta_{j1}U(y)$  is the laminar base state, consisting only of a streamwise component,  $u_j(x, y, z, t)$  are the components of the perturbation velocity  $\mathbf{u}(\mathbf{x}, t)$  and  $p(\mathbf{x}, t)$  is the perturbation pressure.  $x, y$ , and  $z$  are referred to as  $x_1, x_2$ , and  $x_3$ , respectively. Other symbols are as defined in the previous chapter.  $T(\mathbf{x}, t)$  is the perturbation temperature, and the base state temperature  $\bar{T}(y) + T_0$  is linear in  $y$ , varying from the reference temperature  $T_0$  at the bottom wall to  $T_0 + \Delta T$  at the top wall. The base and perturbation viscosities,  $\bar{\mu}(T)$  and  $\mu(T)$  respectively, are functions of temperature alone, and are defined in section 3.2.1. The Reynolds number  $Re$  and the viscosity ratio  $\beta$  have to be defined separately in section 3.2.2 because of the introduction of viscosity stratification.  $Pr = \mu_0 c_p / \rho k$  is the Prandtl number, where  $\mu_0$  is the viscosity at the reference temperature  $T_0$ ,  $c_p$  the specific heat at constant pressure, and  $k$  the thermal conductivity of the fluid. The density  $\rho$  of the fluid is taken to be a constant.

The initial condition for perturbation velocity

$$\mathbf{u}(\mathbf{x}, 0) = \mathbf{u}_0(\mathbf{x}), \quad (3.4)$$

is usually a random noise and temperature perturbations  $T(\mathbf{x}, 0)$  are initialised to zero. Barring the mean pressure drop  $dP/dx$  which is linear, all variables of the flow are

prescribed to be periodic at the domain boundaries in  $x$  and  $z$ . No-slip velocity boundary conditions are imposed at the walls.

We will refer to equation (3.2) as the modified Navier-Stokes equation, valid for viscosity-stratified flow. The set of equations (3.1)-(3.3) are referred to as the ‘direct’ equations to distinguish them from another set of equations called the ‘adjoint’ equations. The variables in equations (3.1)-(3.3) are direct variables as in the previous chapter.

### 3.2.1 Viscosity model and the base state

The local non-dimensional viscosity  $\mu_{tot}$  in the flow is modelled as an exponential function of the total temperature  $T_{tot} = \bar{T}(y) + T_0 + T$ , following Wall and Wilson (1996), as

$$\mu_{tot} \equiv \bar{\mu} + \mu = \frac{\exp(-\kappa T_{tot})}{\exp(-\kappa T_0)}, \quad \text{where} \quad \bar{\mu} = \frac{\exp[-\kappa(\bar{T}(y) + T_0)]}{\exp(-\kappa T_0)}. \quad (3.5)$$

The viscosity of the cold wall is used as the scale here. With the constant  $\kappa$  chosen to be 0.012 per degree Kelvin, this function closely follows the viscosity of water in our temperature range. Since the density of water varies by less than 2 parts in a 1000 for the largest temperature difference, variations in kinematic viscosity are mainly from changes in dynamic viscosity. As is typical of liquids, the viscosity decreases with an increase in temperature, as shown in figure 3.2(a). The laminar base profile of the streamwise velocity given by (Wall and Wilson, 1996)

$$U(y) = \frac{-2\alpha}{\kappa\Delta T} [1 + \coth \kappa\Delta T + (y - \coth \kappa\Delta T) \exp(\kappa\Delta T(1 + y))], \quad (3.6)$$

where

$$\alpha = \frac{2\kappa\Delta T}{3} \frac{1}{-2(1 + \coth \kappa\Delta T) + (\exp(2\kappa\Delta T) - 1)/(\kappa\Delta T)^3}, \quad (3.7)$$

allows for the same non-dimensional volumetric flow rate through the channel for different temperature differences  $\Delta T$  as shown in figure 3.2(b). The nondimensional mean pressure gradient is

$$\frac{dP}{dx} = -\frac{2\alpha\beta}{Re}. \quad (3.8)$$

### 3.2.2 The Reynolds number

In order to make a fair comparison between the growth of perturbation energy in a stratified flow and an unstratified flow, a careful definition of the Reynolds number is required. As the laminar base velocity profile in a stratified channel is asymmetric about  $y = 0$  (figure 3.2(b)), the centerline velocity is not a standard velocity scale across different stratification levels, whereas the volume flux is. Secondly, the viscosity in the channel decreases continuously when moving away from the cold wall at  $y = -1$  (figure 3.2(a)). If, for example,  $Re$  was defined based only on the viscosity at the cold wall, then the effective Reynolds number of the stratified channel would be higher than this value, and consequently the perturbation energy growth could be expected to be higher. So, we choose the space-averaged mean viscosity as our viscosity scale to define  $Re$ . The Reynolds number used in this chapter is

$$Re \equiv \rho L_y \frac{\int_{-L_y}^{L_y} 1.5U(y)dy}{\int_{-L_y}^{L_y} \bar{\mu}_d dy} = \frac{1.5\rho L_y \langle U \rangle}{\langle \bar{\mu}_d \rangle}, \quad (3.9)$$

where  $\bar{\mu}_d(T)$  is the dimensional base viscosity of the fluid, and the angle brackets represent an average in the wall normal direction  $y$ . A factor of 1.5 is incorporated for ease of comparison with earlier studies on unstratified flow which use the centerline velocity as the velocity scale. The dimensional viscosity must therefore be scaled by the average viscosity in the channel, but for ease of comparison, we have scaled it by its value at the cold wall. This is adjusted for, by the introduction in equations (3.2) and (3.8) of the viscosity ratio

$$\beta = \frac{\bar{\mu}_d(T_0)}{\langle \bar{\mu}_d \rangle}. \quad (3.10)$$

In this chapter, we remain in the subcritical regime by fixing  $Re$  at 500.

### 3.2.3 Direct-adjoint looping

To formulate the direct-adjoint looping for this viscosity-stratified case, we need to define a cost functional which includes some measure of energy, and the aim of the optimisation procedure would be to maximise this cost functional. Especially when density or viscosity

or any flow component varies with space and time, there are many choices that may be made for the cost functional, and each choice could lead to a different optimal perturbation. For example, Foures et al. (2014) show interestingly that energy optimization leads to weak mixing, but optimal perturbations obtained from mixing optimization are very effective in mixing, though evolving to lower energies. Thus, the aims of each study are critical in choosing an appropriate cost functional.

In this first attempt to understand the optimal perturbations in a viscosity-stratified channel flow, we study the growth of kinetic energy of the velocity perturbations. The cost functional is same as the prototypical one that we considered in the previous chapter when elaborating on the optimisation technique. As noted in previous studies (Foures et al., 2014; Vermach and Caulfield, 2018) perturbations growing through a given time horizon may not have largest energy precisely at a target time. To account for this, we choose the ratio of the integral over time, up to a preset target-time, of the perturbation kinetic energy, to the initial perturbation kinetic energy, as our cost functional. The time-integrated perturbation kinetic energy of the flow is defined as

$$G(\mathcal{T}) = \frac{\gamma}{2} \int_0^{\mathcal{T}} \|\mathbf{u}(\mathbf{x}, t)\|_{\mathcal{V}}^2 dt, \quad (3.11)$$

where  $\|\mathbf{u}(\mathbf{x}, t)\|_{\mathcal{V}}$  is the total (integrated over the channel volume  $\mathcal{V}$ )  $l^2$ -norm of the velocity perturbations  $\mathbf{u}(\mathbf{x}, t)$ . Note that the math-calligraphy symbol  $\mathcal{T}$  for the target-time is distinguished from the italics  $T$  for temperature.  $\gamma$  is a constant with units of inverse time, and has been set to unity throughout this study.  $\mathcal{T}$  is non-dimensionalised with the advective time scale, i.e.,  $L_y/1.5\langle U \rangle$ , a constant across the various stratification levels studied here. Time-integration includes effects from the intermediate-time dynamics of the flow as opposed to just the energy at the target-time  $\mathcal{T}$ . The total initial perturbation kinetic energy is same as that defined earlier

$$E_0 = \frac{1}{2} \|\mathbf{u}_0(\mathbf{x})\|_{\mathcal{V}}^2. \quad (3.12)$$

The cost functional  $\mathcal{J}(\mathcal{T})$  of our interest is

$$\mathcal{J}(\mathcal{T}) = \frac{G(\mathcal{T})}{E_0}. \quad (3.13)$$

Our aim is to find the optimal perturbation  $\mathbf{u}_0(\mathbf{x}, 0)_{opt}$  to get

$$\mathcal{J}_{opt}(\mathcal{T}) \equiv \mathcal{J}_{max}(\mathcal{T}) = \frac{G_{opt}(\mathcal{T})}{E_0}, \quad (3.14)$$

with a fixed initial energy  $E_0$ .

Following the methodology in the earlier chapter, we define the Lagrangian  $\mathcal{L}$  which is the cost functional  $\mathcal{J}(t)$  in equation (3.13), constrained by the incompressibility condition (3.1), the modified viscosity-stratified Navier-Stokes equations (3.2), the temperature equation (3.3), and the initial velocity conditions of the flow (3.4). The constrained Lagrangian  $\mathcal{L}$  is

$$\begin{aligned} \mathcal{L} = \mathcal{J}(\mathcal{T}) - & \left[ \frac{\partial u_i}{\partial t} + (U_j + u_j) \frac{\partial u_i}{\partial x_j} + u_j \frac{\partial U_i}{\partial x_j} + \frac{\partial p}{\partial x_i} - \frac{2\beta}{Re} \frac{\partial}{\partial x_j} (\mu(s_{ij} + S_{ij}) + \bar{\mu}s_{ij}), v_i \right] - \left[ \frac{\partial T}{\partial t} \right. \\ & \left. + (U_j + u_j) \frac{\partial T}{\partial x_j} + u_j \frac{\partial (\bar{T} + T_0)}{\partial x_j} - \frac{1}{RePr} \frac{\partial^2 T}{\partial x_j^2}, \tau \right] - \left[ \frac{\partial u_i}{\partial x_i}, q \right] - \langle \langle u_i(0) - u_{0,i}, v_{0,i} \rangle \rangle, \end{aligned} \quad (3.15)$$

where parenthesis have already been defined.  $u_i(0) = u_{0,i}$  are the components of the initial perturbation velocity  $\mathbf{u}_0(\mathbf{x})$ .  $v_i$ ,  $q$ ,  $\tau$ , and  $v_{0,i}$  are the already familiar adjoint velocity, adjoint pressure, adjoint temperature, and adjoint velocity initial condition corresponding to direct variables  $u_i$ ,  $p$ ,  $T$ , and  $u_{0,i}$ .

$$\frac{\partial v_i}{\partial x_i} = 0, \quad (3.16)$$

$$\begin{aligned} \frac{\partial v_i}{\partial t} - v_j \frac{\partial (u_j + U_j)}{\partial x_i} + \frac{\partial (v_i(U_j + u_j))}{\partial x_j} + \frac{\beta}{Re} \frac{\partial}{\partial x_j} \left[ (\mu + \bar{\mu}) \left( \frac{\partial v_i}{\partial x_j} \right. \right. \\ \left. \left. + \frac{\partial v_j}{\partial x_i} \right) \right] - \tau \frac{\partial (T + \bar{T} + T_0)}{\partial x_i} + \frac{\partial q}{\partial x_i} + \gamma u_i = 0, \end{aligned} \quad (3.17)$$

$$\frac{\partial \tau}{\partial t} + (U_j + u_j) \frac{\partial \tau}{\partial x_j} + \frac{1}{RePr} \frac{\partial^2 \tau}{\partial x_j^2} - \frac{2\beta}{Re} \left[ \frac{\partial \mu}{\partial T} (s_{ij} + S_{ij}) + \frac{\partial \bar{\mu}}{\partial T} s_{ij} \right] \frac{\partial v_i}{\partial x_j} = 0, \quad (3.18)$$

$$v_i(\mathcal{T}) = 0, \quad \tau(\mathcal{T}) = 0. \quad (3.19)$$

Equations (3.16)-(3.18) are the adjoint equations corresponding to the direct equations (3.1)-(3.3). For a constant viscosity flow, these adjoint equations reduce to those derived by Vermach and Caulfield (2018) for mixing of a passive scalar and also noted in the previous chapter.  $v_i$  and  $q$  have the same dimensions as the direct variables  $u_i$  and  $p$ . But  $\tau$  behaves as the square of a velocity per unit temperature. Nevertheless, we refer to it as adjoint temperature since its evolution equation (3.18) is derived by taking a variation of  $\mathcal{L}$  in equation (3.15) with respect to  $T$ . We notice that in the absence of viscosity stratification, the last term in equation (3.18) with the coefficient of  $2\beta/Re$ ,

vanishes, and since we have no gravity, the solution to equation (3.18) is just  $\tau = 0$ . The temperature term will then drop out of the adjoint momentum equation (3.17). The sign of the diffusion of adjoint momentum and temperature in equations (3.17) and (3.18) imply that only during backward time evolution, i.e., from  $t = \mathcal{T}$  to 0, these equations are well posed as has been mentioned already. We use the rotation technique to constrain the  $E_0$  of the updated perturbations on a fixed energy hypersphere. The adjoint equations for a viscosity-stratified flow are derived here for the first time to our knowledge. We see new terms involving gradients in viscosity, both of the mean and of the perturbations, entering the adjoint velocity as well as the adjoint temperature equations.

The target-time of optimisation is fixed at  $\mathcal{T} = 4$  and we study the linear and nonlinear optimal perturbations and the mechanism behind their evolution, for an unstratified flow, and for stratified flows with temperature differences between the upper and the lower channel walls at  $\Delta T = 20$  K, 40 K, and 60 K. Kaminski et al. (2017) studied the non-linear evolution of the linear optimal perturbations in a density-stratified flow and found the linear optimal perturbations to be sufficient to trigger non-linear effects when evolved with sufficiently large  $E_0$ . However, as we will show later for viscosity-stratified flows, the linear optimal perturbation is qualitatively different in structure from the non-linear optimal perturbation, and hence leads to qualitative and quantitative differences even when scaled to have large  $E_0$ . For unstratified flow despite the clear structural differences in the linear and non-linear optimal perturbations, we find similar qualitative and quantitative evolution of the two, when initialised at  $E_0 = 10^{-2}$ . Thus, the non-linear  $\mathcal{O}(u_i v_j)$ ,  $\mathcal{O}(u_i \tau)$  terms in the adjoint equations (3.17) and (3.18) are critical, especially for the viscosity-stratified flow. We also remark briefly upon the effect of Prandtl number on the evolution of the non-linear optimal perturbation.

Inclusion of viscosity stratification creates an asymmetric velocity profile and we obtain that from our solver and we match with Wall and Wilson (1996) as in figure 3.3. The figure also acts as a validation of the viscosity stratified terms in our solver.

For the viscosity-stratified case we ran the direct-adjoint loop at very low initial energy of  $E_0 = 10^{-8}$  to get the linear optimal perturbation by maximising  $E(\mathcal{T})$ , compared it to the linear viscosity-stratified optimal perturbation obtained from SVD, and obtained excellent agreement.

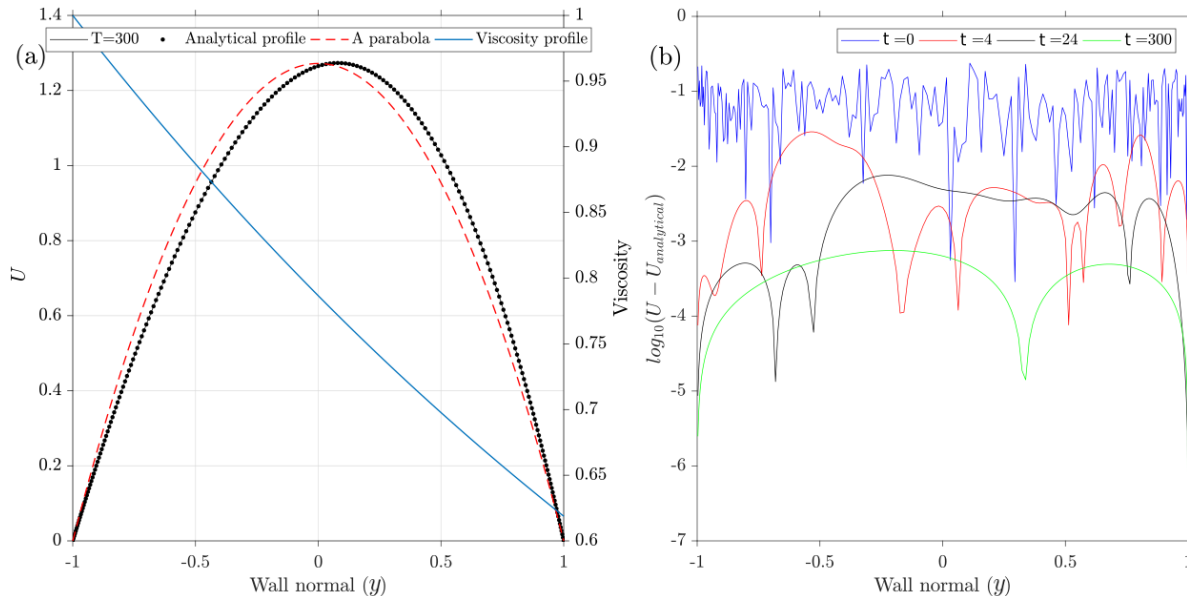


Figure 3.3: (a) Streamwise velocity profile from the solver (black line) compared with the viscosity stratified analytical profile (black dots (Wall and Wilson, 1996)) with  $\Delta T = 20^\circ\text{K}$ . A parabola is plotted (red dotted) to show that the streamwise velocity profile is skewed. Plotted in blue is the viscosity profile. (b) The error in the streamwise velocity between the solver output and the analytical profile for a viscosity stratified case. With time ( $t$ ), the error decreases.

### 3.3 Evolution of stratified optimal perturbations

#### 3.3.1 The linear optimal and its evolution

When the direct-adjoint looping is employed at  $E_0 = 10^{-8}$ , the optimal perturbation obtained by direct-adjoint looping, and its early time evolution, remain linear. This was remarked upon by Foures et al. (2013), and we checked this for stratified flows as well, as will be discussed. By increasing  $E_0$ , we may attain optimal perturbations which are increasingly nonlinear. We will see below how nonlinear optimal perturbations are very different from the linear, and how this impacts the evolution in a significant manner.

The optimal perturbations are visualised in this chapter as isosurfaces of maximum and minimum streamwise velocity perturbations  $u_1$ , e.g. as in figure 3.4 shown for linear optimal perturbations. In this figure and those to follow, a yellow isosurface is plotted at a certain percentage of the maximum over the channel of that quantity at that time, while a blue isosurface indicates regions where the quantity is at the same percentage of

the minimum (usually a negative quantity).

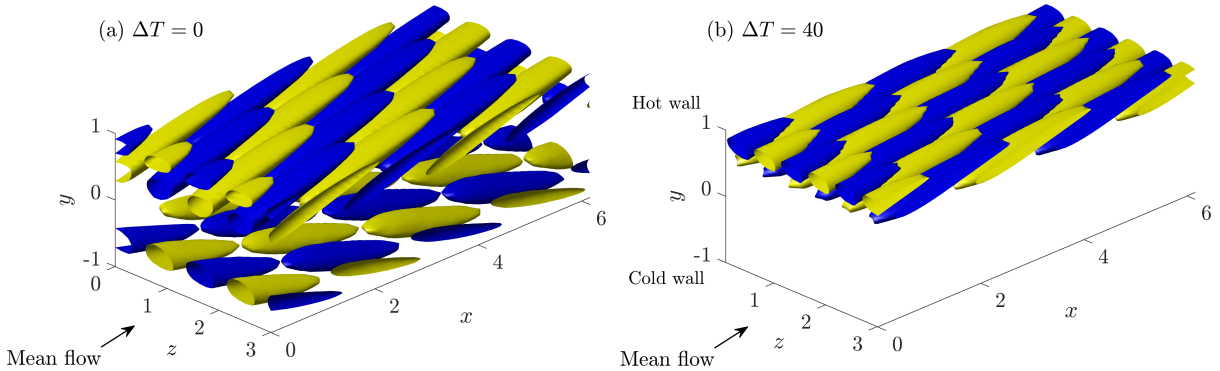


Figure 3.4: Three dimensional linear optimal perturbation ( $E_0 = 10^{-8}$ ), which maximises the cost functional in equation (3.13) for (a) unstratified ( $\Delta T = 0$ ) and (b) stratified ( $\Delta T = 40$  K) channel flow for  $Re = 500$ ,  $\mathcal{T} = 4$ , and  $Pr = 7$ . The mean flow is along the positive  $x$  as marked by arrows in (a) and (b). The colours are the 40% isosurfaces of the maximum (yellow) and minimum (blue) values of the streamwise perturbations  $u_1$ . The isosurfaces for other stratification levels ( $\Delta T = 20$  K and 60 K) are qualitatively similar to (b), with 40% isosurfaces of  $u_1$  localised near the hot wall, where viscosity is lower.

The linear optimal perturbation ( $E_0 = 10^{-8}$ ) consists of an array of streamwise velocity perturbations inclined against the mean flow and shear, on both sides of the channel for the unstratified case (figure 3.4(a)). In the stratified case, similar structures are seen, but all perturbations are remarkably localised close to the hot wall, where viscosity decreases towards the wall, with practically no action on the cold wall (figure 3.4(b)). Such localisation of linear optimal perturbations was also found by Jose et al. (2020) using SVD studies on a channel with viscosity-stratification and weak gravity. For our chosen target-time of  $\mathcal{T} = 4$ , we find that the nonmodal energy growth and the shapes of the optimal perturbations are similar whether we optimise for a cost functional with energy growth at the target-time or with time-integrated energy as in equation (3.13). As mentioned, the linear optimal perturbation for maximising energy at a target-time can also be obtained by an SVD of the respective Orr-Sommerfeld and Squire operators for the unstratified (Schmid et al., 2002) and viscosity-stratified (Chikkadi et al., 2005) cases. The streamwise and spanwise wavenumbers of the linear optimal perturbation from SVD for  $\mathcal{T} = 4$  and  $Re = 500$  are  $k_x \approx 2$  and  $k_z \approx 4$ , respectively, for an unstratified channel and  $k_x \approx 2$  and  $k_z \approx 5$ , respectively, for the viscosity-stratified channel with  $\Delta T = 40$  K. Quantized for channel length, we observe from figure 3.4 that these wavenumbers can

be seen in the linear optimal perturbations obtained from direct-adjoint looping. Besides revealing the localisation of the arrays of vortices near the hot wall due to viscosity stratification, this result is also a validation for our direct-adjoint looping.

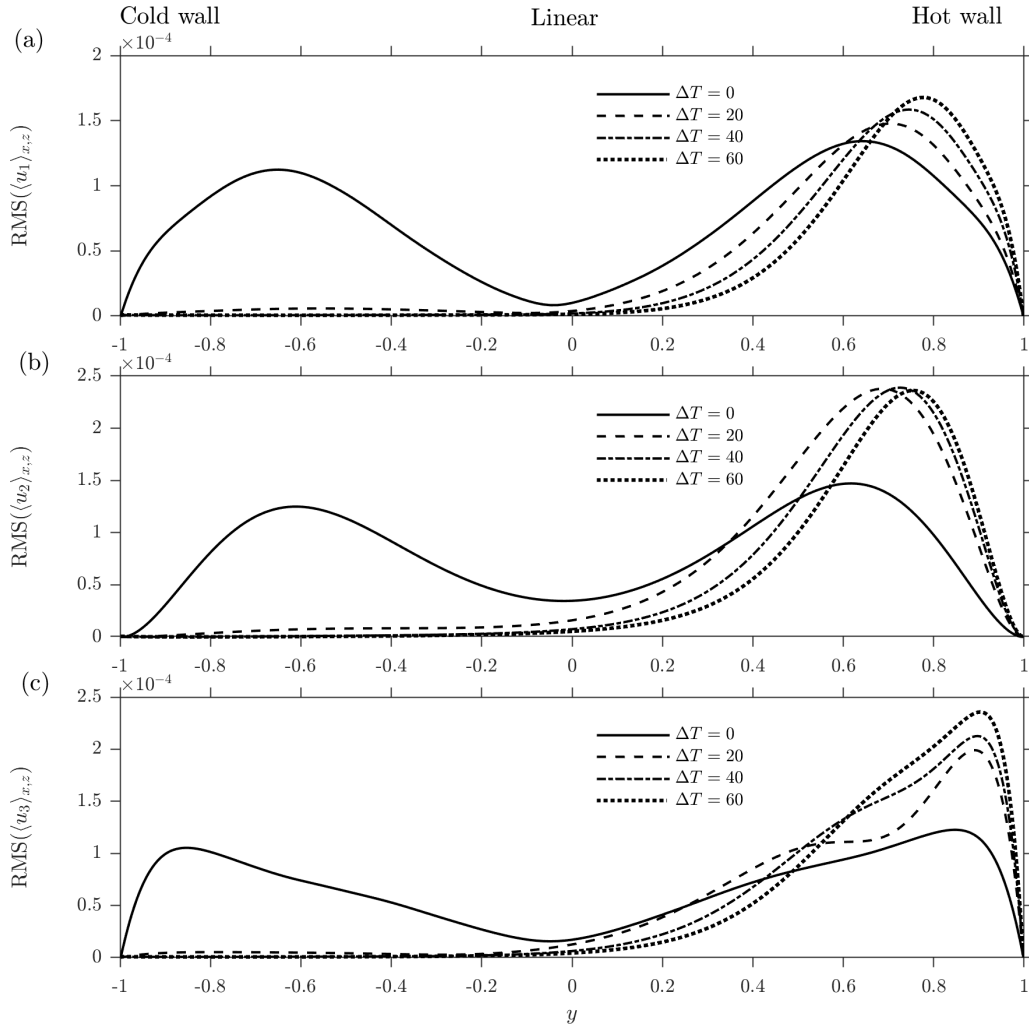


Figure 3.5: Wall normal profiles of root mean square (r.m.s., spatially averaged in the  $x$  and  $z$  directions) of the linear optimal perturbations ( $E_0 = 10^{-8}$ ). (a) Streamwise velocity perturbations  $u_1$ , (b) wall-normal velocity perturbations  $u_2$ , and (c) spanwise velocity perturbations  $u_3$  for various wall-temperature differences  $\Delta T$  (in K). The solid and the dash-dotted line in (a) correspond to the isosurfaces shown in figure 3.4(a) and (b), respectively.

The corresponding root mean square (r.m.s.) profiles of velocity perturbations of the linear optimal perturbations are shown in figure 3.5, where the quantities have been averaged in the streamwise and spanwise directions. There is a significant proportion of initial amplitude in each velocity component, and increase in  $\Delta T$  increases the proportion

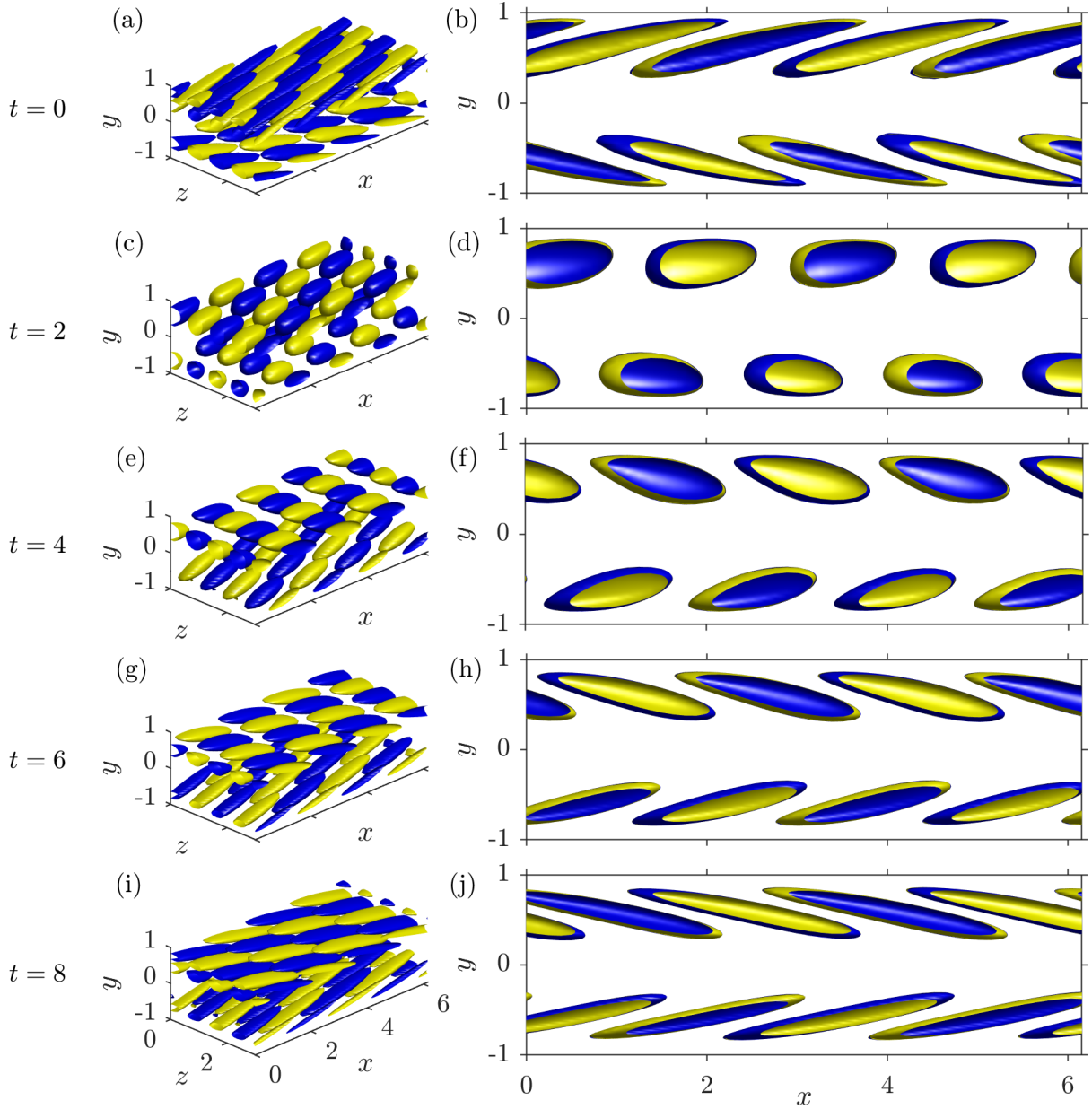


Figure 3.6: Evolution of the linear unstratified optimal perturbation shown at two angles, at times (a,b)  $t = 0$ , (c,d)  $t = 2$ , (e,f)  $t = \mathcal{T} = 4$ , (g,h)  $t = 6$ , and (i,j)  $t = 8$ . The structures are initially aligned against the shear, and as time progresses, realign along the shear.

of energy in the spanwise and wall-normal perturbations  $u_3$  and  $u_2$ . The localisation of all perturbations on the hot side of the channel is underlined in this figure.

The time evolution, obtained by solving the direct equations initialised with the linear optimal perturbation, suggests the reason for its shape. For both the unstratified and stratified cases, shown in figures 3.6 and 3.7 respectively, velocity perturbations are initially tilted against the mean shear, and as time progresses, lean into the shear as

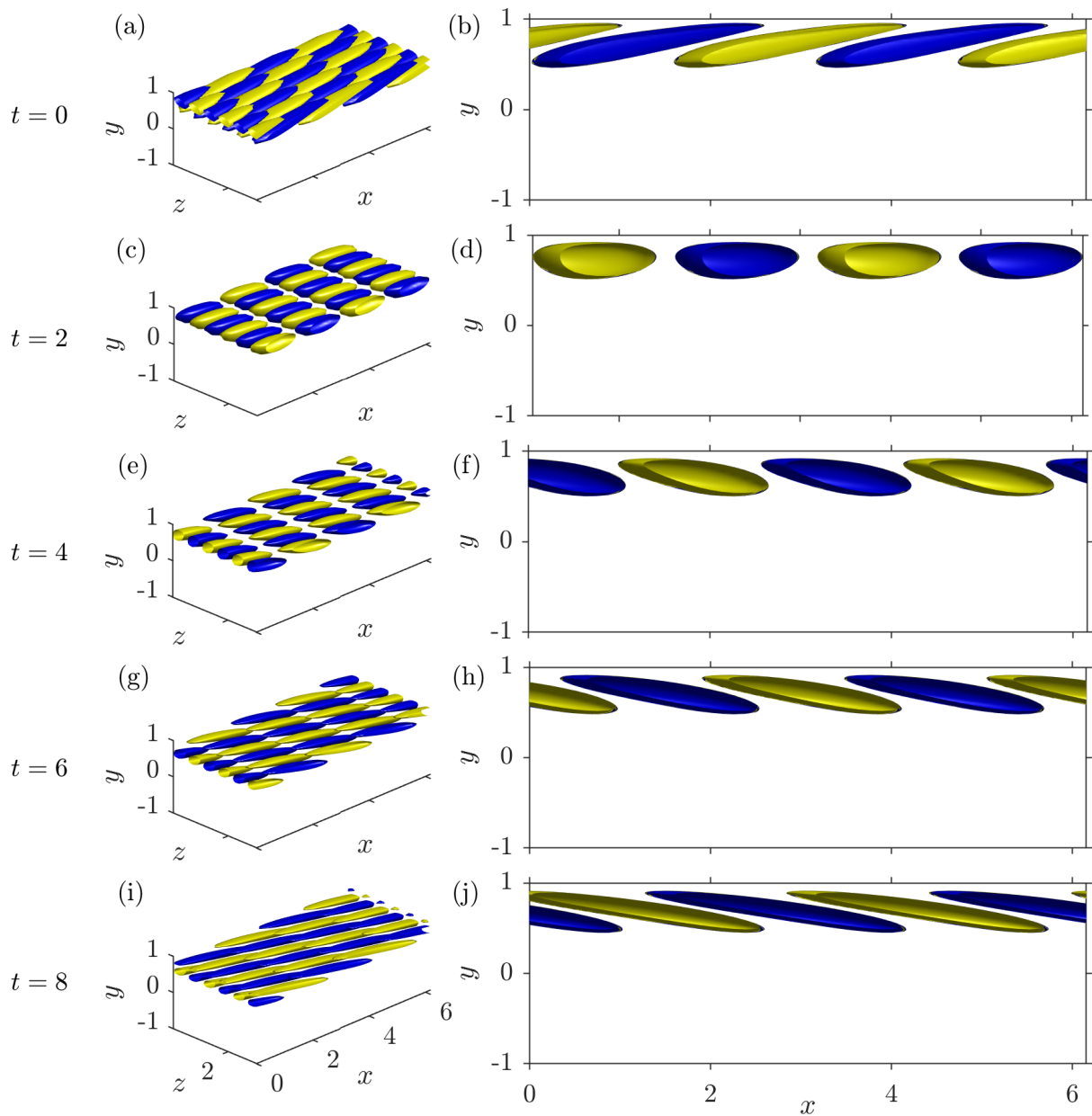


Figure 3.7: Evolution of the linear viscosity-stratified optimal perturbation ( $\Delta T = 40$  K) shown at two angles. Optimal perturbations are strongly localised on the top (hot) wall unlike in figure 3.6, and the Orr mechanism is in evidence. The times are as in figure 3.6.

they stretch. This is the well known, and probably oldest to be described, linear growth mechanism, the Orr mechanism (Orr, 1907), where the tilting and the subsequent energy growth is driven by the base, or laminar, shear. In stratified laminar flow, the magnitude of shear is larger near the less viscous wall, which for liquids is the hot wall (figure 3.2(b)). So, the Orr mechanism is much more efficient near the hot wall. It follows that for a given  $E_0$ , better growth can be achieved by placing perturbations in the high gradient region, which explains the localisation of the initial velocity perturbations in stratified

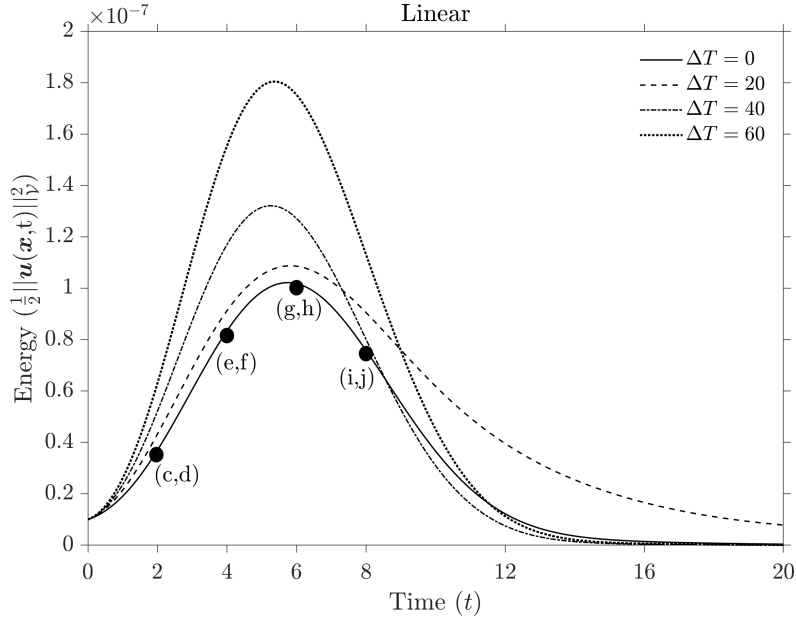


Figure 3.8: Energy growth with time of the linear optimal perturbations ( $E_0 = 10^{-8}$ ) for various stratification strengths. The labels at  $t = 2, 4, 6, 8$  on the solid line correspond to labels in figure 3.6.

flow (figure 3.4(b) and 3.5). The evolution of the optimal perturbations result in algebraic energy growth of disturbances for short duration of time which eventually decays as shown in figure 3.8. For the linear optimal perturbations, the energy growth for stratified flow is larger than for unstratified flow, but this conclusion will not be the same for the nonlinear optimal perturbations, as we shall see.

We thus find that the Orr mechanism is the dominant linear growth mechanism for small energy levels in this short target-time window. The other well-known linear growth mechanism, the lift-up mechanism (Brandt, 2014), is not observed in the evolution of linear optimal perturbation at small  $E_0$ . Before we study nonlinear optimal perturbations, it is instructive to study what would happen if the linear optimal perturbation was in large enough amplitude to trigger nonlinearities. To this end, we rescale the energy of the linear optimal perturbations to a higher initial energy,  $E_0 = 10^{-2}$ , while maintaining the shape of the initial conditions corresponding to the case shown in figure 3.4(b) for  $\Delta T = 40$  K. The evolution of the streamwise velocity perturbations for this case is shown in figure 3.9. The low momentum fluid is transferred away from the walls, displaying features of the classical lift-up mechanism (Brandt, 2014) driven by streamwise vortices (not shown). Comparing figures 3.7 and 3.9 we see that the nonlinear evolution of the linear optimal

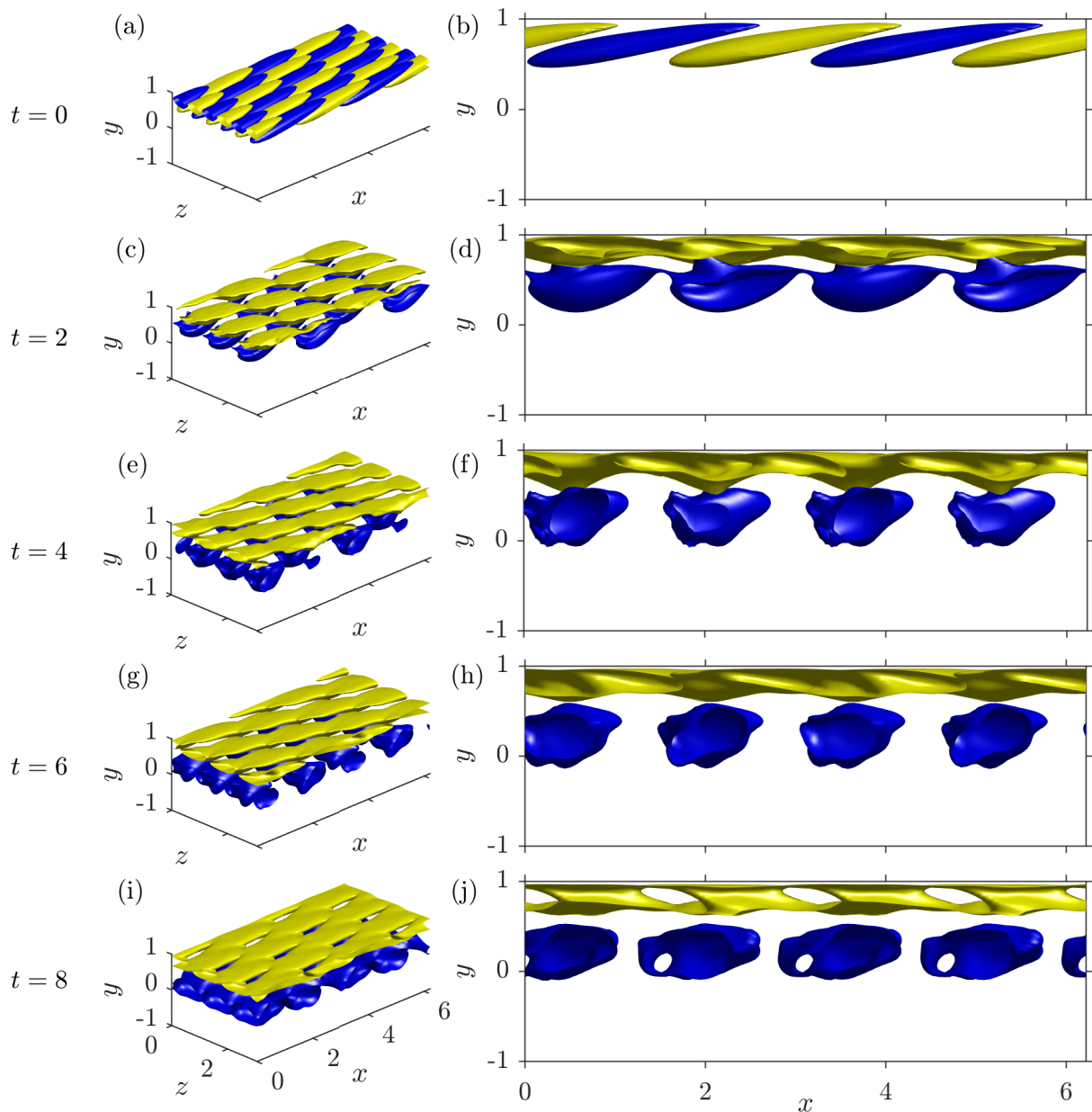


Figure 3.9: Evolution of the linear viscosity-stratified optimal perturbation ( $\Delta T = 40$  K) scaled to nonlinear initial energy  $E_0 = 10^{-2}$ , shown at two angles. The lift-up mechanism is in evidence. The times are as in figure 3.6.

perturbation is very different from the linear evolution of the linear optimal perturbation. The non-linear evolution of the linear optimal perturbation for the unstratified case (not shown) also shows a lift-up type mechanism in operation, albeit at both walls, and is symmetric about  $y = 0$ . The physical mechanism for energy growth at small energy levels ( $E_0 = 10^{-8}$ ) is thus the Orr mechanism and that at high energy levels ( $E_0 = 10^{-2}$ ) is indicative of the lift-up mechanism. As we discuss below, in particular for stratified flow, the linear optimal perturbations are not the most efficient way to extract energy

from the mean flow into the perturbations for higher energy levels.

### 3.3.2 The non-linear optimal perturbation and its evolution

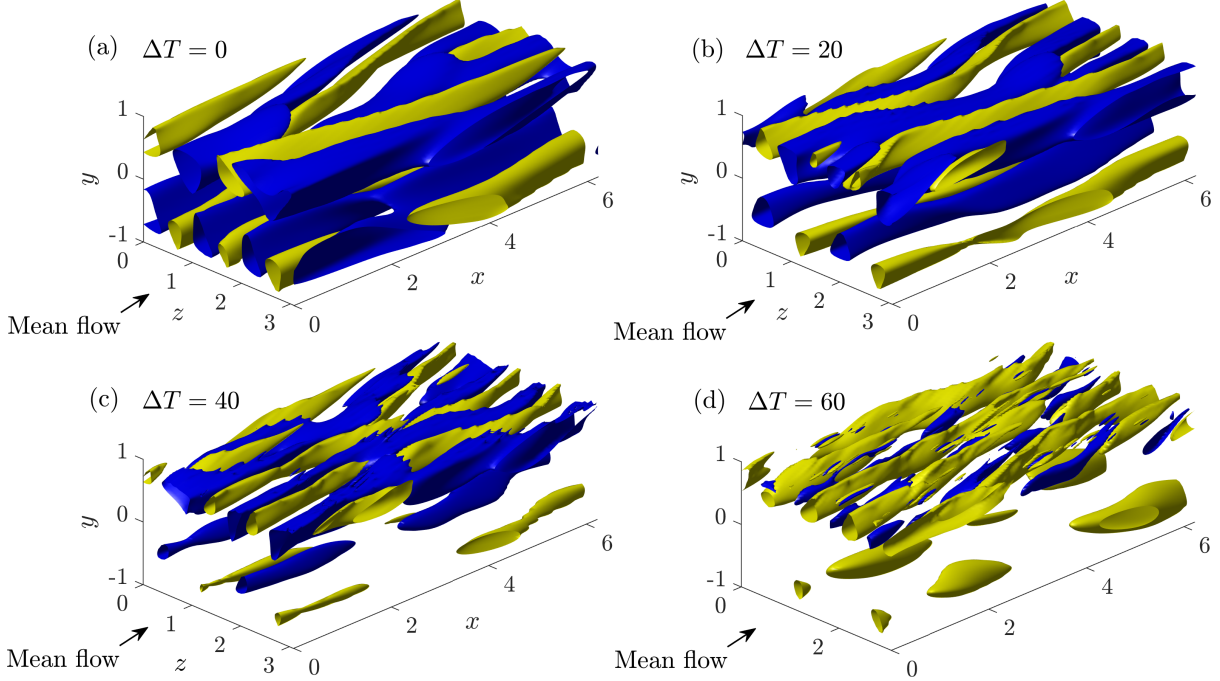


Figure 3.10: 40% isosurfaces of the maximum (yellow) and minimum (blue) values of the streamwise perturbations  $u_1$  of the nonlinear optimal perturbation ( $E_0 = 10^{-2}$ ) with (a)  $\Delta T = 0$  (unstratified); and of the viscosity-stratified nonlinear optimal perturbation with (b)  $\Delta T = 20$  K and (c)  $\Delta T = 40$  K. (d) 20% isosurfaces of the maximum (yellow) and minimum (blue)  $u_1$  for the viscosity-stratified nonlinear optimal perturbation with  $\Delta T = 60$  K. A slightly lower isosurface value had to be shown in (d) for better visualisation.

The perturbation leading to the maximum energy growth for the highest  $E_0$  of  $10^{-2}$  considered here, is referred to as the nonlinear optimal perturbation. Isosurfaces of the nonlinear optimal streamwise velocity perturbation (figure 3.10) and streamwise-spanwise averaged r.m.s. wall-normal nonlinear optimal velocity profiles (figure 3.11) show some localisation towards the hot wall due to viscosity stratification. But remarkably, unlike in the linear case (figures 3.4 and 3.5), there is significant perturbation energy on both walls of the channel for the stratified nonlinear optimal perturbation. Figure 3.11, in stark contrast to figure 3.5, makes it clear that the asymmetry between the two sides of the channel is small for the nonlinear optimal perturbation, whereas in the linear optimal perturbation, energetic structures were absent in the bottom half of the channel.

But in the nonlinear optimal perturbation too, the asymmetry increases with increasing stratification, with more structures at the hot wall. The streamwise velocity perturbations are now arranged in a series of elongated (mainly in the flow direction, but with a spanwise inclination) high and low momentum zones near the walls. Increasing the stratification level makes the population near the cold wall smaller (but not insignificant). From figure 3.11 we observe a significant contribution to the initial perturbation kinetic energy from all three components of velocity.

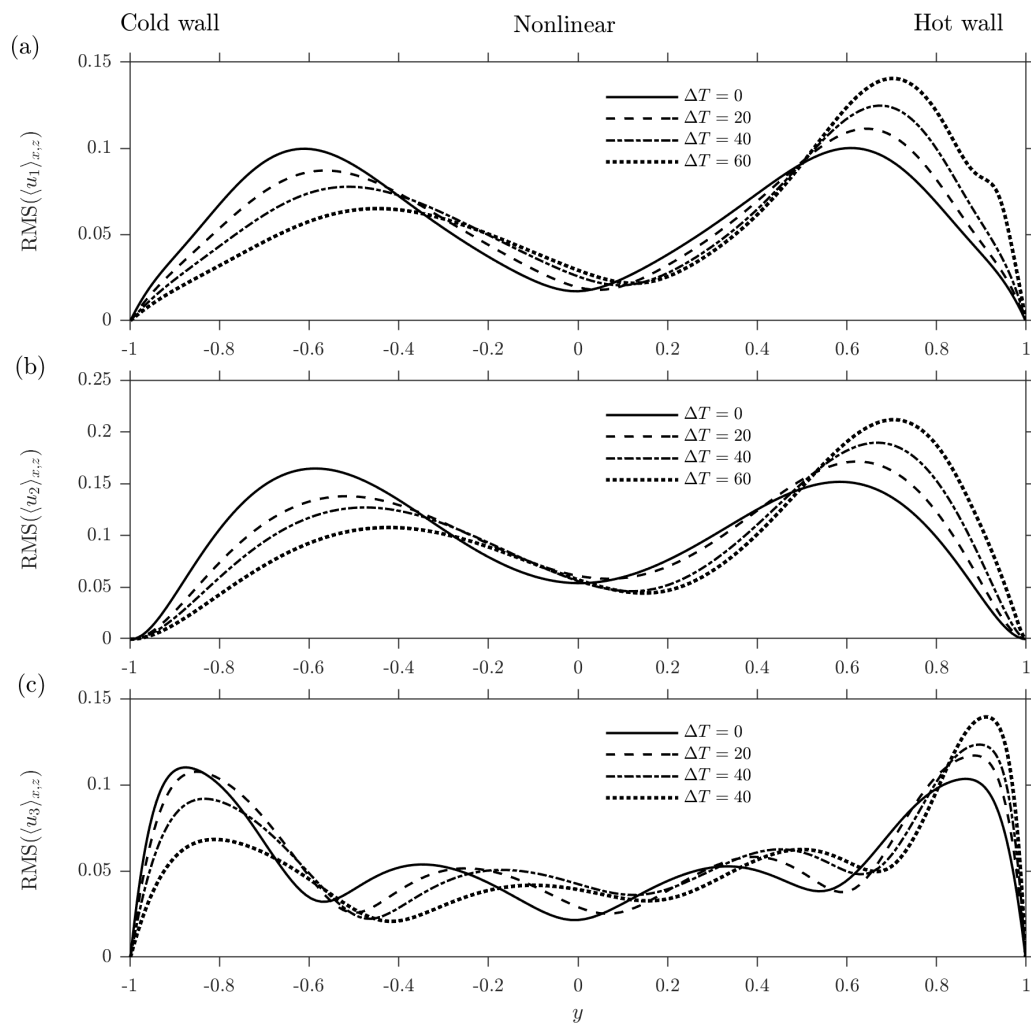


Figure 3.11: Wall normal profiles of (a) streamwise velocity fluctuations  $u_1$ , (b) wall-normal velocity fluctuations  $u_2$ , and (c) spanwise velocity fluctuations  $u_3$ , averaged across the  $x$  and  $z$  coordinates, of the nonlinear optimal perturbations ( $E_0 = 10^{-2}$ ) for various stratification strengths.

The energy-time graphs corresponding to the evolution of the nonlinear optimal perturbations in figures 3.10 and 3.11 are shown in figure 3.12 for various stratification levels.

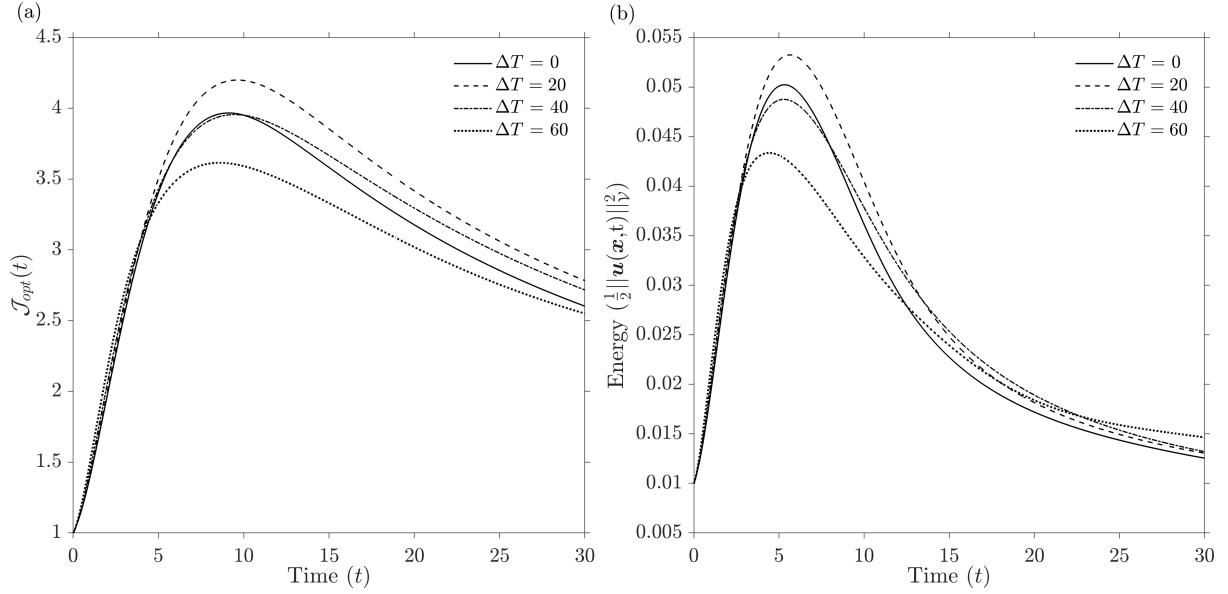


Figure 3.12: Time evolution of (a) the cost functional  $\mathcal{J}_{opt}(\mathcal{T})$  as in equation (3.14) and of (b) energy, of the nonlinear optimal perturbations for various stratification strengths. The time of optimisation is  $\mathcal{T}=4$  for all.

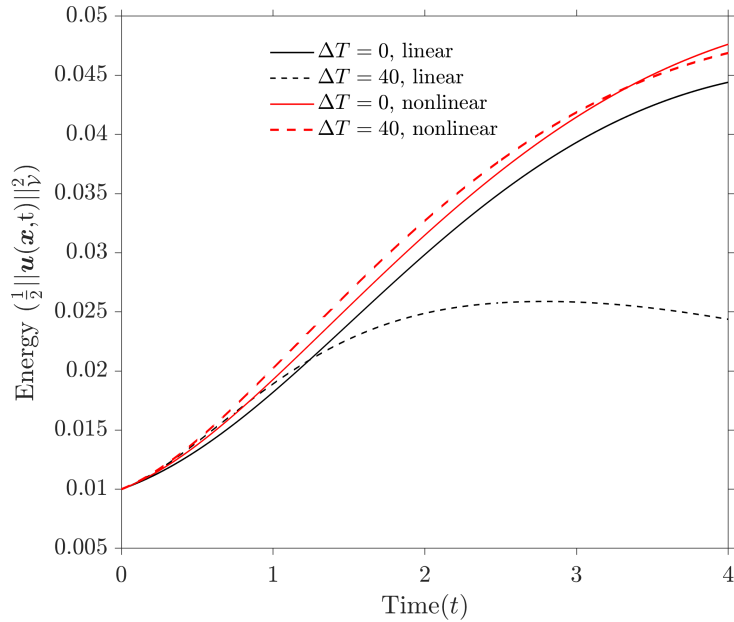


Figure 3.13: Evolution of energy of the linear (black lines) and nonlinear (red lines) optimal perturbations when evolved with the modified Navier-Stokes equation with  $E_0 = 10^{-2}$ . Solid lines are for the unstratified cases ( $\Delta T = 0$ ) while the dotted lines are for stratified cases with  $\Delta T = 40$  K. Other stratification levels (not shown), show similar behaviour to  $\Delta T = 40$  K.

Figure 3.12(a) shows the cost functional  $\mathcal{J}_{opt}(\mathcal{T})$  of the optimal perturbation which is the quantity that we optimised for, while figure 3.12(b) shows the volume-averaged kinetic energy as a function of time. Growth is algebraic in the nonlinear regime as well, and perturbations decay soon after the target-time of optimisation. Unlike in the linear evolution of the linear optimal perturbation, there is no qualitative difference between the growth in the unstratified case and those at various levels of stratification. We are now in a position to compare the evolution, by the modified Navier-Stokes equations, of the linear and the nonlinear optimal perturbations, both starting from the same initial energy of  $E_0 = 10^{-2}$ , in figure 3.13. We may first satisfy ourselves of the higher energy growth in the evolution of the non-linear optimal perturbation as compared to the linear optimal perturbation, consistent with the definition of the nonlinear optimal perturbation. For the unstratified flow, for a short target-time, it turns out that the linear and nonlinear optimal perturbations show similar growth, though the linear is of course lower, whereas the linear optimal perturbation shows a much lower growth in the stratified flow than the nonlinear optimal perturbation (comparing the dashed black line to the dashed red one in figure 3.13). This is consistent with the cold wall becoming more prominent in the evolution of the nonlinear optimal perturbation, as we shall discuss below. It is also worth mentioning that on comparison with figure 3.8 we see that the growth of energy of the linear optimal perturbation, as a ratio of the initial energy, is significantly lower with nonlinear evolution, for initial conditions differing only in amplitude. However, the absolute value of perturbation energy always remains larger than the linear case since the initial perturbation was large. When the initial perturbation is large, the available energy from the laminar flow becomes a limiting factor, which could result in the lower growth, as a ratio.

We now discuss how viscosity stratification changes the mechanism of subcritical disturbance growth and how nonlinear optimal perturbations are fundamentally different from linear optimal perturbations in this regard. Initially proposed by Hamilton et al. (1995) and Waleffe (1997) and summarised by Brandt (2014), the regeneration/self-sustaining cycle of wall turbulence involves three steps, (i) lift-up, i.e., transportation of low (high) momentum fluid away from (towards) the wall by streamwise vortices, to form streamwise independent streaks of low (high) momentum away from (near) the wall, (ii) break down of these by inflectional secondary instability to acquire streamwise de-

pendence and (iii) regeneration of elongated vortices by nonlinear interactions between oblique modes. These arguments were initially made with the linear optimal perturbation in mind. Through similar direct-adjoint looping methodology, Cherubini et al. (2011) for a boundary layer and Cherubini and De Palma (2013) for a Couette flow showed that it is much more efficient for the lift-up to be driven by streamwise modulated vortices in the first place. The nonlinear optimal perturbation inherently contains such streamwise modulation. This is referred to as the modified lift-up mechanism, as it can bypass the stage of secondary (streak) instability en-route to transition to turbulence.

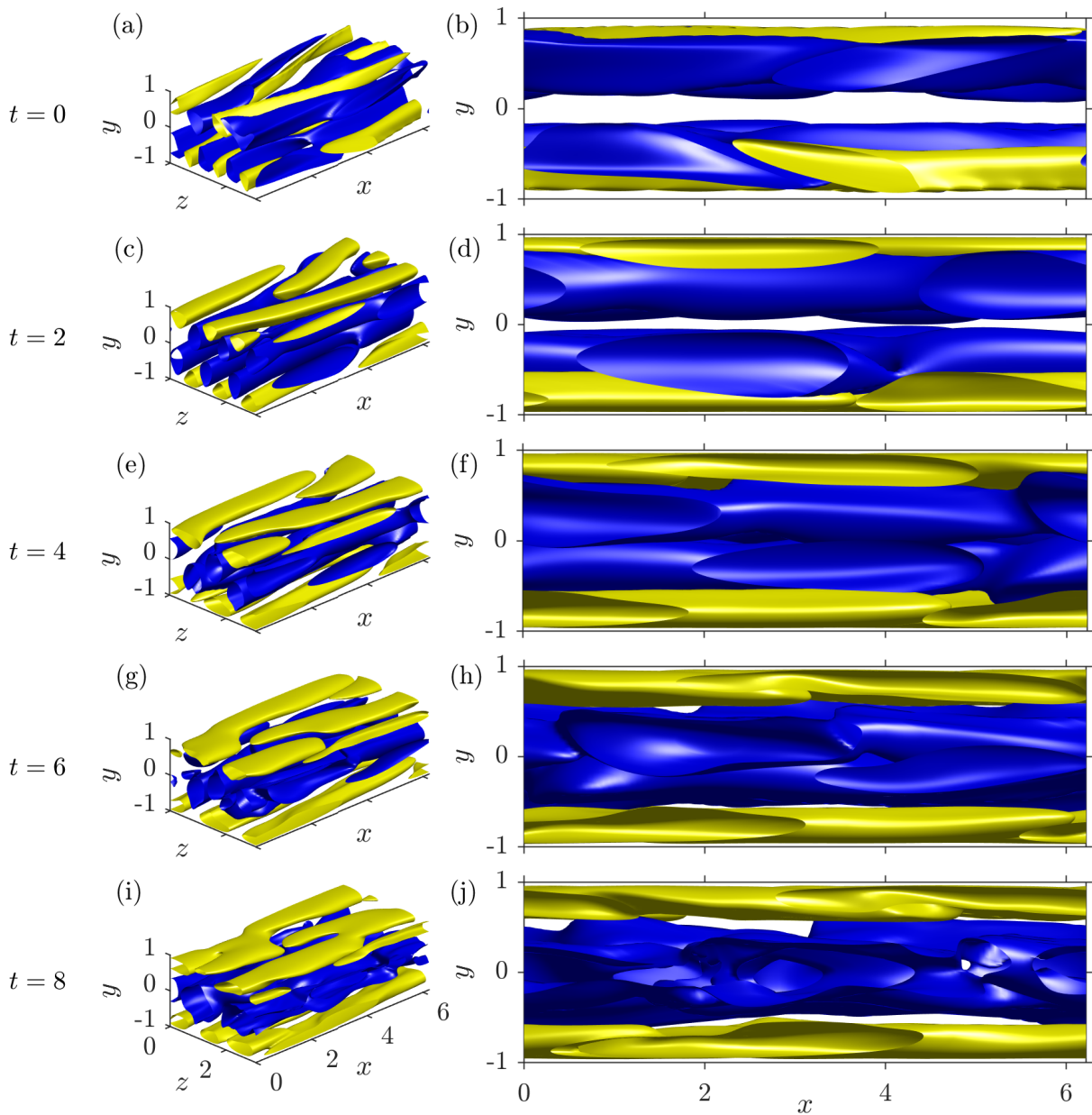


Figure 3.14: Evolution of the nonlinear unstratified optimal perturbation with  $E_0 = 10^{-2}$ , shown at two angles. The times of evolution are marked.

We detect similar optimal perturbation structures here for a channel flow, both in the unstratified and stratified cases. Their evolution in time by the modified Navier-Stokes equation is shown in figure 3.14 for the unstratified case. A modified lift-up mechanism similar to Cherubini et al. (2011) and Cherubini and De Palma (2013) is seen to be in operation, where low momentum fluid is lifted off the wall and high momentum fluid is brought closer to the wall by streamwise modulated vortices (vortices not shown). This translates into the algebraic growth of perturbation kinetic energy seen in figure 3.12.

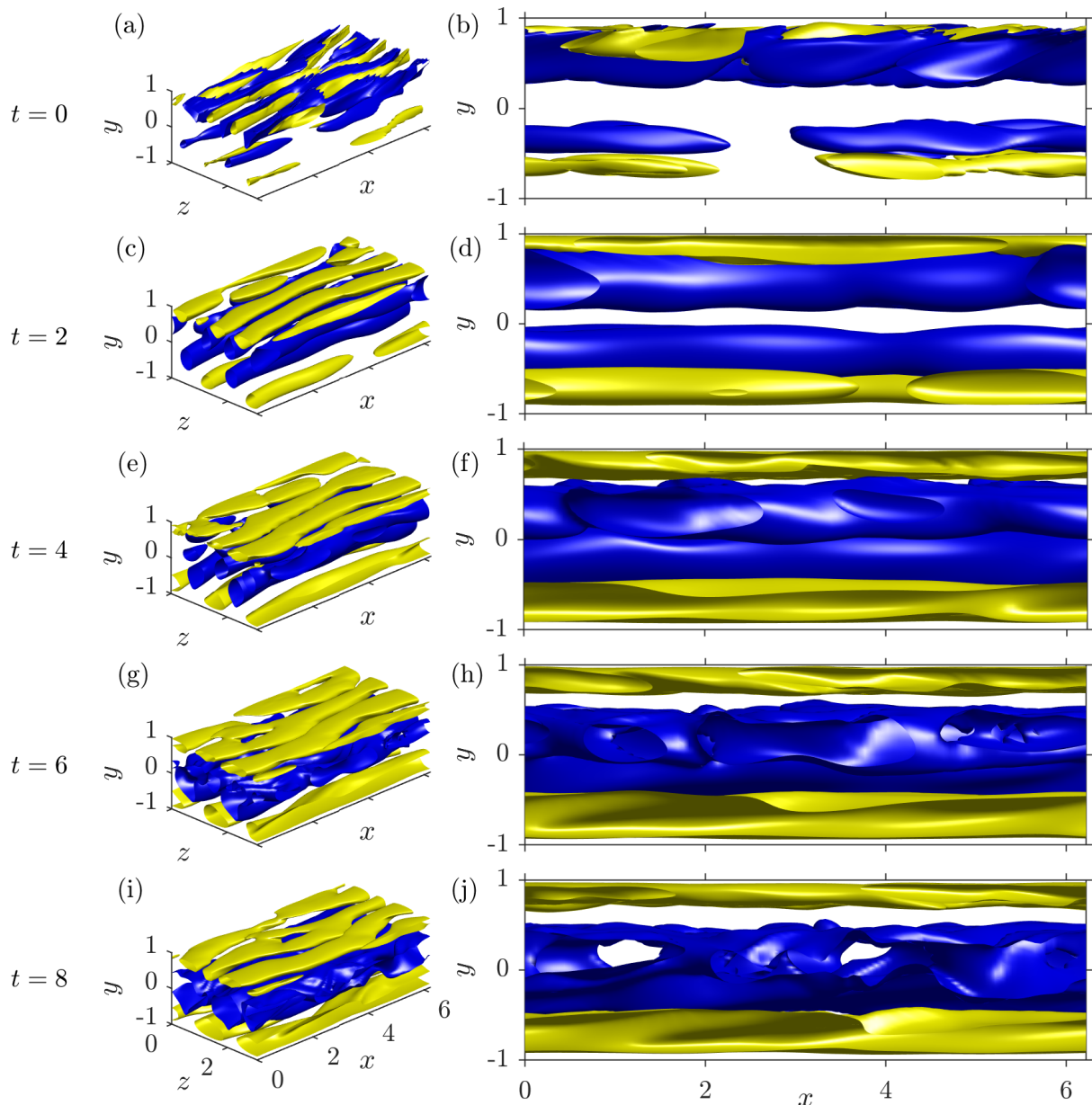


Figure 3.15: Evolution of the nonlinear viscosity-stratified optimal perturbation ( $\Delta T = 40$  K) with  $E_0 = 10^{-2}$ , shown at two angles. The times of evolution are marked.

The evolution of the nonlinear optimal perturbation in stratified flow is shown in

figure 3.15. As mentioned earlier, the inception of an inflection point due to lift-up may be expected to be more efficient near the less viscous wall as the wall-normal velocity gradient is larger, and lift-up is usually associated with  $u_2 \partial U / \partial y$  (Cherubini et al., 2011). Consistent with this, we have a larger population of optimal perturbation structures near the less viscous wall, as seen in figure 3.10(a) and (b). Since mean shear is smaller at the cold wall, its lift-up capability is lower, and therefore it may be argued that it is structures which are already a little away from the cold wall, which can grow better on the cold side. This is borne out by the optimal perturbation structures seen in the bottom half of figure 3.15(b). An interesting feature of the evolution of the viscosity stratified nonlinear optimal perturbation, which distinguishes it from the unstratified case as well as from the evolution of the linear optimal perturbation, is that as time progresses action at the cold wall is increasingly significant, and the high-speed structures at the hot wall shrink in wall-normal extent. The evolution of perturbations at the cold wall is strong enough to create points of inflection in the  $x - z$  averaged velocity profiles, and this will be discussed with the aid of figure 3.16. We shall refer to a “strengthening (weakening)” of inflectional profiles when the profile becomes more (less) strongly wavy in the wall-normal direction. In panel (a) of this figure, we see that the unstratified flow progresses steadily towards inflection, maintains this up to about  $t = 10$ , and become less inflectional thereafter. The profiles are symmetric. In fact the perturbations in all cases decay at long times. This is expected because we use a low Reynolds number and small target-time of optimisation which means the asymptotic state would be laminar. In figure 3.16(b) the evolution of the profile in the stratified case is shown. There is a strengthening of the inflectional profile at early times at both walls, with the hot wall being more inflectional. After about  $t = 4$ , the profile becomes weaker near the hot wall and more strongly inflectional than before on the cold side, before eventually weakening at long time. The corresponding profiles of the  $x - z$  averaged total viscosity are shown in figure 3.16(c). Upon comparing with the laminar viscosity profile, up to a time of about 10, on the colder side, we see that higher viscosity fluid from the cold wall has been lifted up towards the centreline and lower viscosity fluid from the central portion of the channel has been carried towards the wall. A similar exchange is visible on the hot side of the channel as well, but with opposite signs of viscosity change. At the long time of  $t = 16$ , we see a mixing of fluids. Below, we address the question: if lift-up is more efficient at the less viscous (hot) wall,

why do perturbations grow near the other (cold) wall?

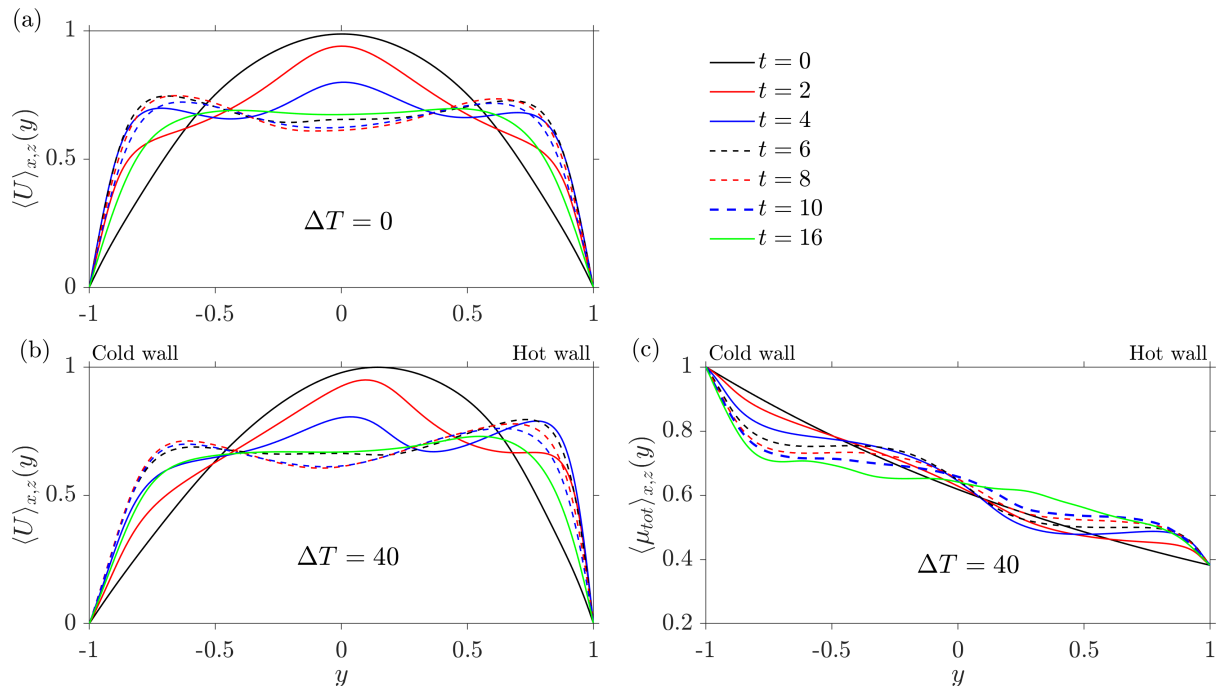


Figure 3.16: The total streamwise velocity at various times averaged across the  $x$  and  $z$  coordinates for (a) the nonlinear unstratified optimal perturbation and (b) the nonlinear viscosity-stratified optimal perturbation for  $\Delta T = 40$  K. (c) The evolution of the total viscosity profile for the flow corresponding to (b). Solid black lines in each for  $t = 0$ , solid red for  $t = 2$ , solid blue for  $t = 4$ , dashed black for  $t = 6$ , dashed red for  $t = 8$ , dashed blue for  $t = 10$ , and solid green for  $t = 16$ .

After the inception of lift-up, near the hotter wall, less viscous fluid of low momentum is brought away from the wall to the vicinity of more viscous and high momentum fluid, and the opposite happens on the colder wall. Thus the low (high) momentum streaks near the hotter wall are composed of less (more) viscous fluid, but those near the colder wall are composed of more (less) viscous fluid than the local laminar values. This is evident from the conditionally averaged viscosity profiles in figures 3.17(a) and 3.18(a) at time  $t = 2$  and 6 respectively. Here, at each  $y$  location, the viscosity  $\langle \mu_+ \rangle$  is averaged over all positive  $u_1$  cells over the  $x - z$  plane, and  $\langle \mu_- \rangle$  is the viscosity averaged over negative  $u_1$  cells in the same plane. A small cut-off  $\varepsilon = 0.001$  in the velocity has been used for this averaging, and it has been checked that the profiles are insensitive to the exact choice of  $\varepsilon$ . These plots establish that on the colder side of the channel, low speed regions are correlated with elevated viscosity, and high speed regions correlate with reduced viscosity,

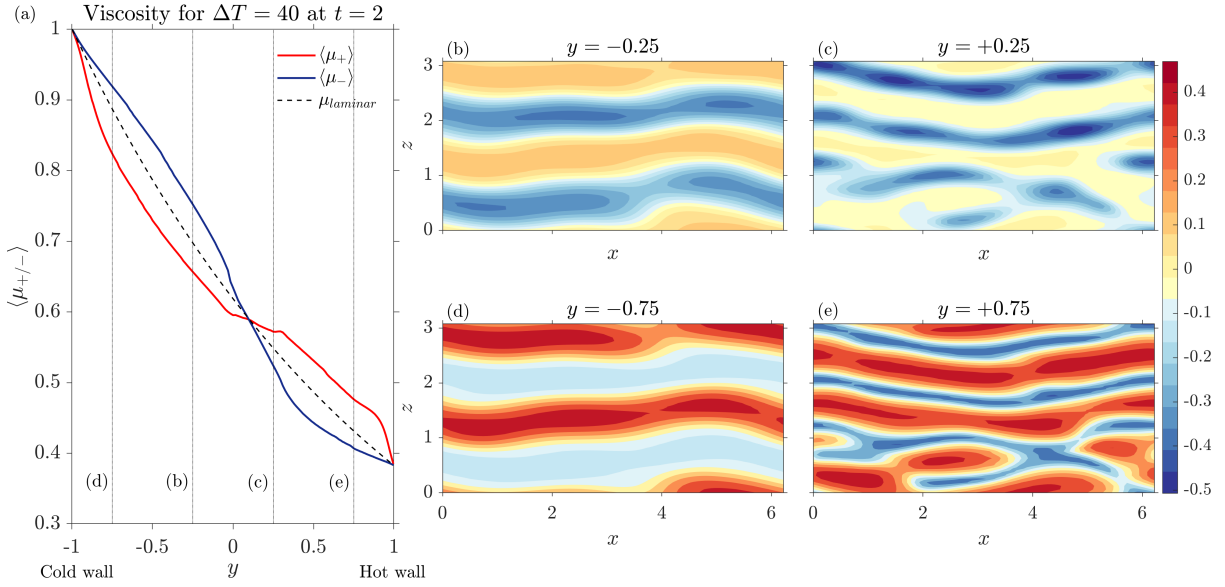


Figure 3.17: Flow driven by the nonlinear viscosity-stratified optimal perturbation at  $\Delta T = 40$  K and time  $t = 2$ . (a) Viscosity profiles averaged across the  $x$  and  $z$  coordinates for positive streamwise velocity perturbation  $u_1 > \varepsilon$  in red, and for  $u_1 < -\varepsilon$  in blue. The laminar viscosity profile is shown as a dashed black line. The four vertical black dotted lines with labels denote the  $y$  locations of the plots in (b-e). Instantaneous streamwise velocity perturbations  $u_1$  are shown in the  $x-z$  plane at  $y$  locations (b)  $-0.25$ , (c)  $0.25$ , (d)  $-0.75$ , and (e)  $0.75$ . Refer to figure 3.15(c) for a 3D view of isosurfaces of  $u_1$  at this time and the red solid line in figure 3.16(b) for the total  $U(y)$  averaged in  $x$  and  $z$  at this time.

with the opposite correlations on the hotter side. The instantaneous streamwise velocity perturbations in four different  $x-z$  planes are shown in figures 3.17 and 3.18 in panels (b) to (e). The spanwise widths and spacing of the low and high speed streaks is significantly larger on the cold side than on the hot side. Secondly the streaks persist up to  $t = 6$  on the cold side, whereas on the hot side the structure is practically lost by this time. A physical argument for the relative persistence near the colder wall is as follows. Consider that the streamwise pressure gradient is similar across the span of the channel. High speed streaks of low viscosity alternating with low speed flow of higher viscosity would be maintained by this pressure gradient. On the other side, i.e., at the hot wall, a higher viscosity fluid of higher forward speed would tend to slow down, and a higher viscosity fluid of lower speed up, in response to a similar streamwise pressure gradient. The greater persistence of streaks on the colder side is thus a consequence of the basic

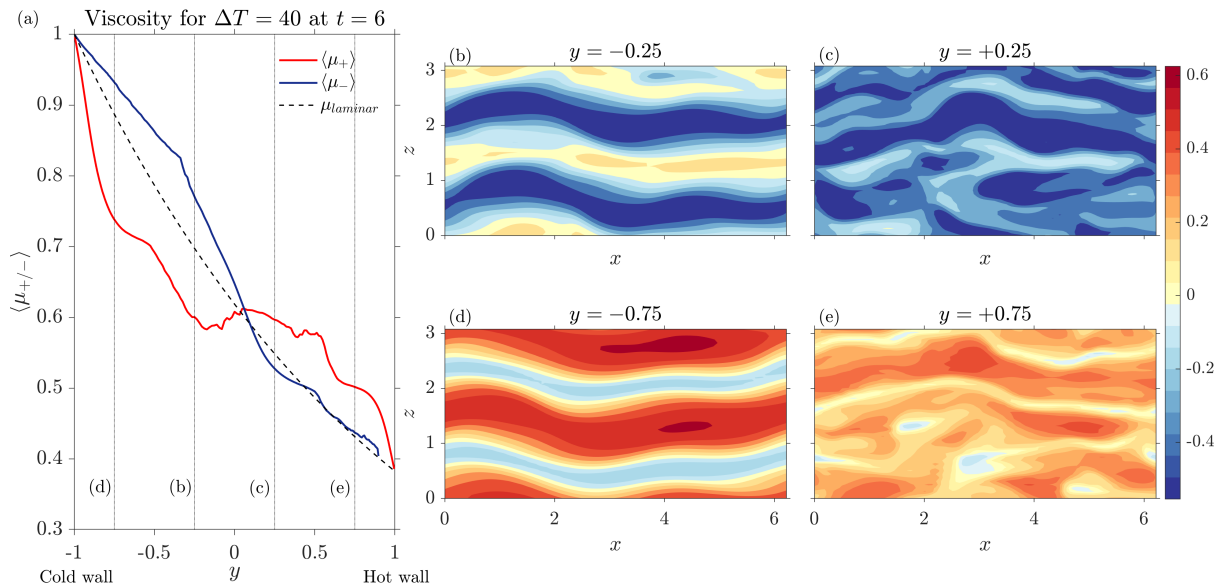


Figure 3.18: Same as figure 3.17 but for time  $t = 6$ . Refer to figure 3.15(g) for a 3D view of isosurfaces of  $u_1$  at this time and the black dashed line in figure 3.16(b) for the total  $U(y)$  averaged in  $x$  and  $z$  at this time.

asymmetry in the mechanics of the lift up on the two sides.

In figure 3.10(c) we had seen that the spanwise variation of the velocity perturbations had different apparent wavenumbers on the two walls. The slices in figures 3.17 and 3.18 clarify this to be a sinuous variation. Such variation is known to be responsible for the ultimate breakdown of streaks (Waleffe, 2009). A study at higher Reynolds number and longer target-time could reveal this. Besides, the inflectional instability, discussed below for the stratified case, extracts energy from the streaks (Waleffe, 2009) allowing further energy growth beyond the lift-up. Further studies at higher Reynolds numbers and longer target-times will be needed to explore these mechanisms in viscosity-stratified flows.

The observations in figures 3.16 to 3.18 enable us to schematically illustrate the lift-up process in stratified flow, in figure 3.19. Panel (a) shows stronger inception of inflection near the hot wall at early time. On the left of panel (b) we sketch how this lift-up results in exchange of viscosities. On the right of this panel, we see how this exchange of viscosities results in strengthening of the inflectional profile on the cold wall and weakening on the hot wall. Wherever viscosity is higher than the surrounding laminar flow, gradients are lowered and wherever it is lower, gradients are relatively increased.

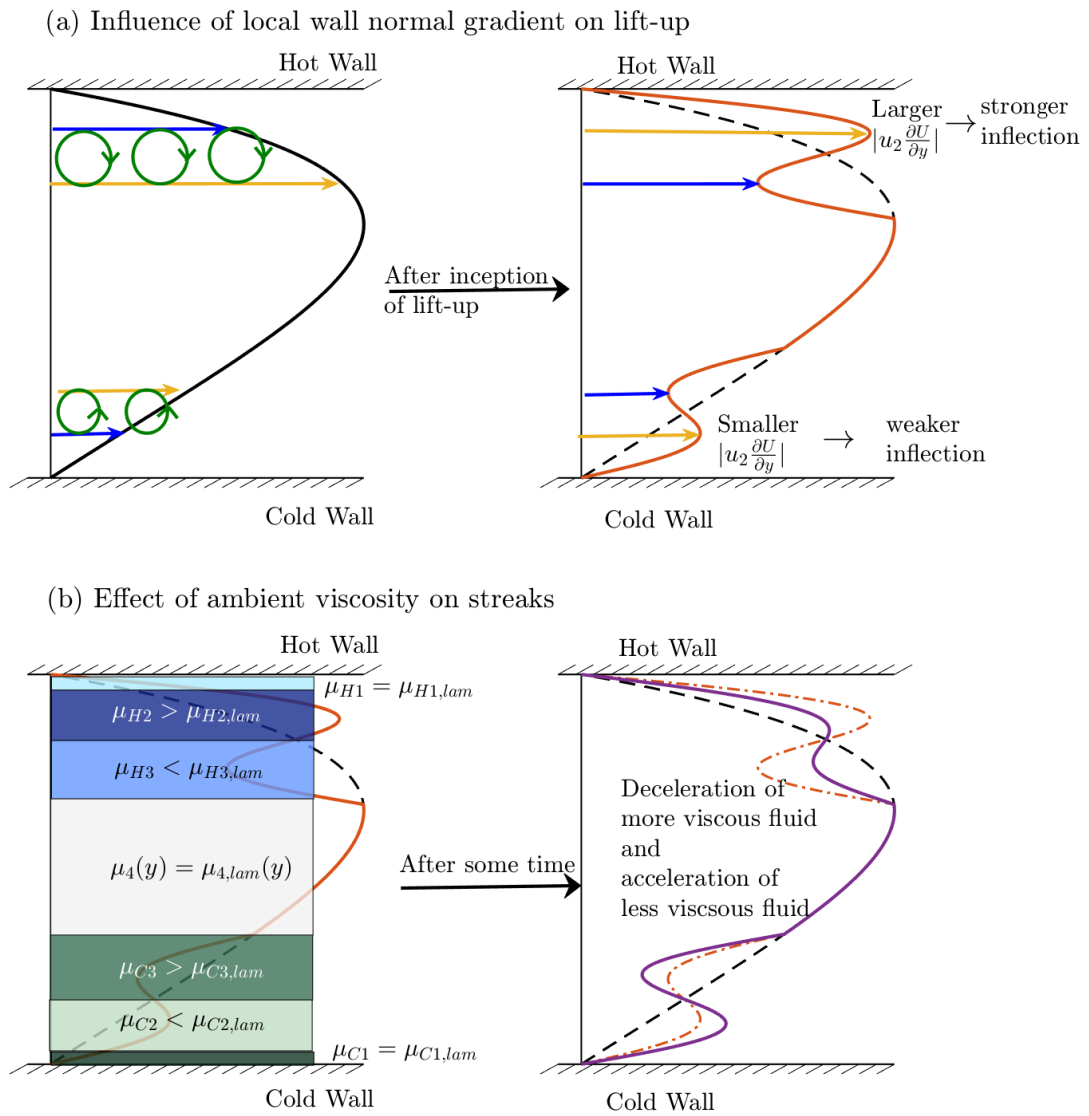


Figure 3.19: Schematic of the lift-up mechanism influenced by viscosity stratification: (a) inception of the inflection in the velocity profile is stronger near the less viscous wall as it has larger wall-normal velocity gradient, (b) persistence of the inflection created is greater near the cold/more-viscous wall because the streak  $C2$  of high momentum can sustain higher wall-normal gradients of velocity than before, whereas the streak of low momentum,  $C3$  has higher viscosity velocity gradients within it will be lowered. The opposite happens on the other wall where high momentum fluid  $H2$  has higher viscosity and low momentum fluid  $H3$  has lower viscosity than the local laminar value. The dashed line represents the undisturbed laminar profile, the dash-dotted line and the solid lines are representations of early and later times respectively.

Thus, the low viscosity streak at the cold wall brings with it higher velocity gradients, leading to stronger lift-up. The persistence of high momentum and low viscosity streaks, combined with stronger inflection in the velocity profile near the colder wall is consistent with the observations of previous DNS studies (Lee et al., 2013; Zonta et al., 2012) concerned with turbulence in stratified flow. In boundary layer flow (Lee et al., 2013) heating the flat plate and hence making fluid less viscous in the vicinity leads to suppression of turbulence and for channel flow (Zonta et al., 2012) turbulence is suppressed on the hot/less viscous wall and enhanced on the cold/more viscous wall. Cherubini et al. (2011) and Cherubini and De Palma (2013) highlight the importance of the Orr and lift-up mechanisms, both linear mechanisms, in the creation of sub-critical transition through minimal seeds of turbulence transition (obtained by optimizing over much larger target-times as compared to what we study in this chapter). Recently, Vavaliaris et al. (2020) also reported the dominance of these mechanisms in the initial stages of sub-critical turbulence in a boundary layer. We have shown how viscosity stratification in a channel acts to modify these mechanisms. For the short target-time ( $\mathcal{T} = 4$ ) optimal perturbations at the relatively small Reynolds number ( $Re = 500$ ) that we have studied, the interaction required for non-linear regeneration of the streaks and hence completing the regeneration cycle en-route to transition (Waleffe, 2009) is absent. But the primary role of viscosity stratification in the initial stages of the nonlinear nonmodal process has been revealed.

### 3.3.3 Effect of Prandtl number

We performed simulations at three Prandtl numbers:  $Pr = 0.1$ , 7 and 5000, for  $\Delta T = 20$  K. Our lowest Peclet number, i.e., the product of the Reynolds and the Prandtl numbers, is 50, which is too large for diffusion of the temperature perturbations to qualitatively change the behaviour over our simulation times. We confirm this in our simulations. Slices of temperature and viscosity perturbations are shown in figure 3.20 for two values of  $Pr$ , when evolved with the corresponding nonlinear optimal perturbation up to the target-time. We see that diffusion effects are greater at the lower Prandtl number, so viscosity variations persist better at the higher  $Pr$ , while we find very similar structures and their evolution (not shown) at all Prandtl numbers. However, in studies over longer target-times, of the process of transition to turbulence, we expect the Prandtl number to

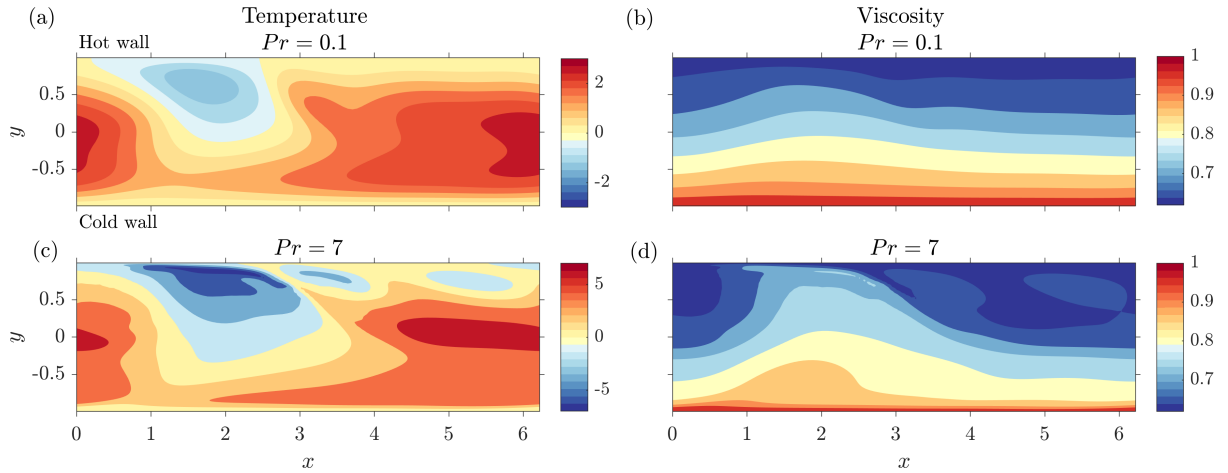


Figure 3.20: Temperature perturbations at target-time at  $z = \pi/2$  for (a)  $Pr = 0.1$  and (c)  $Pr = 7$  when started with the corresponding nonlinear viscosity-stratified optimal perturbation ( $\Delta T = 20$  K). The corresponding viscosity contours at same time are in (b) and (d). Note the presence of higher gradients in temperature and viscosity in (c) and (d), respectively. The colour bars in (a) and (c) are different.

play an important role.

### 3.4 Conclusions

In this study we have derived, for the first time to our knowledge, the adjoint modified Navier-Stokes equations for a viscosity-stratified flow. We have shown that viscosity stratification brings important modifications to the operation of the lift-up mechanism in the early stages of disturbance growth. Initially stronger lift up is set up at the hot (less viscous) wall due to the higher mean velocity gradient, but the lift-up at the cold (more viscous) wall increases in strength later, while that at the hotter wall weakens. Significantly, at the colder wall, high-speed streaks are more persistent, of larger spanwise extent, and give rise to a strengthening of the inflectional profile. We have presented physical arguments for these observations. Thus the action shifts from the hotter wall to the colder wall as time progresses. Most of the features we observe in the evolution of the nonlinear optimal perturbation are completely missed in the linear study. A linear optimal perturbation of small amplitude will only display the Orr mechanism and not the lift-up. At higher amplitudes, lift up will be seen, but only at the hot wall. In fact no perturbations are ever seen near the cold wall with the linear optimal perturbation.

This work suggests several directions for future research. A starting point for understanding the role of viscosity stratification in the transition to turbulence will be the study of nonlinear optimal perturbations over long target-times. Vermach and Caulfield (2018) made an interesting finding that the initial condition which produces the most efficient mixing could be quite different from that which gives the highest energy growth. Recognising that most flows where questions about mixing are relevant are also stratified in viscosity indicates this as an area of study. We expect the effect of Prandtl number to be pronounced in flows with a sharp stratification, e.g., the flow of miscible fluids of different viscosity, and also at long times in continuously stratified flows, and this bears investigation. We have neglected gravity in this study but most flows with a composition to temperature variation are subject to buoyancy effects. This combination will make for interesting study. Given the number of industrial applications for which viscosity stratification is important, a variety of experimental studies are called for.

Finally, oceanic flows are also of varying viscosity but in that case it is the turbulent eddy viscosity that would be of importance and not molecular viscosity as studied in this chapter. We hope that this first work on the effects of viscosity stratification in nonlinear optimal perturbation growth will give rise to discussions on how to implement such stability analysis for real-life flows like oceans. As have been mentioned earlier, some of these model studies had been inspired from oceanographic observations in the Bay of Bengal. From the next chapter onwards, we describe some of these oceanic observations, and we can see that some are not well understood. We believe that the numerical tools that have been developed in this first half of the thesis could prove useful in improving understanding of more complicated oceanic flows.

# Ocean turbulence with $\chi$ pods

\*\*\*

With this chapter we move on to the next half of thesis concerned with turbulence measurements in the ocean. Some of the observations presented in this and the next two chapters had inspired some of the earlier model studies on nonmodal fluid stability. To understand the turbulence observations, we first describe the measurement of ocean turbulence using mixing meters called  $\chi$ pods developed first in Moum and Nash (2009).  $\chi$ pods are fitted with thermistors, Pitot tube, and other sensors which are required to measure various flow quantities in the ocean to infer geophysical turbulence. We will first discuss the theoretical principles behind turbulence measurements and how it has been applied to the measurements from  $\chi$ pods. We then describe the raw signals that are necessary to infer turbulence and the instruments used for the same. The turbulence data from the Bay of Bengal that will be discussed later in this thesis is based on turbulence measured by  $\chi$ pods.

## 4.1 Introduction

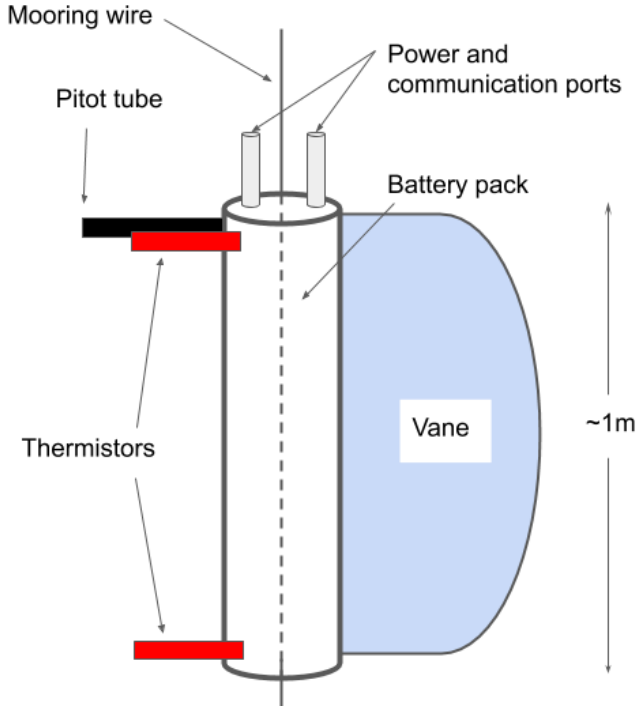
The direct methods of oceanic turbulence measure the vertical momentum or buoyancy fluxes,  $\overline{w'\rho'}$  or  $\overline{w'b'}$  (where  $w'$ ,  $\rho'$ , and  $b'$  are vertical velocity, density, and buoyancy fluctuations from some mean) (Moum, 1990; Osborn and Crawford, 1980; Osborn and Lueck, 1985a,b). These measurements are limited due to the instrument's inability to capture small correlations of velocity and density measurements and are difficult to interpret due to the natural unsteadiness of turbulence (Gregg, 1987; Ivey et al., 2008). The measurements of these correlations could also be contaminated due to vibrations if the

instruments are fixed on moorings or gliders (Rudnick et al., 2004) to obtain long-term turbulence data. Another critical measurement is of the vertical velocity fluctuation  $w'$  in phase with density fluctuations. However, short-term measurements of turbulence have been collected with this principle of direct measurement using vertically falling shear probes (e.g., Moum (1990)). Oceanographers and others interested in long-term turbulence data, rely on indirect estimates that infer dissipation of turbulent kinetic energy and temperature variance, using theories devised by Osborn and Cox (1972) and Osborn (1980). These estimates of turbulence are based on the premise that vigorous stirring will eventually generate small scales of motion and at these scales, molecular diffusion will dissipate momentum, temperature, and salinity alike. And hence, measurement of the rate of that smallest-scale dissipation would give an estimate of the strength of turbulence. Mixing meters called  $\chi$ pods infer turbulence by this indirect method.

## 4.2 $\chi$ pods

$\chi$ pods, as shown in figure 4.1 are about a meter long, 0.1m diameter cylindrical casings with a thermistor and a Pitot tube at the top cap of the casing, another thermistor (to act as a contingency against non-functionality of the first one) at the bottom cap, a pressure transducer, and a streamlined vane along the casing length opposite to the sensors to direct them to face the mean flow.  $\chi$ pods can be fixed to the line or wire of a mooring and can be deployed for many months at a time. It has yielded turbulence data at various sites across the globe, from the Pacific to the Indian Ocean (Cherian et al., 2020; Moum et al., 2013; Pujiana et al., 2018; Thakur et al., 2019; Warner et al., 2016; Warner and Moum, 2019). Not that it can be fixed only to a mooring, but very recently, a miniature version of  $\chi$ pod have also been attached to a buoyant structure and towed behind a research vessel to measure spatial variations of upper-ocean turbulence in the Western Pacific (Hughes et al., 2020).

The long body of the  $\chi$ pod consists of a battery and circuit boards designed to carry out conversion, reduction and storage operations of the recorded analog signal. The most recent version of  $\chi$ pods record temperature using fast thermistors, current speed ( $u$ ) with Pitot tubes (Moum, 2015), pressure, and acceleration at 50 Hz. In an earlier version, the velocity field required to infer the flow past a  $\chi$ pod was done using ancillary velocity



(a) A schematic of a  $\chi$ pod attached to a mooring wire, showing thermistors and the Pitot tube among others.



(b) A  $\chi$ pod on a mooring wire before deployment. From Moum and Nash (2009). ©American Meteorological Society. Used with permission.

Figure 4.1: Mixing meter  $\chi$ pod.

data, like from that of an acoustic Doppler current profiler (ADCP). The time rate of temperature change ( $T_t$ ) is measured at 100 Hz, and compass heading is sampled at 1 Hz. Acceleration and the compass heading is required to decompose the speed calculated using the Pitot tube into its  $x$ ,  $y$ , and  $z$  components. The integrated motion of accelerometers also provide the vertical motion of the  $\chi$ pod. As discussed later, speed is used to convert temperature fluctuations in time to spatial fluctuations using Taylor's frozen flow hypothesis (Taylor, 1938). An iterative algorithm (Moum and Nash, 2009) is used to determine the decay rate of temperature variance ( $\chi$ ) using an inferred turbulent kinetic energy dissipation rate ( $\epsilon_\chi$ ), as  $\epsilon_\chi = \frac{N^2 \chi}{2\Gamma T_z^2}$ . Here,  $T_z$  is the mean vertical temperature gradient and square of Brunt-Väisälä  $N^2 = -g\rho \cdot d\rho/dz$ , where  $\rho$  is the fluid density.  $\Gamma$  is related to the efficiency of turbulent mixing and is set at 0.2 (Gregg et al., 2018; Osborn, 1980) and is discussed in 4.3.1. Because turbulence inference using  $\chi$ pods amounts to measuring  $\chi$  in the ocean, hence the instrument is named so.

### 4.3 Theoretical principles

The theoretical principle that underlies the indirect estimates of turbulence presented here is based on the formulations of Osborn and Cox (1972) and Osborn (1980).

For any conserved passive tracer (like temperature) in a flow,

$$\frac{\partial T}{\partial t} + \mathbf{u} \cdot \nabla T = D_t \nabla^2 T. \quad (4.1)$$

It is a local conservation (in time  $t$ ) equation for instantaneous temperature (or any other scalar) field  $T$  advected by instantaneous velocity field  $\mathbf{u}$ . Molecular diffusivity  $D_t$  acts to smoothen temperature gradients at the dissipation scales which are much smaller than the forcing scales.  $\nabla$  is the divergence operator and  $\nabla^2$  is the Laplacian operator. The fluctuation temperature variance conservation equation, derived by Reynolds decomposition of the instantaneous temperature advection-diffusion equation (4.1) and multiplying it by fluctuation  $T'$  is

$$\frac{\partial \overline{T'^2}}{\partial t} + U_i \frac{\partial \overline{T'^2}}{\partial x_i} + \frac{\overline{u'_i \partial T'^2}}{\partial x_i} + \underbrace{2 \overline{u'_i T'} \frac{\partial \overline{T}}{\partial x_i}}_P = D_t \frac{\partial}{\partial x_i} \frac{\partial \overline{T'^2}}{\partial x_i} - \underbrace{2 D_t \overline{\left[ \frac{\partial T'}{\partial x_i} \right]^2}}_\chi. \quad (4.2)$$

It is important to note that primes denote the fluctuation quantities (and not derivatives) and overbars denote appropriate averages. The 3-dimensional instantaneous velocity field  $\mathbf{u}$  is also Reynolds decomposed into mean  $U_i$  and fluctuations  $u'_i$ .

In a steady and homogeneous shear turbulence, from equation (4.2) we are left with a balance between the turbulent production of scalar gradients by velocity fluctuations ( $P$ ) and the irreversible dissipation of the those gradients by molecular diffusivity ( $\chi$ ) (Pope (2000), Kundu and Cohen (1990)).  $\chi$ , which is the product of molecular diffusivity of temperature and the square of the temperature fluctuation gradient, is the only sink in the above equation. Hence, whatever variance is produced, is destroyed only by molecular diffusivity at small wavelengths (or high wavenumbers), similar to what viscosity does to velocity gradients. We assume that the mean temperature gradient, from which this variance is being extracted, is present only in the vertical direction, i.e, the balance of  $P$  and  $\chi$  in equation 4.2 can be approximated as

$$2\overline{u'_i T'} \frac{\partial \overline{T}}{\partial x_i} \equiv 2\overline{w' T'} \frac{\partial \overline{T}}{\partial z} = -\chi. \quad (4.3)$$

This assumption is justified by the fact that in a majority of ocean profiles, the temperature gradient is primarily in the vertical, and horizontal gradients are orders of magnitude smaller than the vertical gradient.

Osborn and Cox (1972) assumed an eddy coefficient approach for the production term, where correlations of vertical velocity fluctuation and temperature fluctuation is parametrised to be only dependent on the strength of the vertical gradient, i.e.  $\overline{w' T'} = -K_t \overline{\partial T / \partial z}$ , where  $K_t$  is the parameter which measures the strength of this correlation with respect to the vertical gradient. This quantity is named the turbulent (or eddy) diffusivity of temperature (or heat).  $K_t$  is however a synthetic quantity and is not a property of the fluid but of only of the flow. From equation 4.3 and Osborn and Cox (1972) parametrisation,

$$K_t = \frac{\chi}{2T_z^2}. \quad (4.4)$$

$\chi$  in the ocean is measured using  $\chi$ pods and the turbulent diffusivity  $K_t$  is inferred. The quantity  $K_t$  is the basis of other analysis presented in this thesis.

The buoyancy flux is also modelled as an eddy coefficient formulation following Osborn (1980) as in equation (4.5). The production of the buoyancy flux  $J_b$  is dependent only on the mean Brunt-Väisälä frequency,  $N^2$ . Assuming a constant flux Richardson number, the equality in (4.5) can also be represented in terms of the rate of dissipation of turbulent kinetic energy  $\epsilon$ .  $N^2$  is a representative of the background density stratification over which turbulent eddies create stirring motion.

$$J_b = K_\rho N^2 = \Gamma \epsilon. \quad (4.5)$$

$K_\rho$  is the proportionality constant and is the diffusivity of density analogous to diffusivity of temperature introduced in equation 4.4.

Using a constant value of  $\Gamma = 0.2$  was first argued for by Osborn (1980). This quantity represents how much gain in potential energy is obtained by a mixing event due to the carrying of a high-density fluid to a lower-density neighbourhood in a stratified flow. The higher the value, low is the loss of energy to viscous dissipation and more is the gain in

potential energy of the flow.

We assume that the turbulent Prandtl number is unity, i.e., temperature, salinity, density and any other scalar diffuse at the same rate as the velocity. By equating the turbulent diffusivities of temperature and density, we have an estimate of the viscous dissipation of turbulent kinetic energy. With  $K_t = K_\rho$ ,

$$\epsilon_\chi = \frac{\chi N^2}{2\Gamma T_z^2}. \quad (4.6)$$

We name it  $\epsilon_\chi$  because this dissipation of turbulent kinetic energy is not obtained directly from direct measurements of turbulence like with microstructure profilers (see, for example, Gregg (1989) among many), but is rather inferred from rate of temperature dissipation  $\chi$ . This whole set of equations forms the looping algorithm for our analysis shown as a schematic in figure 4.3 and will be discussed in section 4.4.

### 4.3.1 Mixing efficiency $\Gamma$

The quantity  $\Gamma$  deserves a special mention as it has been a source of intense debate regarding what the actual efficiency of mixing is for oceanic flows (reviews of Ivey et al. (2008) and Gregg et al. (2018)). We are aware of studies that express concern about using a constant  $\Gamma$  by showing it to have a dependence on the buoyancy Reynolds number ( $Re_b$ ) or the strength of turbulence in the flow (Monismith et al., 2018). They present different critical  $Re_b$  above which the flow is  $Re_b$ -dependent and below which the flow is a constant- $\Gamma$  flow. The scaling with  $Re_b$  was however found to be not universal by Mater and Venayagamoorthy (2014). This means a complete functional form of  $\Gamma$  is yet to be uncovered. We agree that instantaneous  $\chi$  values would change due to a sensitivity to  $\Gamma$ , but as presented in the appendix of Moum and Nash (2009), this sensitivity is about 30% for a  $\Gamma$  range of 0.1-0.35. So, assuming a constant  $\Gamma$  at 0.2 should not qualitatively change the analysis presented in this thesis. Also, in a recent review, Gregg et al. (2018) suggests that the use of a constant value of  $\Gamma = 0.2$  could be continued until “observations, laboratory experiments, and numerical simulations converge on a more accurate formulation.”

### 4.3.2 Spectrum of turbulence

We can expand any time-varying function  $T'(t)$  as a series of its constituent frequencies (Fourier, 1822). For any spatially varying  $T'(x)$ , we can expand it into its constitutive wavenumbers,

$$T'(x) = C \int_a^b \hat{T}'(k) \exp^{ikx} dk, \quad (4.7)$$

where  $x$  is the horizontal direction in our frame of measurements, i.e., parallel to the surface of the ocean,  $k$  is the wavenumber space of  $x$ ,  $a$  and  $b$  are the spatial bounds in  $k$ ,  $C$  is a constant, and  $\hat{T}'(k)$  the Fourier transform of  $T'(x)$ . For such a one-dimensional spatial function, Parseval's theorem states that the variance in the real space is equal to the variance in the wavenumber space. If we define a function  $\psi_{T_x}(k)$ , which is a power spectral density for the variance in the wavenumber space, we have

$$\overline{\left[\frac{dT'}{dx}\right]^2} = \int_0^\infty \psi_{T_x}(k) dk. \quad (4.8)$$

Hence  $\psi_{T_x}$  is the temperature fluctuations gradient spectrum. For isotropic turbulence,  $2D_t \overline{\left[\frac{\partial T'}{\partial x_i}\right]^2} = 6D_t \overline{\left[\frac{dT'}{dx}\right]^2}$ . Hence, from equation 4.2 and equation 4.8, we have

$$\chi = 6D_t \int_0^\infty \psi_{T_x}(k) dk. \quad (4.9)$$

This can also be represented in terms of integral in frequency  $f = k/u$ . For the sake of easing future discussions, we can safely assume the velocity  $u$  to be unity and write  $\chi$  as,

$$\chi = 6D_t \int_0^\infty \psi_{T_x}(f) df. \quad (4.10)$$

The spectrum of turbulence was coined for homogeneous isotropic turbulence by Taylor (1938). After scaling arguments for energy distributions, Kolmogorov (1941) and Obukhov (1941) established the existence of such a spectrum with a  $k^{-5/3}$  scaling in the inertial subrange of a turbulent flow. The inertial subrange is a spectral range where the effect of viscosity has not yet taken place (i.e., the length scales in the flow are bigger than the Kolmogorov length scale). However, we are not concerned with the spectrum of velocity fluctuations but that of the passive scalar in the flow. As the scalar is advected in a flow and the eddies break down to smaller and smaller scales, equivalent destruction

in the scales of a scalar occurs and hence the spectrum exists.

The scalar spectrum has a non-monotonic form with the contribution from each sub-range marked (e.g., see Dillon and Caldwell (1980); Tennekes and Lumley (2018)):

$$\psi_{T_x}(k) = [\text{internal waves}] + \chi \left[ \underbrace{C \epsilon^{\frac{-1}{3}} k^{\frac{1}{3}}}_{\text{inertia-convective}} + \underbrace{q \nu^{\frac{1}{2}} \epsilon^{\frac{-1}{2}} k}_{\text{viscous-convective}} \right] + [\text{viscous-diffusive}]. \quad (4.11)$$

Here  $\nu$  is the viscosity of the fluid,  $C$  and  $q$  are constants and their numerical values have been postulated to be 0.4 and 2.3 respectively in Sreenivasan (1996) and Klymak and Moum (2007). A schematic of the spectrum is shown in figure 4.2 with the various subranges. In the inertia-convective subrange as marked in equation (4.11) and in figure 4.2 between  $k_1$  and  $k_2$ , temperature is simply advected around like a passive parcel. This is because neither viscosity nor molecular diffusivity makes an appearance in this subrange. In the viscous-convective subrange, which is higher in the wavenumber space (and hence smaller length scale), as marked in figure 4.2 between  $k_2$  and  $k_3$ , temperature is still advected without any dissipation but the velocity gradients are being continuously destroyed by the action of viscosity at the Kolmogorov scale. It can be seen from equation (4.11) that viscosity  $\nu$  makes its first appearance in the spectrum only in this subrange. At the extreme end of the spectrum, called the viscous-diffusive subrange, both the gradients in temperature and velocity are being smoothed out by the action of molecular diffusivity of temperature and viscosity, respectively. The scaling arguments of the inertia-convective subrange was first suggested by Corrsin (1951) and Obukhov (1949). The form of the viscous-convective subrange is attributed to Batchelor (1959) and has been confirmed to exist by measurements of Gibson and Schwarz (1963). A model with non-uniform straining of scalar field was considered by Gibson (1968) as opposed to the uniform straining model of Batchelor (1959), and still the scaling in the viscous-convective subrange was preserved. Kraichnan (1968) took into account the intermittency effects of velocity field and arrived at scaling which preserved the earlier scaling by Corrsin (1951), Obukhov (1949), and Batchelor (1959). Hence, there are strong reasons to believe that the scalar spectrum of the form (4.11) is universal.  $\chi$  pods are capable of resolving turbulence in the viscous-convective subrange. The viscous-diffusive subrange occurs at very small length scales and has an exponential cutoff. We cannot resolve this small-scale subrange from our measurements and hence it has been left out of discussion. Bogucki et al.

(1997) and Yeung et al. (2002) found using direct numerical simulations that the scaling arguments of Kraichnan (1968) holds better than Batchelor (1959) in the viscous-diffusive subrange ( $> k_3$  in figure 4.2).

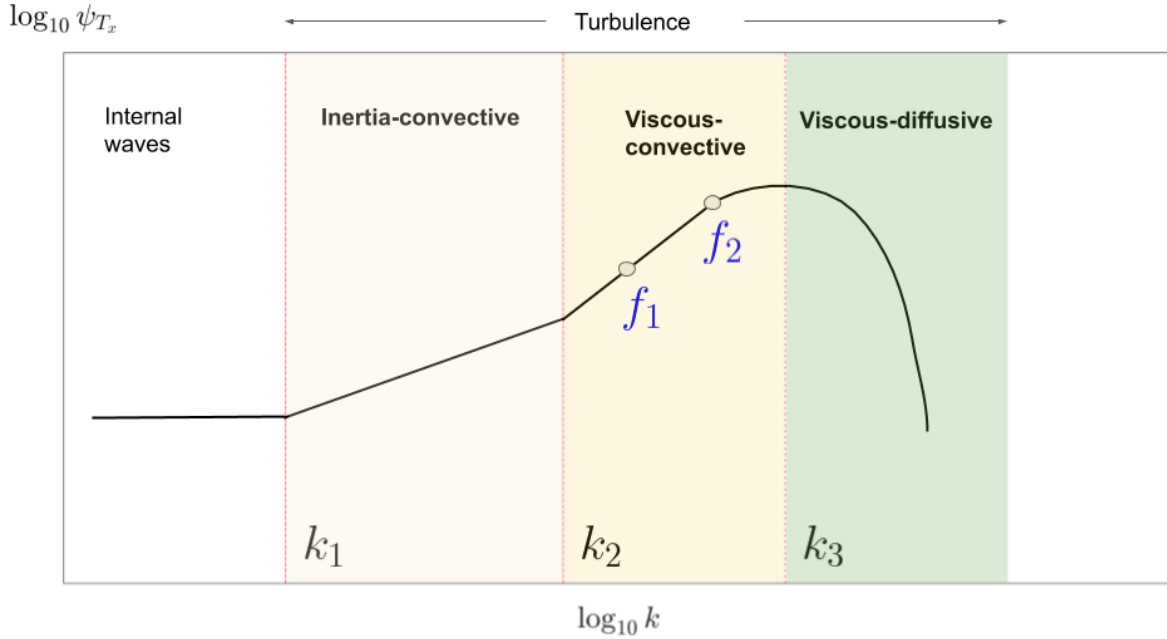


Figure 4.2: A log-log plot showing a schematic of scalar variance whose form is given in equation (4.11) for a fixed turbulent kinetic energy dissipation  $\epsilon$ . The internal wave part of the spectrum has a zero slope.  $k_1$ - $k_2$  is the inertia-convective subrange of scalar turbulence, while  $k_2$ - $k_3$  is the viscous-convective subrange.  $f_1$ - $f_2$  is the thermistor frequency range resolved by the  $\chi$ pod as mentioned in the iteration loop in figure 4.3. The subrange  $> k_3$  is viscous-diffusive part of turbulence. Spectrum is not to scale. (After Becherer and Moum (2017, Fig 1)).

#### 4.4 Iterative procedure to calculate $\chi$

We detail here the iterative looping algorithm based on the equations in section 4.3 for estimating  $\chi$  using  $\chi$ Pods. The looping is represented as a schematic in figure 4.3. We need an iterative technique because the spectrum depends on both  $\chi$  and  $\epsilon$  as in equation (4.11) but we only have measurements of temperature fluctuations and we can resolve only a part of the spectrum. The iteration is used to determine the decay rate of temperature variance ( $\chi$ ) using an inferred turbulent kinetic energy dissipation rate ( $\epsilon_\chi$ ) as  $\epsilon_\chi = \frac{N^2 \chi}{2\Gamma_z^2}$ .

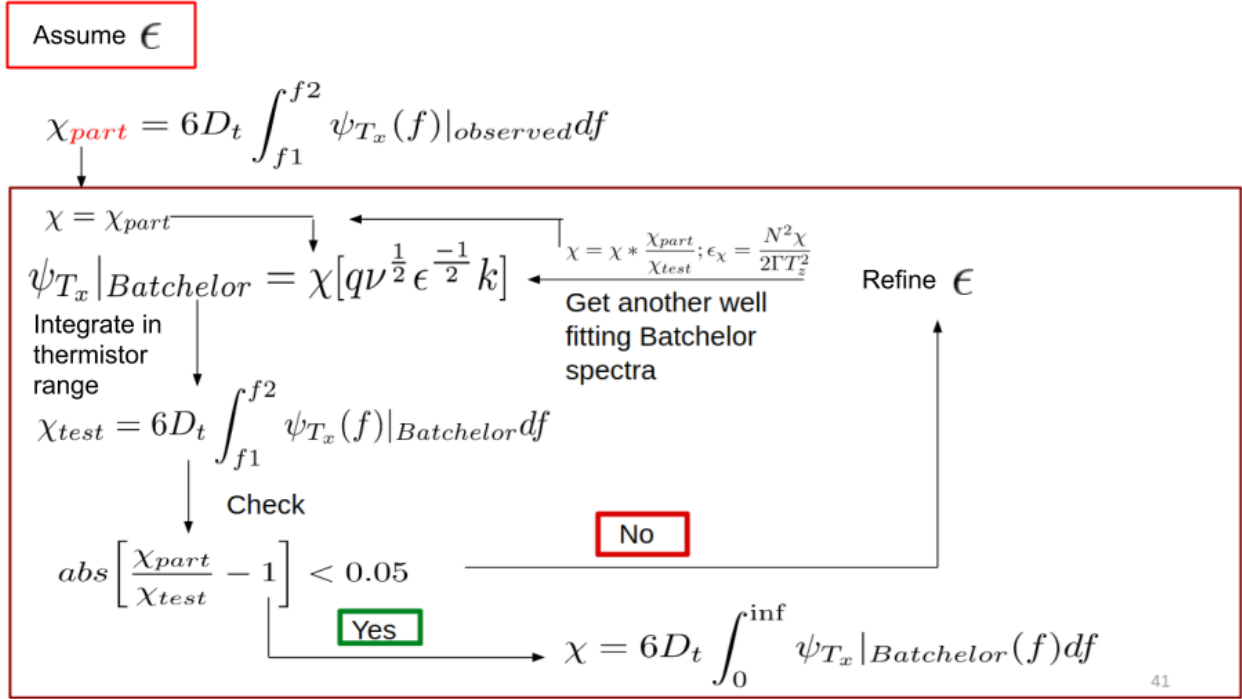


Figure 4.3: The looping algorithm used to find the best fitting theoretical Batchelor spectrum in the viscous-convective subrange.  $\chi$  is determined from the full integral of that theoretical spectrum.

For the first step in the iteration, the  $\epsilon_{\chi}$  is a guess. Apart from high frequency temperature fluctuations, we need reliable measurements of vertical temperature gradient  $T_z$ , the vertical stratification in density  $N^2$ , and the speed of flow past the  $\chi$ pod to complete this iterative looping.

Theoretically, after we measure the spectrum of temperature dissipation as in equation (4.8), we could have obtained  $\chi$  using the integral in equation (4.10). This is, however, avoided for two reasons. Firstly, when the flow speed is high or the turbulent dissipation  $\epsilon$  is high, the spectrum is pushed to higher wavenumbers (see, e.g., Shroyer et al. (2018, Fig 8)). This means, very high frequency measurements of temperature fluctuations would be required to resolve the spectrum. This is not possible even with the fastest of the glass rod thermistors available, which responds somewhere between 20-30 Hz (Gregg and Meagher, 1980). This is a challenge to the method of estimating turbulence using microstructure measurements of temperature. But the strength of this technique lies in the fact that the spectrum is relatively robust to platform noise and hence can provide long-term turbulence data as has been mentioned already. Secondly, surface wave signals

act as contamination to the temperature spectra somewhere in the inertia-convective and the viscous-convective subrange (Becherer and Moum, 2017, Fig 10). Hence, the full integration in equation (4.10) will be erroneous. This necessitates estimating  $\chi$  using a part of the measured spectrum and not by integrating the whole. In this analysis, we scale the 1-second spectrum as measured by the  $\chi$ pod to the theoretical Batchelor spectrum in the viscous-convective subrange. As this is not the full  $\chi$ , we name it  $\chi_{part}$  in the looping schematic in figure 4.3. We then try to fit this  $\chi_{part}$  to the integral of a theoretical spectra in the same frequency range and calculate the full  $\chi$  by integrating the whole theoretical spectra. The iteration loop can be decomposed into the following steps (also refer to figure 4.3).

1. Assume a certain rate of turbulent kinetic energy dissipation  $\epsilon$ . The current guess is  $\sim 10^{-7}$ .
2. From the measured spectra of temperature gradient from the ocean  $\psi_{T_x}(f)|_{observed}$ , we choose a range  $f_1$  to  $f_2$ , and the limits of the integral in equation (4.10) becomes

$$\chi_{part} = 6D_t \int_{f_1}^{f_2} \psi_{T_x}(f)|_{observed}(f)df. \quad (4.12)$$

3. In the same range of  $f_1 - f_2$  we try to find a theoretical Batchelor spectrum  $\psi_{T_x}(f)|_{Batchelor}$  (whose nondimensional form is shown in figure 4.2) which when integrated in  $f_1 - f_2$  gives an estimate  $\chi_{test}$ .
4. If  $\chi_{test}$  and  $\chi_{part}$  are not within a certain tolerance (5 % is used in this analysis),
  - we change our guess of  $\epsilon$ , which gives a new Batchelor spectrum (the spectrum depends on  $\epsilon$  as in equation (4.11)),
  - and steps 2 and 3 are repeated.
5. If  $\chi_{test}$  is matched with  $\chi_{part}$  within the tolerance, we assume to have found the theoretical Batchelor spectrum that we need for the full integration of equation (4.10).
6. After finding the actual theoretical spectrum  $\psi_{T_x}(f)|_{Batchelor}$ , we calculate  $\chi$  using the full integral in equation (4.10) as,

$$\chi = 6D_t \int_0^\infty \psi_{T_x}(f)df \equiv 6D_t \int_0^\infty \psi_{T_x}(f)|_{Batchelor}(f)df. \quad (4.13)$$

Temperature gradient spectra ( $\psi_{T_x}$ ) are calculated on 1-second sections, thus outside the surface wave band ( $\sim 4$ -20 s). Fitting over a short time range also lends confidence to the assumption that turbulence in that range is stationary and Taylor's frozen flow hypothesis is valid. Mean temperature and salinity (from conductivity-temperature-depth probes) was sampled more slowly with effectively 10 minute-resolution so that surface wave contributions are averaged out of these data. We use a 10-minute average ( $\langle\chi\rangle$ ) from 1-second individual estimates of  $\chi$  to derive 10-minute estimates of turbulent diffusivity  $K_t$  as,

$$K_t = \frac{\langle\chi\rangle}{2T_z^2}. \quad (4.14)$$

A raw signal of  $\chi$  and the turbulent diffusivity  $K_t$  for a few random days obtained from the Bay of Bengal is shown in figure 4.4.

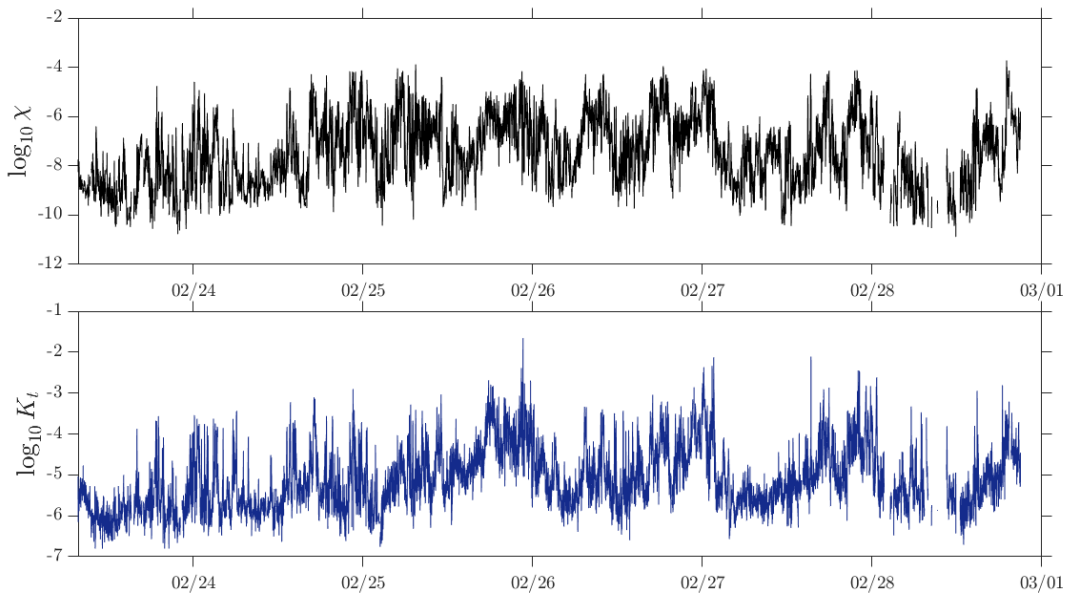


Figure 4.4: A raw signal of (a) temperature variance ( $\log_{10} \chi$ ) as obtained from a  $\chi$ pod and the (b) inferred turbulent diffusivity ( $\log_{10} K_t$ ) for a randomly-chosen period of seven days in the month of February 2015 in the Bay of Bengal.

### 4.4.1 Temperature fluctuations

A Reynolds decomposition of temperature  $T$  gives  $T = \bar{T} + T'$ , where  $T'$  is the fluctuation and  $\bar{T}$  is mean temperature, in time. A fast thermistor is designed to measure this temperature fluctuation by changes in its resistance. As a turbulent patch is advected past the thermistor, these fluctuations in time can be mapped on to fluctuations in space using the flow past the sensor, described next. Figure 4.5 shows one hour of measured temperature fluctuations using a  $\chi$ pod and a nearby instrument on the mooring line. The hourly-averaged profile of temperature is also shown, which follows the generic trend. These kind of measurements also provide a source of validation of the measurements by  $\chi$ pods. Temperature fluctuations occur at various timescales and its averaging depends on what physical aspect of the problem one is interested in.

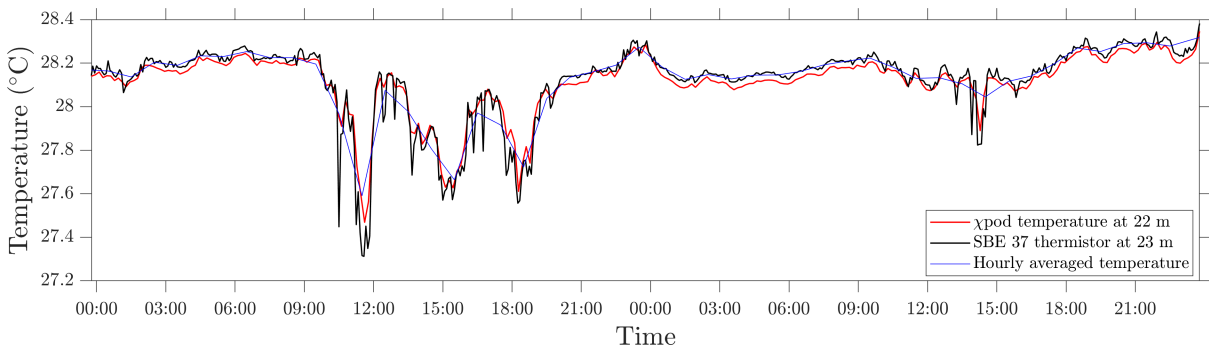


Figure 4.5: Temperature for a randomly-chosen 24-hour period measured by  $\chi$ pod (red line) is shown to match a nearby Sea-Bird electronics (SBE) temperature measuring sensor on the mooring line (black line). The hourly interpolated temperature (in blue) is shown just for reference.

With the measurement of temperature, we can measure the temperature gradient as shown as an example in figure 4.6. The location of four  $\chi$ pods deployed in the Bay of Bengal (Indian Ocean) are also shown (as red dotted lines) which form the basis of all the turbulence analysis in this thesis. Depending on the limitations of the number of instruments, we have to settle at different measures of temperature gradient  $T_z$  as can be seen in figure 4.6 as “a)  $T_z$ ” and “b)  $T_z$ ”. So, the background temperature that the  $\chi$ pods measure see different degrees of  $T_z$  depending on its how we measure this vertical gradient. In this thesis, we use the nearest temperature sensors to measure  $T_z$  such we can have as local a measure of turbulence as possible. This limitation in not having

infinite resolution in the depth is also translated to the measurement of Brunt Väisälä frequency  $N^2$  which also goes into the  $\chi$ pod iterative algorithm.

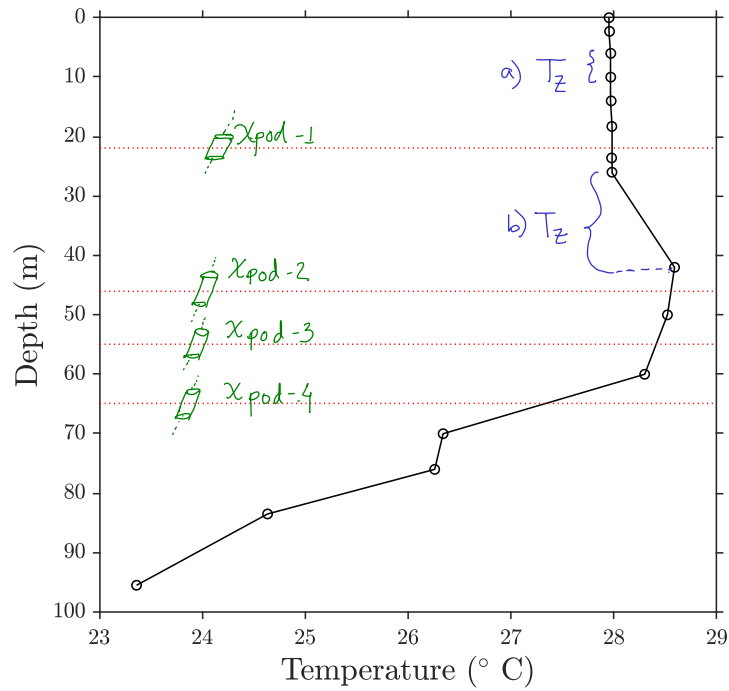


Figure 4.6: A sample temperature gradient from the Bay of Bengal and location of  $\chi$ pods with respect to temperature and salinity measuring instruments (in empty circles). The vertical temperature gradient is  $T_z$ . Locations of  $\chi$ pods are shown.

#### 4.4.2 Speed past thermistor

A Pitot tube in a  $\chi$ pod measures pressure, and from Bernoulli's principle, the speed of flow past the thermistor is determined. The speed of the flow is a the vector sum of the speed of the local currents and also the motion of the  $\chi$ pod due to the movement of the mooring line,

$$u^2 = (u_x - u_{mx})^2 + u_{my}^2 + u_{mz}^2 \quad (4.15)$$

where  $u_x$  is the measured speed in the  $x$ -direction, and  $u_{mx}$ ,  $u_{my}$ , and  $u_{mz}$  are the speeds of the  $\chi$ pod in the three directions. The 50 Hz raw voltage signal from the Pitot tube is combined into 10 min bins and is superimposed with integrated instantaneous motion obtained from the orthogonal accelerometers (Perlin and Moum, 2012).

Figure 4.7 shows the three components of velocity recovered by integrating accelerom-

eter movements in the  $\chi$ pod. As can be seen, the  $\chi$ pod does not stay put in its actual deployment depth but can have some horizontal and vertical movement, which is due to the local currents and surface waves moving the mooring line where the  $\chi$ pod is fixed.

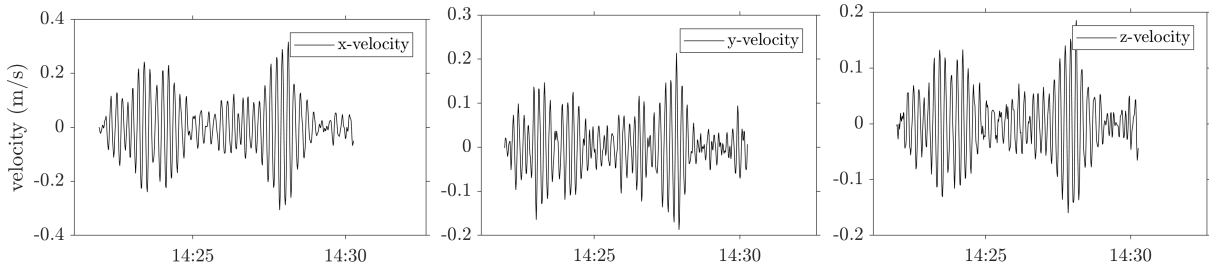


Figure 4.7: One second velocity measurements with Pitot tube on a  $\chi$ pod in (a)  $x$  direction, (b)  $y$  direction, and (c)  $z$  direction shows variations in a small period of about 10 minutes.

The temperature gradient defined in the section 4.4.1 in the temporal space is converted to one dimensional spatial gradient by assuming Taylor’s frozen flow hypothesis (Taylor, 1938), where a linear space-time relation maps the temporal derivative of temperature ( $T_t$ ) to the spatial derivative ( $T_x$ ) using the total local velocity of flow ( $u$ ) as in equation (4.15) as

$$T_x = \frac{1}{u} T_t. \quad (4.16)$$

Surface waves, as well as internal waves, generate motions which complicate the motion of the  $\chi$ pods for effective calculation of the this frozen flow. Due to local reversal of flow and many other factors, the Pitot tube does not respond ideally. We get rid of these data points which gives us unusable velocity data. Also, the flow needs to be sufficient to flush the thermistor fast enough so that the  $\chi$ pod does not sample its own wake. Hence, we get rid of speeds  $< 0.02$  m/s (a small speed value). Pitot tube response is also limited by the sensitive non-linear dependence of the pressure sensor on various external factors like temperature and static pressure. A common mode rejection scheme and an extensive calibration procedure has helped in obtaining robust estimates of speeds from the Pitot tube. A detailed description of the development of a Pitot tube for use in  $\chi$ pods and its sensitivities to various external factors is provided in Moum (2015). Velocity measurements using  $\chi$ pods compare well with other established measurement techniques. Comparison of Pitot tube data on a  $\chi$ pod and the more traditional ADCP is

shown in Moum (2015, Fig 5). Detailed comparisons of turbulence estimates from  $\chi$ pods and more traditional shear microstructure profilers are discussed in Perlin and Moum (2012); Pujiana et al. (2015).

Turbulence as measured by  $\chi$ pods will be used in the next two chapters, where we first show the year-long signal in the geophysical turbulence from the Bay of Bengal and its depth dependence. We also show an interesting phase of suppressed turbulence during and after the summer monsoon months. In the final chapter, we show a diurnal variation in turbulence for about a month and comment on its importance in the Bay of Bengal and its communication with the Indian monsoon system.

# Seasonality and suppression of turbulence

\*\*\*

This chapter is an enlarged version of the publication (reproduced with permission):  
Thakur, R., Shroyer, E. L., Govindarajan, R., Farrar, J. T., Weller, R. A., & Moum, J. N. (2019). Seasonality and buoyancy suppression of turbulence in the Bay of Bengal. *Geophysical Research Letters*, 46(8).

Bay of Bengal in the northern Indian ocean is an important player in the regional climate, specially Indian monsoon. Our year-long (year of 2015) dataset of temperature, salinity, velocity, and turbulence quantifies the upper-ocean turbulent mixing in the northern Bay of Bengal (18N and 89.5E location). The instruments also provide atmospheric data and in conjunction with oceanic measurements provide an estimate of the air-sea interaction in the Bay of Bengal. Above 25 m, we find that (1) mixing is very strong during the summer monsoon (June - September) due to the momentum imparted by strong winds, (2) mixing is reduced from summer monsoon values during the winter monsoon (nominally defined November - January), and (3) mixing is lowest during transition periods between the two. The ocean responds differently below 25 m, a depth that can be regarded as the average ocean mixed layer depth in the Bay of Bengal. The freshwater layer on top of the Bay, arising from river discharge and precipitation in the post-monsoon season, acts as a barrier to the wind-induced mixing and turbulence

is suppressed for several months at the site of our experiment. Below 60 m, even an intense cyclone could not generate appreciable ocean mixing when the freshwater layer was present. Upper ocean turbulence is effectively decoupled from surface forcing by the intense, persistent (multiple months), and shallow salinity-induced stratification associated with this low-salinity water.

## 5.1 Introduction

The Bay of Bengal has one of the lowest-salinity surface waters in the tropical ocean due to numerous rivers discharging into it from the Indian subcontinent (Sengupta et al., 2006) and heavy local seasonal rainfall (Hoyos and Webster, 2007). This low-salinity surface water has a seasonal nature and is highest after the monsoonal precipitation in the summer monsoon months. During the period of this low-salinity water over the Bay, shallow mixed layer depths are observed. This makes the Bay an “active communicator” with the atmosphere (Bhat et al., 2001), i.e., it promptly adjusts itself to change in air-sea interactions, with potential consequence to the Indian monsoon system (Sengupta and Ravichandran, 2001) and cyclonic activities (Balaguru et al., 2014). Due to its potential importance, this portion of the Bay of Bengal has been a site of interesting studies. Sree Lekha et al. (2018) have shown that the salinity changes in the northern Bay are mainly related to the changes in the winds. When winds are high, the shallow Ekman flow pushes the low-salinity water to the interior of the Bay. When winds are low, the mesoscale ( $\mathcal{O}(100\text{km})$ ) eddy field dominates the dispersal of the fresh (low-salinity) water. Studies have also analysed the exit pathways of this low-salinity water from the Bay (Jensen, 2003; Sengupta et al., 2006). However, the role of this low-salinity water in modulating turbulent mixing had not been addressed before.

The upper ocean mixed layer has homogeneous properties like temperature and salinity. Below the mixed layer the temperature decreases with depth (figure 5.1). This is called the thermocline and it has a seasonal nature. Salinity and temperature both contribute to the density of seawater. When there is a stable salinity gradient (i.e., low salinity water above high salinity water), an unstable temperature gradient (i.e., cold water above hot water) can survive (e.g. figure 5.1). It is called an inversion layer. In the Bay as we observe here, salinity often dominates stratification at the base of the

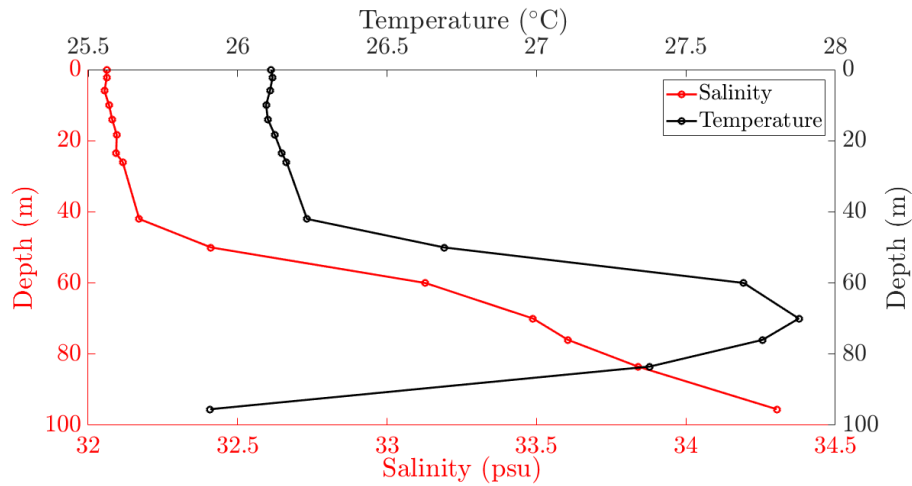


Figure 5.1: A barrier layer and an inversion layer as observed from salinity (red) and temperature (black) at a random time of the day on 19 January 2015 in the Bay of Bengal. The markers denote the location of the temperature and salinity sensors on their respective profiles.

mixed layer, allowing for formation of a “barrier layer” defined as the salinity-stratified region between the base of the mixed layer and the beginning of the thermocline (Godfrey and Lindstrom, 1989). Due to the strong salinity stratification, multiple fine-scale ( $< 10$  m) inversions in temperature are observed and subsurface warm layers can persist (Shroyer et al., 2016). These subsurface warm layers provide an additional reservoir of heat which may influence the sea-surface temperature. Tropical cyclones moving over an ocean draw mass and sustain themselves by evaporation. This cools the ocean surface (Emanuel, 2003). Ocean observations using buoys (D’Asaro, 2003), microwave satellites (Chiang et al., 2011), and shipboard measurements (Leipper, 1967) have reported this ocean cooling by tropical cyclones. A temperature drop as high as  $10.8$  °C has been reported (Chiang et al., 2011) and numerical experiments have studied the mechanisms leading to the ocean surface cooling after a tropical cyclone (Vincent et al., 2012). But tropical cyclones within the Bay have been known to leave a salty wake, which however is not pronounced in its cooling, due to the presence of this subsurface heat supported by the strong salinity gradients (Chaudhuri et al., 2019). Long-term turbulence measurements provide the opportunity to explore the seasonal nature of geophysical turbulence in the Bay. We also describe how turbulent mixing influences the upper-ocean structure within the context of the Bay’s evolving stratification, i.e., the variation in temperature and salinity due to rainfall and riverine discharge and monsoonal wind forcing. High fre-

quency measurements also capture intense bursts of turbulence associated with energetic events like a tropical cyclone.

Moored mixing meters called  $\chi$ pods described in the previous chapter has made it possible to resolve multi-year subsurface turbulence in the Bay. Warner et al. (2016) studied the seasonality in turbulence in the Bay for the first time from a single  $\chi$ pod at 15m depth at 12N and 90E location. This study found that the turbulent heat fluxes were of similar magnitude to the surface flux during the monsoon (stronger wind) periods, whereas it was three orders of magnitude weaker during the transition (weaker wind) periods. In the present study, we examine results from four  $\chi$ pods (at depths ranging from 22 to 65 m) on a heavily-instrumented upper-ocean mooring in the northern Bay (18N). These data capture the development of intense, persistent (multiple months) near-surface stratification and shallow mixed layers associated with the advective arrival of low-salinity water from riverine discharge and rainfall. During this time, salinity contributed 3-5 times the magnitude of temperature to upper-ocean density stratification, supporting the formation of a thin but intense barrier layer as has been shown above. These data provide direct evidence on the role of low-salinity water in controlling the depth of penetration of turbulent mixing in the northern Bay. A remarkable suppression of turbulence below 40 m is seen even during periods of strong winds including during the passing of a cyclone when this low-salinity water existed on the surface.

## 5.2 Data and Methods

Here, we analyse data from a Woods Hole Oceanographic Institution (WHOI) mooring which was deployed in the northernmost international waters of the Bay (18° N, 89.5° E) from 8 December 2014 to 29 January 2016 to record oceanic and atmospheric data. The mooring location is shown in the map in figure 5.2. The deployment of the mooring was a part of a 5-year joint effort between the Indian Ministry of Earth Sciences via the Ocean Mixing and Monsoon (OMM) project and the US Office of Naval Research via the Air-Sea Interactions in the Northern Indian Ocean: Regional Initiative (ASIRI) project. The mooring was provided by Woods Hole Oceanographic Institution and the sensors in the mooring by participating Indian and US institutes. This study of turbulent mixing in the Bay was conducted in collaboration with Oregon State University (Emily L Shroyer

and James N Moum) and Woods Hole Oceanographic Institution (J Thomas Farrar and Robert A Weller). The dataset can be accessed as given in section 5.7.2.

The mooring line had instruments measuring various properties of the water column from the surface of the ocean to  $\sim 1$  km deep into the ocean. A complete description of the full dataset from the different instruments in the mooring is provided in Weller et al. (2019). We present the turbulence estimates in this study. Thirteen Sea-Bird Electronics 37-SM MicroCATs from 2.5-95m logged conductivity (C) and temperature (T) of the water column every 5 minutes. Two of these sensors at 1 m depth below the surface sampled conductivity and temperature every minute, and several also recorded pressure using pressure gauges. We infer salinity and density from conductivity and temperature as given in McDougall and Barker (2011). An upward looking Teledyne RD Instruments 300 kHz acoustic Doppler current profiler (ADCP) was deployed at 80m. Data from a meteorological package (ASIMET (Hosom et al., 1995)) were used to approximate the air-sea fluxes (Fairall et al., 2003) which give a measure of the communication or the coupled nature of the atmosphere-ocean system.

Six  $\chi$  pods were deployed from 22-65m; one was lost at sea, and a second returned data for only half of the deployment. Here, we analyze data from the remaining four  $\chi$  pods deployed at 22, 46, 55, and 65m. Estimates of  $\chi$  are calculated on 1-second intervals, and the turbulent diffusivity for heat (hereafter diffusivity) is calculated as  $K_t = \frac{\chi}{2T_z^2}$  (Osborn and Cox, 1972), using 10-minute averages of  $\chi$  and the mean temperature gradient. The algorithm to estimate  $\chi$  has been described in the previous chapter.  $K_t$  is not evaluated when  $|T_z| < 10^{-3}$  °C/m, or when  $N^2 < 10^{-6}$  s $^{-2}$  to preclude estimates during periods of convection and weak stratification. Based on these criteria, 7.5 percent ( $< 1.5$  percent) of the 1-second  $\chi$  estimates are removed from the 22m  $\chi$  pod (other three  $\chi$  pods at 46, 55, and 65m). A time series of  $\chi$  and  $K_t$  for a the whole year from daily averages is in figure 5.3.

### 5.3 Results from the Bay of Bengal

At the mooring location, the 2015 winter or northeast (NE) monsoon was characterized by negative net surface heat flux that acted to cool the ocean with seasonal-average (NE monsoon) of  $-51.4$  W m $^{-2}$  (daily values peaked at  $-229$  W m $^{-2}$ ; figure 5.4 (a)), occasional

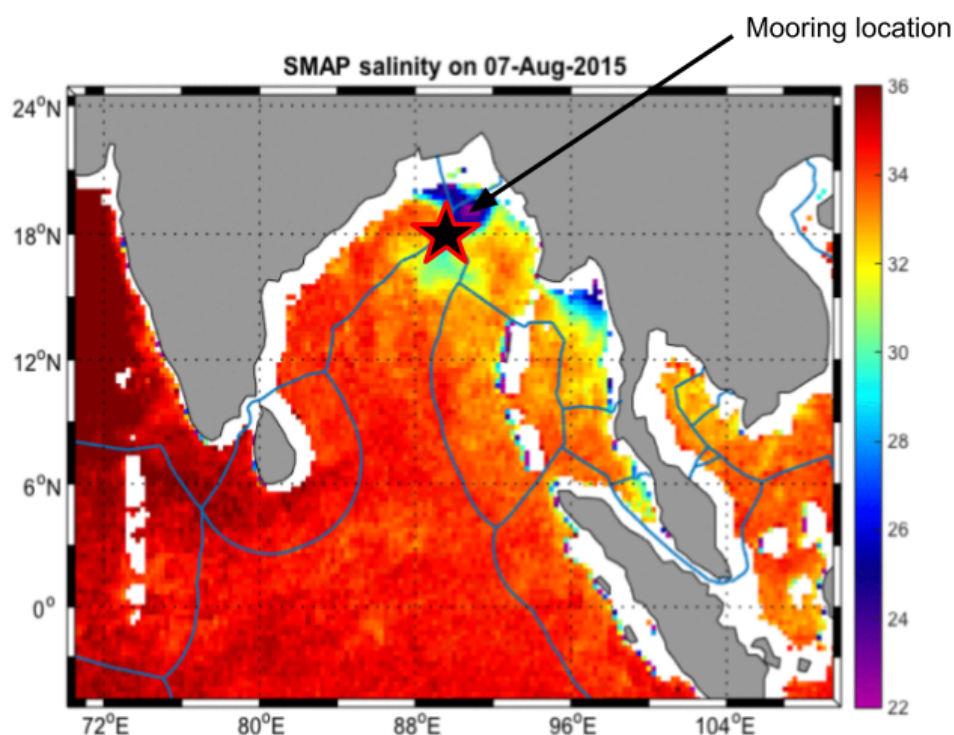


Figure 5.2: A map showing the experimental location with a black star. The colour shows sea-surface salinity (in psu) on 7 August 2015. The land boundaries and the respective Exclusive Economic Zones (EEZs) of the countries are shown. The map is extracted from a movie originally made by Andrew Lucas (Scripps Institution of Oceanography). Used with permission.

precipitation (daily values ranged  $0.2-1.5 \text{ mm hr}^{-1}$ ; figure 5.4 (b)), and strong, persistent winds (daily stress peaked at  $0.2 \text{ N m}^{-2}$ ; figure 5.4 (c)). In contrast, the 2015 winter - summer transition period was characterized by positive net surface heat flux in excess of  $120 \text{ W m}^{-2}$  (peaking at  $170 \text{ W m}^{-2}$ ), negligible precipitation ( $< 0.3 \text{ mm hr}^{-1}$ ), and low wind stress ( $< 0.04 \text{ N m}^{-2}$ ). During this transition, surface air temperature increased from  $24 \text{ }^\circ\text{C}$  in February to  $31 \text{ }^\circ\text{C}$  in June as can be seen in figure 5.5. The increase in air temperature was also followed by the increase in the SST and thus adding buoyancy to the surface. The summer or southwest (SW) monsoon was characterized by fluctuating net surface heat flux and a decrease in surface air temperature to  $28 \text{ }^\circ\text{C}$  by September, persistent and heavy precipitation events ( $> 2 \text{ mm hr}^{-1}$ ), and the strongest observed variability in wind stress, e.g.,  $0.01-0.1 \text{ N m}^{-2}$  during 15-23 May and  $0.04-0.3 \text{ N m}^{-2}$  during 16-21 June. Cyclone *Komen* in late July is identified by its associated negative net surface heat flux and the year's highest precipitation and wind stress. This was the

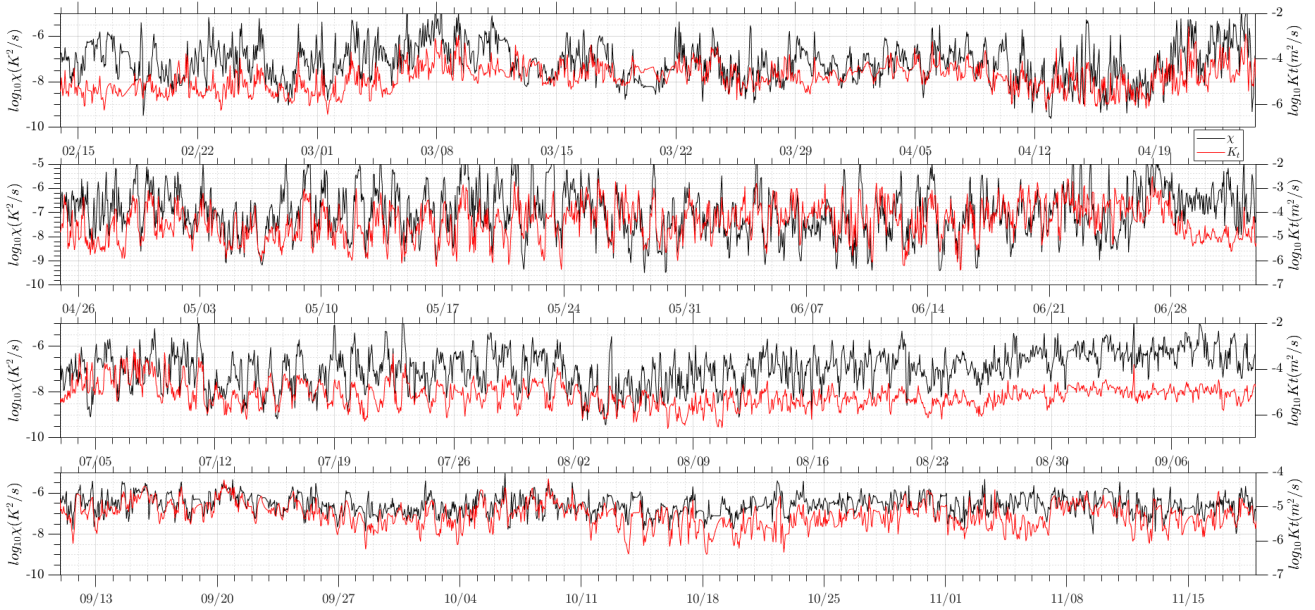


Figure 5.3: Time series of  $\log_{10} K_t$  in red and  $\log_{10} \chi$  in black divided into 2.5 months each in (a-d). Variability of turbulence across seasons is evident.

strongest cyclone in 2015 and, as expected, associated with intense cloud cover.

Figure 5.4 shows the whole monsoon cycle. The various seasons are marked on top of (a). Upper-ocean temperatures (figure 5.4 (d)) increased during the transition to SW monsoon, resulting in increased stratification ( $N^2$ ) over the upper 70 m. In June, they reached maxima after which the upper 25 m cooled by almost  $2.5^\circ\text{C}$  over a one month period in concert with increasing monsoon winds. Large decreases in salinity ( $> 6$  psu; figure 5.4 (e, f)) during the latter half of the SW monsoon mark the arrival of Brahmaputra-Ganga-Meghna discharge with significant contribution from precipitation. The first low-salinity pool arrived on 29 July accompanied by  $\sim 0.5^\circ\text{C}$  drop in SST. The pools of low-salinity water detected in the mooring location is seen in figure 5.4 (f) and figure 5.6. It can be seen that the changes in the upper ocean density structure during the low-salinity pools is majorly contributed by the changes in the upper ocean salinity. The base of the low-salinity pool create intense salinity stratification and can sustain temperature inversions.

Subsequent shallow ( $< 15$  m) and low-salinity ( $< 27$  psu) pools appeared over the SW monsoon persisting for roughly 10 days and characterized by mixed layers (defined by  $|T_{mixedlayer} - \text{SST}| \leq 0.15^\circ\text{C}$ ; figure 5.4 (f)) often less than 10 m deep. Low-salinity features observed later in the year (November and December) show similar shallow mixed

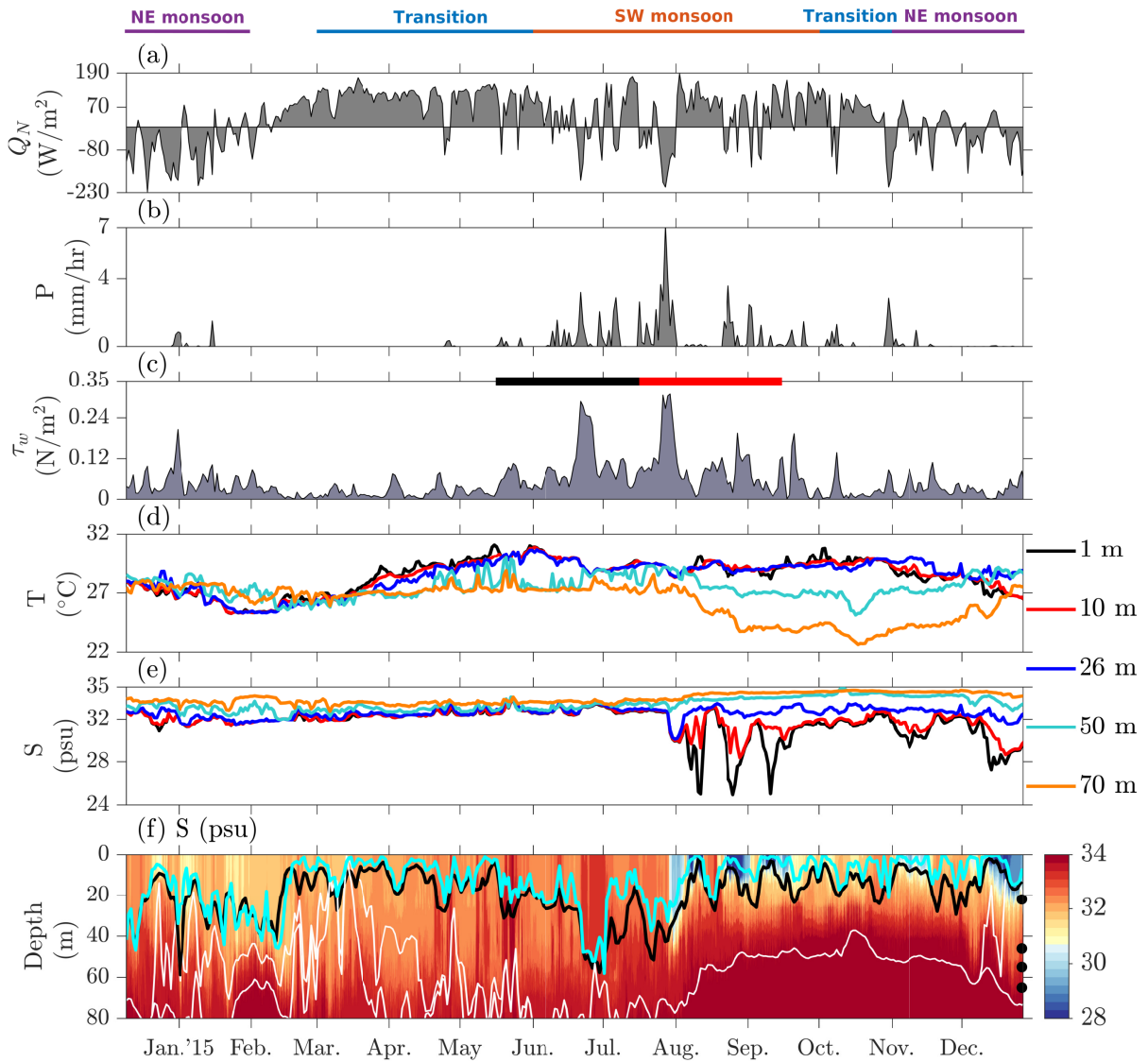


Figure 5.4: Daily-averaged (a) net surface heat flux  $Q_N$  (positive is heat going into the ocean at surface), (b) precipitation  $P$ , (c) wind stress  $\tau_w$  (black and red indicate periods shown in figure 5.7), (d/e) temperature  $T$ /salinity  $S$  at 1 m (SST), 10 m, 26 m, 50 m, and 70 m. (f)  $S$  in color with the temperature-based mixed layer depth (black), density-based mixed layer depth (cyan), 27 °C isotherms (white) overlaid, and  $\chi$ pod deployment depths (black circles). The climatologically-averaged Indian monsoon cycle is indicated above (a).

layer depths with strong stratification at the base of the mixed layer.

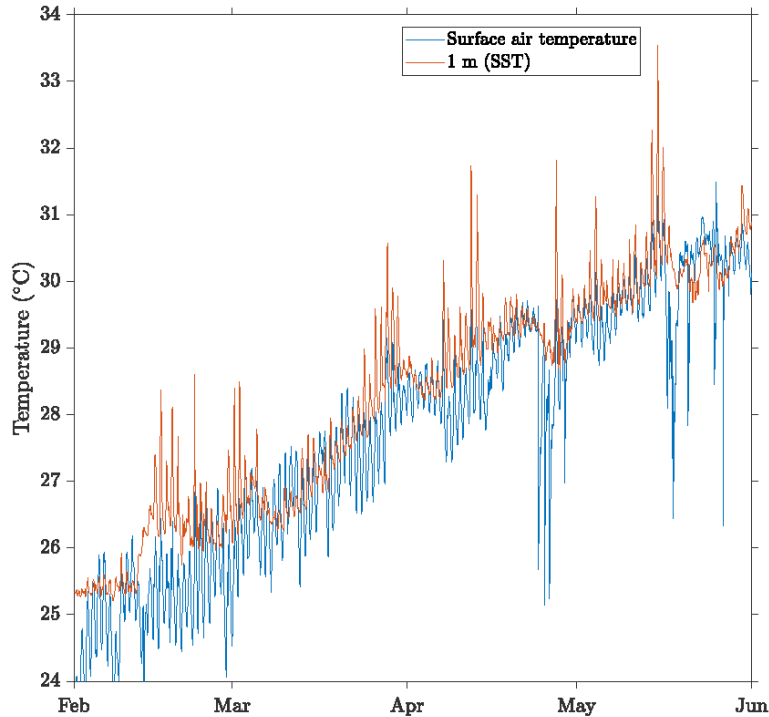


Figure 5.5: The gradual increase in ocean surface-air temperature (blue) and sea surface temperature (red) is seen leading up to the summer monsoon of 2015. The oscillation in both of them is the diurnal signal due to the solar cycle.

## 5.4 Observed Upper-Ocean Turbulence

Interpretation of the turbulence measurements from these four moored  $\chi$  pods requires resolution of the mixed layer depth. The mixed layer was close to the 22 m  $\chi$  pod for a significant portion of the year (figure 5.4 (f)). Responding to wind stress events greater than  $0.24 \text{ N m}^{-2}$  in the SW monsoon, the mixed layer extended below the 46 m  $\chi$  pod for a total of only 13 days. So for the rest of the analysis, we can safely consider the mixed layer to be somewhere around the 22m  $\chi$  pod. The diffusivity indicates variability in turbulence both above and below the mixed layer over a wide range of timescales (figure 5.7). The gray shading in figure 5.7 (a-e) are the one minute raw turbulence estimates at different depths. The  $10^{-4}$  and  $10^{-5}$  lines are plotted to show the difference between the turbulence at the upper 22m  $\chi$  pod and turbulence at deeper  $\chi$  pods. The characteristics of turbulence differed based on whether or not the  $\chi$  pod was near the base of the mixed layer (22m  $\chi$  pod; figure 5.4 (f) and figure 5.7 (b, g)) or below the mixed layer (other three  $\chi$  pods; figure 5.4 (f) and figure 5.7 (c-e, h-j)), as the interplay of surface forcing and

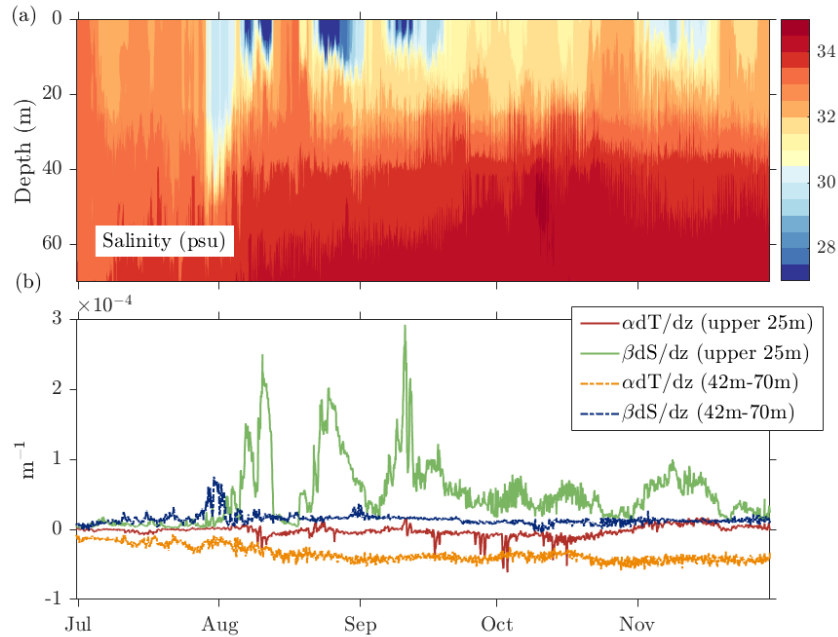


Figure 5.6: (a) Salinity in colour and (b) relative contribution of salinity and temperature to density averaged across various depths assuming a linear equation of state.  $\alpha$  and  $\beta$  are the coefficients of contribution to density for temperature and salinity.

stratification differed within these two environments. One manifestation of this difference is that turbulence at 22m tended to be stronger in magnitude and different in frequency than the sub-mixed layer ( $> 40$  m) turbulence. This was primarily set by surface forcing during the SW monsoon when the median (mean) value of the 22m-diffusivity was one (three) order(s) of magnitude higher than the sub-mixed layer diffusivity. A linear relation between the wind stress and the turbulent diffusivity for the whole year shows that the correlation at 22m is stronger as compared to 46m which is below the mixed layer (figure 5.8). This is consistent with the definition of mixed layer - a layer actively mixed by the winds. Despite strong winds in the summer monsoon months and heavy rainfall creating strong salinity stratification, this trend still holds, and the correlation between the wind stress and turbulence is stronger at 22m when compared to 46m (compare insets of figure 5.8 (a) and (b)).

Intermittency is a strikingly unique feature of turbulence. Multiple definitions of intermittency are possible and can be sometimes defined as where intense fluid motion occurs when the ambient fluid is relatively quiet or the fraction of time the flow is turbulent. These intermittent motions are widely accepted as a candidate for stronger energy

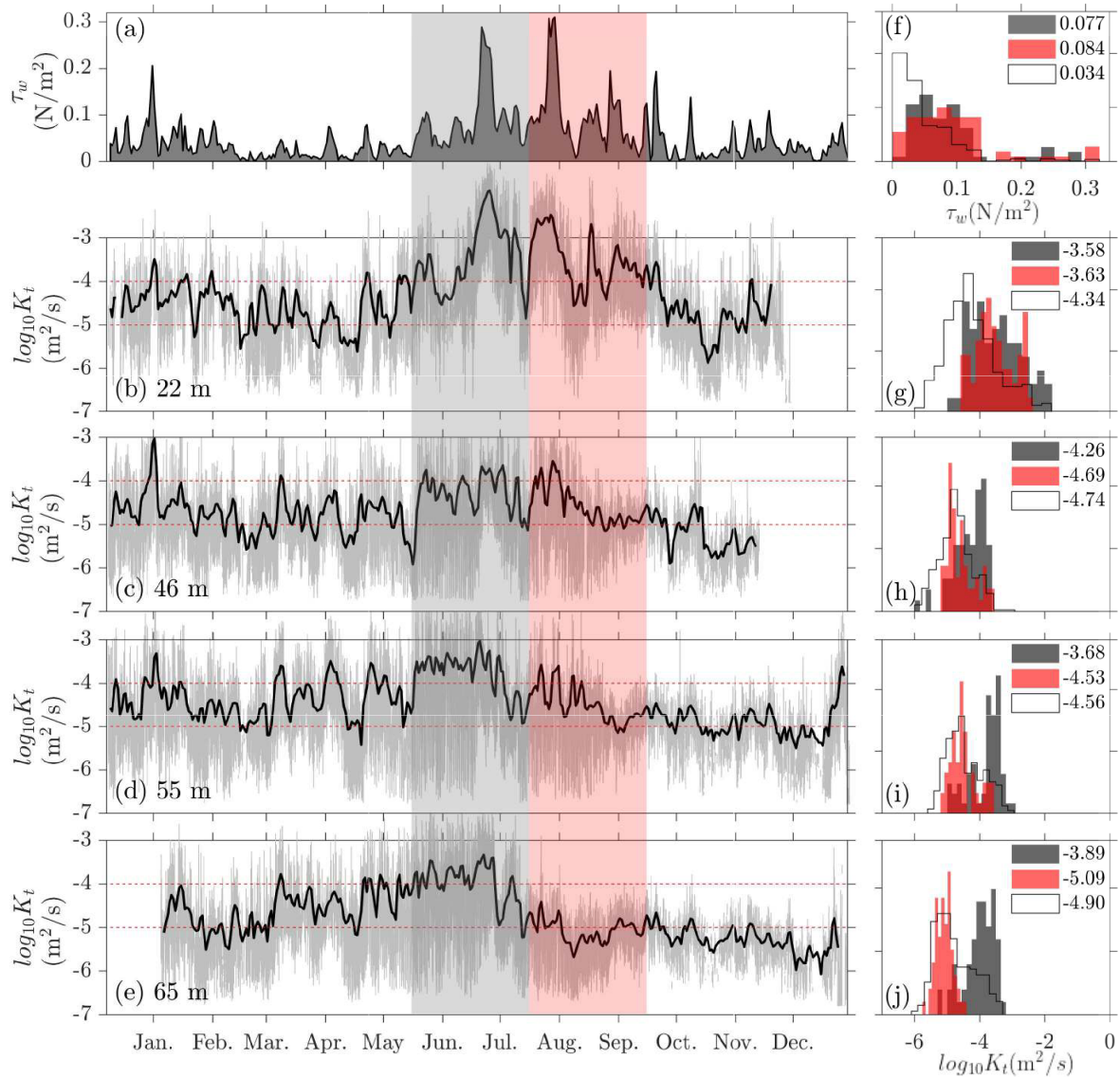


Figure 5.7: (a) Daily-averaged wind stress  $\tau_w$ . Daily-averaged diffusivity  $\log_{10} K_t$  at (b) 22 m, (c) 46 m, (d) 55 m, and (e) 65 m in black, and smoothed one-minute averages in gray. (f) Normalized histograms of daily-averaged  $\tau_w$  for 15 May - 15 July (gray), 15 July - 15 September (red), and the whole year (black outline). (g-j) Normalized histograms of daily-averaged  $\log_{10} K_t$  at same depths as (b-e) and colour coding similar to (a, f). Median values are indicated in (f-j).

transfers during mixing, and reason for intense vortices in atmospheric and oceanic flows. A more quantitative description of this intermittency is the deviation from a Gaussian statistics of some measure of velocity difference between two points and is attributed to strong vortical motions (Batchelor and Townsend, 1949). Intermittency in geophysical turbulence can also be attributed to the natural variability in the forcing agents like winds

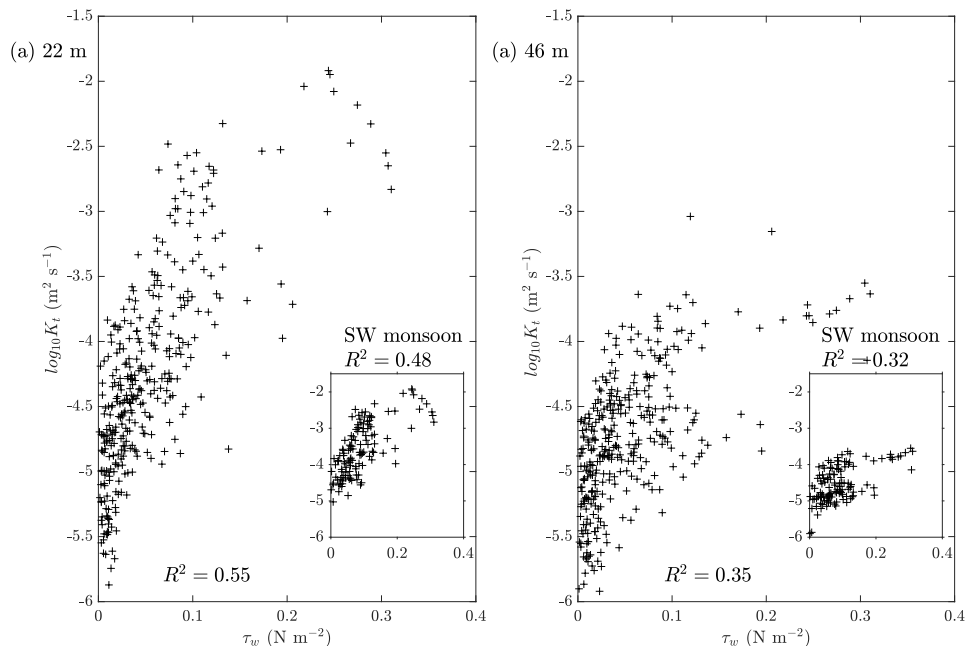


Figure 5.8: Turbulent diffusivity ( $K_t$ ) as a function of wind stress ( $\tau_w$ ) at (a) 22 m and (b) 46 m for the whole year. The inset in each shows the correlation between  $K_t$  and  $\tau_w$  for the summer monsoon months as marked on top of figure 5.4(a).  $R^2$  is the coefficient of determination in the fitted linear models.

and tides and turbulence suppressing agents like stratification, and this is what we will be referring to in this chapter and next. Intermittency can be observed from both the one-minute averages and the hourly averages of turbulent diffusivity in figure 5.7. Although intermittent, variability in turbulence at diurnal, semi-diurnal, and shorter timescales is observed at all depths below the mixed layer, and the correlations as shown in figure 5.8 exists. These turbulence signals were particularly enhanced within the diurnal band during the transition and the SW monsoon (figure 5.11). For example, at 65 m, a persistent ( $\sim$  one month) diurnal signal in diffusivity ranging two orders of magnitude is seen through the majority of July (figure 5.11 (e, g)), coincident with a period of increased subsurface stratification. The diurnal signal in diffusivity is also seen at 46 m and 55 m, but it is not as persistent ( $< 15$  days) as at 65 m. In contrast, the 22 m diffusivity shows a broadband variability at the diurnal timescale (figure 5.11 (e, f)).

The origin of the diurnal cycle in diffusivity is not entirely clear and is a topic of further exploration. A few noteworthy points: (1) the diurnal signal in diffusivity is narrowband (figure 5.9 and 5.11), (2) the internal tide signal (as diagnosed with band-

passed, depth-dependent velocity) has a stronger semi-diurnal component than diurnal, and (3) a strong diurnal signal in temperature stratification ( $T_z$ ) is not seen during this time period (figure 5.9; e.g., as would be anticipated for the development of a diurnal jet (Sutherland et al., 2016)). The periodicity is visualised with wavelet spectrograms (more details on wavelet transforms in section 5.7.1). A weak narrowband diurnal signal is apparent in the east-west wind stress during this time, so a possible interpretation is that the signal is in response to acceleration of the water column by the winds. An alternative theory is that layers of enhanced mixing are vertically advected past depth sensors by the diurnal tide. This explanation depends on the vertical scale of stratification, shear, and mixing layers and their location relative to sensors. Observed patterns in shear, stratification, and Richardson number do not yield conclusive evidence of heaving (figure 5.10) in the month of July. One final possibility is that the diurnal signal is biological in origin, i.e., forced by migrating zooplankton or fish (Pujiana et al., 2015). There is also another diurnal signal with a month-long persistence in the month of May. These interesting diurnal signals in May and July are followed up in the next chapter.

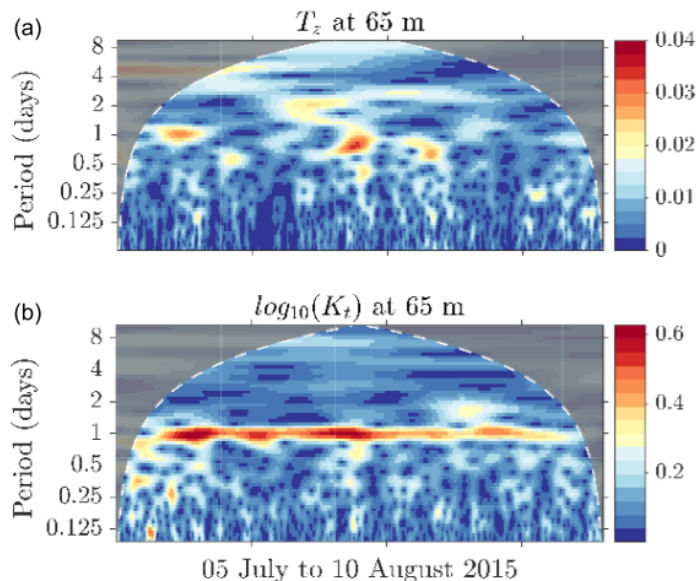


Figure 5.9: Wavelet transforms of (a)  $T_z$  at 65m and (b)  $\log_{10} K_t$  at 65m for the period of 05 July to 10 August. A diurnal signal is seen in  $\log_{10}(K_t)$  which is not seen in the  $T_z$ .

Turbulence also varied at the intraseasonal and seasonal timescales which is arguably the most obvious feature of figure 5.7. For example, the 22 m  $\chi$ pod shows a strong 30-day signal in diffusivity ranging three orders of magnitude during the SW monsoon. We

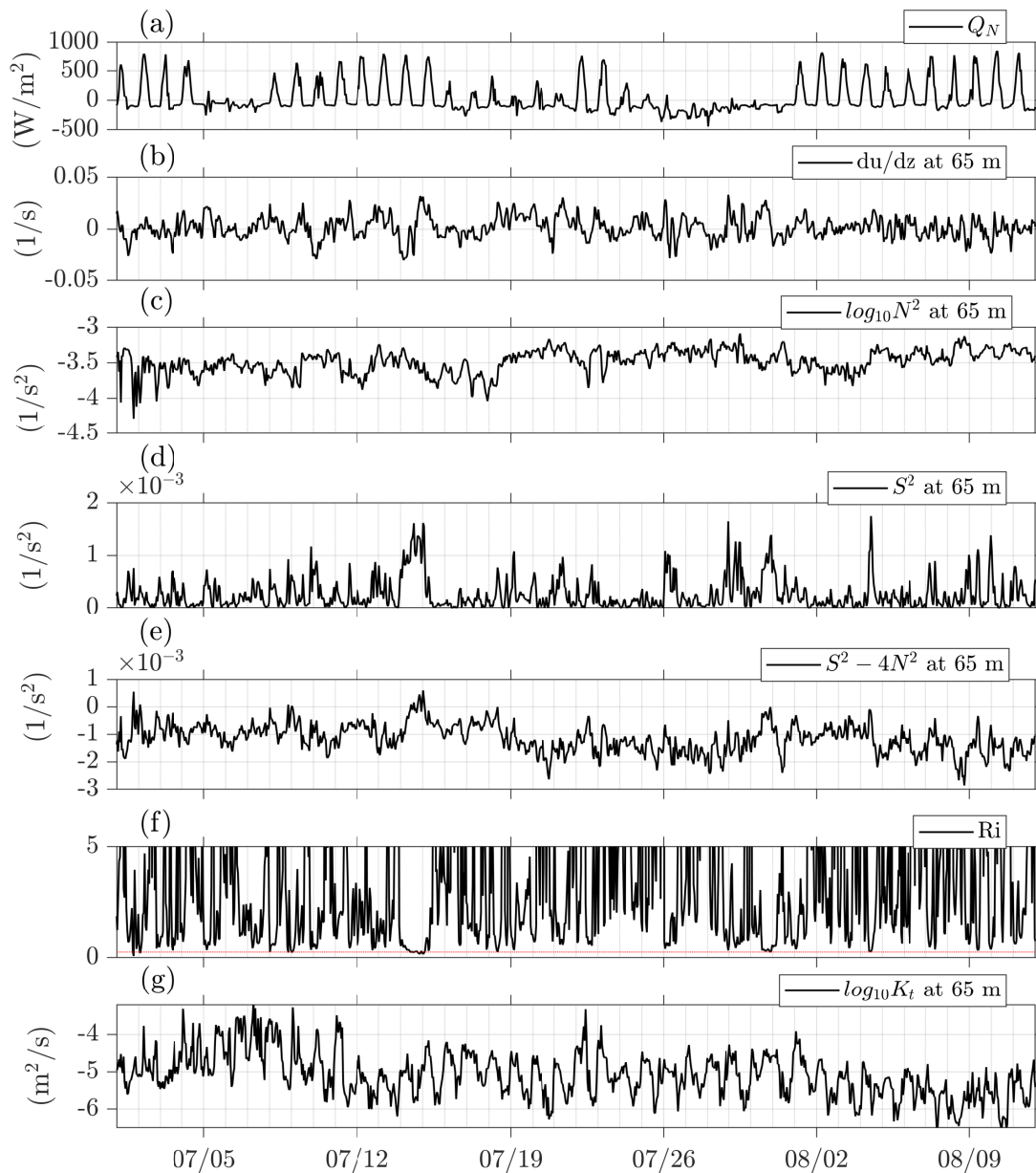


Figure 5.10: Hourly averages of (a) net atmospheric heat flux  $Q_N$ , (b) eastward shear at 65 m (The ADCP bins are 2 m apart in depth ( $z$ )), (c) Brunt-Väisälä frequency  $\log_{10} N^2$ , (d) square of the total shear ( $S^2 = (du/dz)^2 + (dv/dz)^2$ ) at 65 m, (e)  $S^2 - 4N^2$  at 65 m, (f) Richardson number ( $Ri = N^2/S^2$ ) at 65 m (red dotted line is the 1/4 value), and (g) diffusivity  $\log_{10} K_t$  at 65 m.

distinguish two periods of the SW monsoon, 15 May-15 July and 15 July-15 September. These periods were nominally defined by the build-up of the SW monsoon winds (figure 5.4 (c)) and similar wind stress distributions (figure 5.7 (a, f)). Hence, the first period (black rectangle in figure 5.4 (c) and figure 5.7) represents conditions in the SW monsoon before arrival of low-salinity water and the second period (red rectangle in figure 5.4 (c)

and figure 5.7) represents conditions in the SW monsoon after arrival of low-salinity water. Despite having similar wind stress, turbulence is quantitatively different in the two periods for the sub-mixed layer  $\chi$ pods.

### 5.4.1 Seasonality in Turbulence Near the Base of the Mixed Layer

Turbulence at 22m generally followed the strength of the surface winds (figure 5.7 (a, b) and figure 5.8) with the weakest winds and diffusivities observed during the transition and the strongest winds and diffusivity observed in the SW monsoon. The median diffusivity during the transition to the SW monsoon was  $1.5 \times 10^{-5} \text{ m}^2 \text{ s}^{-1}$  which increased to  $2.5 \times 10^{-4} \text{ m}^2 \text{ s}^{-1}$  during the SW monsoon. The highest diffusivity ( $1.1 \times 10^{-2} \text{ m}^2 \text{ s}^{-1}$ ) is observed during the SW monsoon coincident with wind stress in excess of  $0.3 \text{ N m}^{-2}$  (figure 5.11 (b)). These are extremely energetic events in the ocean and turbulent intensity of similar magnitude has been known to exist in isolated intense bursts (Alford et al., 2015; Polzin et al., 1995).

The transition to the NE monsoon was associated with lower values of diffusivity (median  $1.9 \times 10^{-5} \text{ m}^2 \text{ s}^{-1}$ ; mean  $3.8 \times 10^{-5} \text{ m}^2 \text{ s}^{-1}$ ). The distributions of 22 m diffusivity (figure 5.7 (g)) pre- and post-arrival of low-salinity water are very similar (median  $2.5 \times 10^{-4} \text{ m}^2 \text{ s}^{-1}$  versus  $2.4 \times 10^{-4} \text{ m}^2 \text{ s}^{-1}$ ) and an order of magnitude higher than the full-year (median  $4.2 \times 10^{-5} \text{ m}^2 \text{ s}^{-1}$ ). However, diffusivity from mid-September until the end of October was low despite a few high wind stress events.

### 5.4.2 Seasonality in Turbulence Below the Mixed Layer

At the onset of the SW monsoon winds ( $0.01\text{-}0.1 \text{ N m}^{-2}$  during 15-23 May), diffusivity at 46, 55, and 65 m approached that of the 22 m ( $1.8 \times 10^{-4} \text{ m}^2 \text{ s}^{-1}$  on 23 May). (The 46 and 55 m diffusivity increased by roughly an order of magnitude within a few days at this time, while the 65 m diffusivity, already elevated, increased at a slower rate.) Elevated diffusivity below the mixed layer is also seen during other seasons in response to winds, e.g., the peak on 1 January that coincided with a reduction in stratification (figure 5.7 (c, d)). Diffusivity distributions differ significantly from one another with an increasing shift between median values progressing downwards in depth (figure 5.7 (h-j)).

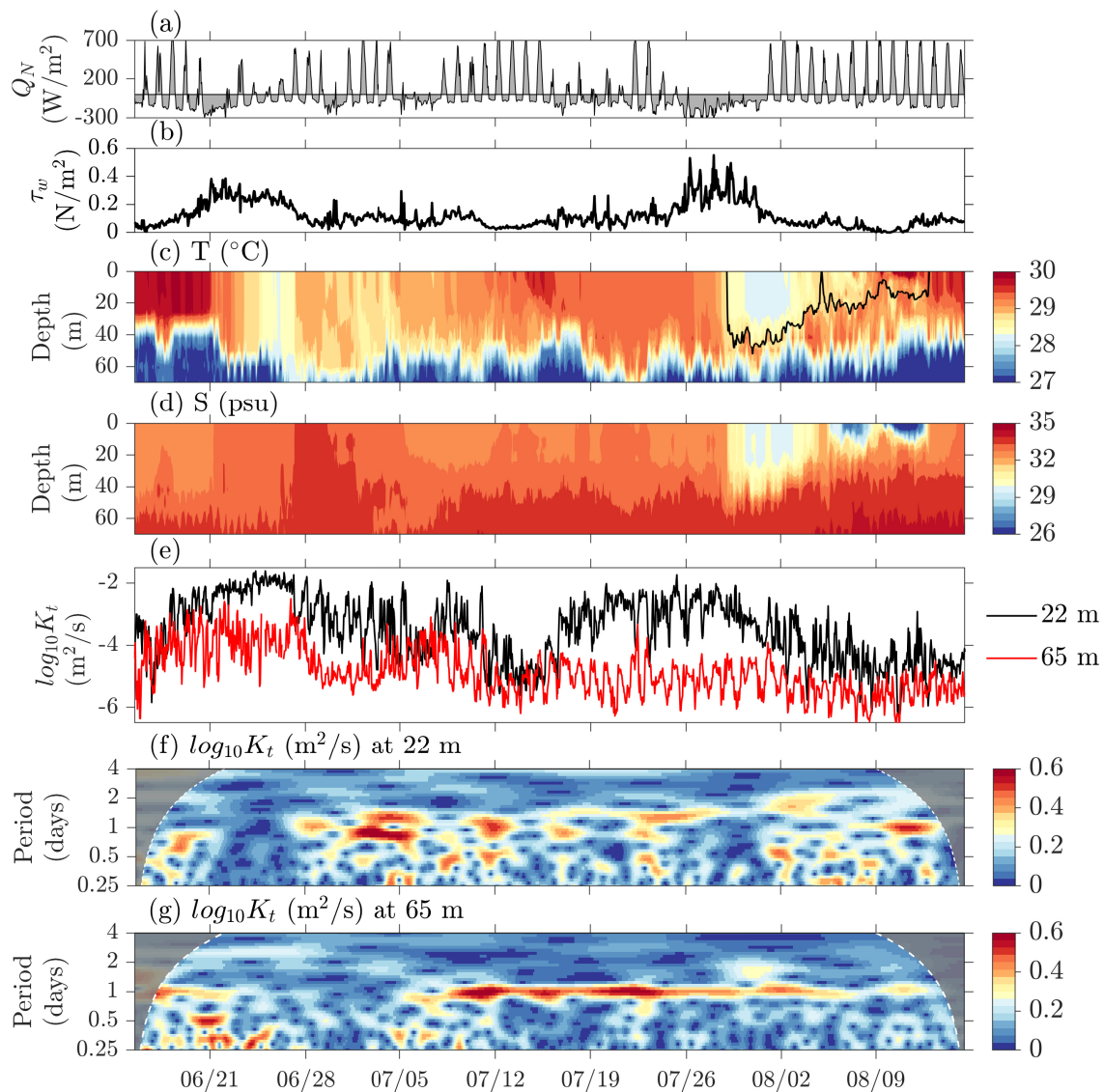


Figure 5.11: Hourly-averaged (a) net surface heat flux  $Q_N$ , (b) wind stress  $\tau_w$ , (c) temperature  $T$  (black line is the 32 psu iso-salinity contour), (d) salinity  $S$ , and (e) diffusivity  $\log_{10} K_t$  at 22 m and 65 m. Wavelet transforms of  $\log_{10} K_t$  at (f) 22 m and (g) 65 m.

The most pronounced trend in turbulence below the mixed layer is the steady decline in the intensity and variance of diffusivity observed during the latter half of the SW monsoon and into the NE monsoon season (figure 5.7 (c-e)), despite strong winds. After this decline, daily median and mean values of diffusivity remained low ( $10^{-5}$ - $10^{-6} \text{ m}^2 \text{ s}^{-1}$ ) for 3-5 months.

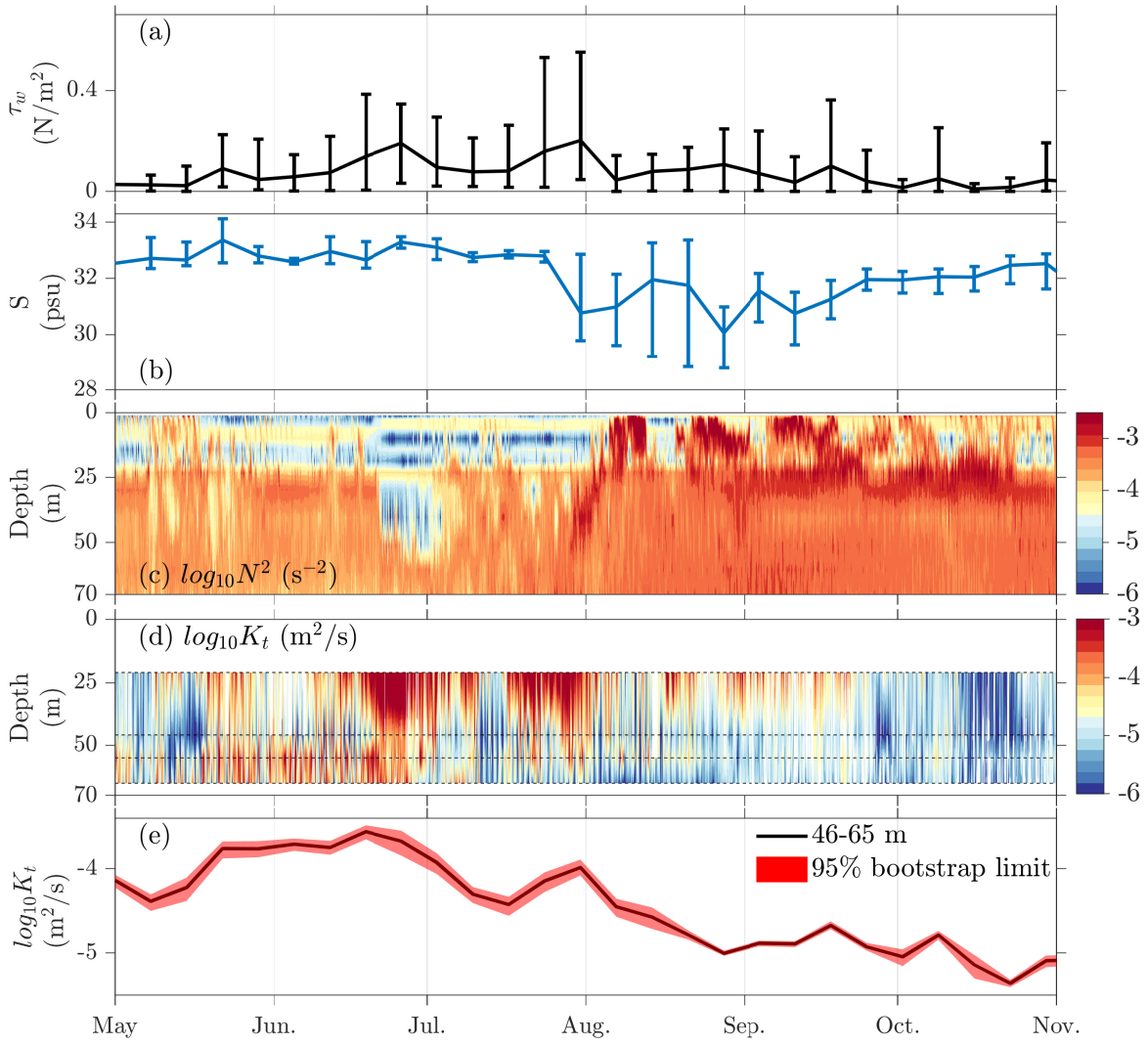


Figure 5.12: Weekly-averaged (a) wind stress  $\tau_w$  and (b) upper 30 m salinity  $S$ , with error bars of maximum and minimum  $\tau_w$  and  $S$  within each week (from hourly averages) respectively. Hourly-averaged (c) Brunt-Väisälä frequency  $\log_{10} N^2$  and (d) diffusivity  $\log_{10} K_t$  interpolated linearly between 22 m, 46 m, 55 m, and 65 m  $\chi$ pods (black dotted lines). (e) Weekly-averaged 46-65 m  $\log_{10} K_t$  with the 95 percent bootstrap limit.

## 5.5 Buoyancy Suppression of Turbulence

The low-salinity water was detected in the mooring in distinct pulses starting late-July and continuing into the early NE monsoon (figure 5.4 (f)); the first occurrence is a set of three pools over two weeks (figure 5.11 (d)). The first pool, occurring on 29 July, was  $\sim 40$  m deep and the next two pools on 05 and 09 August were relatively shallow ( $\sim 20$  m).

The first caused an increase in stratification below 25 m while the following two caused increased stratification above 25 m (in both cases  $N^2 \sim 10^{-3} \text{ s}^{-2}$ ; figure 5.12 (c)). (Note that during the arrival of these freshwater pools the near-surface salinity stratification accounted for a majority of the total change in upper-ocean stratification. Both near-surface low-salinity water and the compression of iso-density (isopycnal) contours at depth contributed significantly to the stratification.

The response of diffusivity to the increase in stratification associated with arrival of low-salinity water must be interpreted with consideration of surface forcing, especially with regard to the strong storms occurring in June and July (wind stress  $> 0.3 \text{ N m}^{-2}$ ). The decrease in winds on 28 June and 12 July coincided with reduced diffusivities at all depths (figure 5.7 and figure 5.11 (b, e)).

The reduction in diffusivity over this time span varied from 1.5-3 orders of magnitude in hourly averages for the different  $\chi$  pods (figure 5.12 (d)). As compared to the late-June storm, the increase in diffusivity during *Komen* was less in magnitude and restricted only to shallower depths (figure 5.12 (d, e)). The signal of *Komen* is not at all obvious at 65 m (figure 5.11 (e)). This is despite stronger wind stress during *Komen* (*Komen's* storm center passed within  $\sim 350 \text{ km}$  of the mooring on 29 July.). High wind stress events occurred during August and September, but diffusivities (and their daily ranges) below the mixed layer remained low (figure 5.7 and figure 5.12 (d, e)). After *Komen*, extreme turbulence events (1-minute data; figure 5.7) rarely exceeded  $10^{-4} \text{ m}^2 \text{ s}^{-1}$  below 45 m. Over this time period, the daily mean diffusivity at 65 m was  $\lesssim 10^{-5} \text{ m}^2 \text{ s}^{-1}$ . Closer to the surface (22 m), it ranged between  $10^{-3} \text{ m}^2 \text{ s}^{-1}$  and  $10^{-6} \text{ m}^2 \text{ s}^{-1}$ .

Weekly averages of wind, salinity, and sub-mixed layer diffusivity reflect the relative correlations between forcing, stratification, and turbulence at this timescale. Weekly-averaged sub-mixed layer diffusivity mimics the weekly averaged surface-salinity rather than the wind stress, in that the presence of low-salinity water ( $S < 32 \text{ psu}$ ; figure 5.12 (b)) is associated with reduced diffusivity (figure 5.12 (e)) but variable wind forcing (figure 5.12 (a)).

## 5.6 Conclusions

The upper-ocean turbulent response of the northern Bay is notable in several ways. First, semi-diurnal to near-inertial variability in turbulence shows intermittency throughout the year with periods of enhanced turbulence often spanning one week to one month. The differences and variability at distinct depths (22, 46, 55, and 65 m) are a reflection of the small vertical scale in the stratification (figure 5.12 (c)), which is often of the order of 10 m or less. Furthermore, as layers heave past the  $\chi$  pods, signals that persist on individual layers will be interpreted as time variability at that depth.

Second, turbulence within and near the base of the mixed layer (22 m) shows a strong seasonality that varies with monsoon winds, similar to results found by Warner et al. (2016) at 12N. Turbulent diffusivity was strongest ( $> 10^{-3} \text{ m}^2 \text{ s}^{-1}$ ) in the SW monsoon with the two strongest storms of the year. In contrast to Warner et al. (2016), diffusivity during the NE monsoon of 2015 was weaker than during the SW monsoon at 18N. During times of weak winds, often during transition periods, the daily averaged diffusivity occasionally dropped below  $10^{-5} \text{ m}^2 \text{ s}^{-1}$ .

Third, turbulence beneath the mixed layer (46-65 m) was suppressed in the second half of the SW monsoon during the period of arrival of low-salinity water from riverine-discharge and precipitation (figure 5.12 (b, e)), coincident increase in near-surface salinity stratification (initial response), and also elevated sub-surface temperature stratification (boreal fall). A noteworthy example of this suppression is the lack of turbulent response in the 65 m  $\chi$  pod when cyclone *Komen* transited the northern Bay (figure 5.11 (e)). Following *Komen*, turbulence remained suppressed below the mixed layer for three to five months (figure 5.12 (e)). Turbulence at 55 m recovered to its original strength by the end of the year.

For 18N, the high near-surface stratification contributed significantly to limiting vertical turbulent “communication” within the water column for multiple months, isolating subsurface heat reservoirs with consequences to upper-ocean heat and salt content and air-sea interactions. This suppression of turbulence will also limit storage of surface fluxes at depth and must contribute towards the longevity of the low-salinity surface layer.

Turbulence suppression (Narasimha and Sreenivasan, 1979) or destabilisation of turbulent flows (Kühnen et al., 2018) has also been of interest with regard to fundamental

fluid stability. Studies on suppression or ‘relaminarization’ of turbulence in simple flows reviewed by Narasimha and Sreenivasan (1979) indicates that this suppression could be due to dissipation by viscosity, conversion of turbulent kinetic energy to other forms of energy (Narasimha, 1983), or reduction in turbulent transport by changing the geometry or other features of the flow. This observation of turbulence suppression in the Bay provides an opportunity to understand this fundamental transition question and the effect of stratification, and the numerical tools developed in the earlier chapters could prove to be helpful.

## 5.7 Appendix

### 5.7.1 Wavelet Transforms

When wavelet transforms are referred to in this thesis, we mean the continuous one-dimensional wavelet transform of a signal using one of the many available analytic wavelets (Lilly and Olhede, 2010). These analytic wavelets are wavelike oscillatory functions localized both in time and frequency. These functions are rapidly decaying in time and have a zero mean. Wavelet transforms allow us to analyze oscillatory signals ( $f(t)$ ) by extracting the amplitude of convolutions with analytic wavelets. The analytic wavelets used in our study are the generalized Morse wavelets (Lilly and Olhede, 2012). A certain benefit of using wavelet transforms for our study is that it gives us time dependence of the frequency in the signal as can be seen in figure 5.13. We have a signal of the form  $\sin(2\pi * 10t) + \sin(2\pi * 30t)$  in time ( $t$ ). A Fourier transform of the time series gives information about the frequencies present in the signal as can be seen by comparing panels (a) and (b) of figure 5.13. Panel (b) shows two peaks at 10 and 30 Hz. It says nothing about when the signal with frequency 10 Hz ended and when the signal with frequency 30 Hz begins. That can, however, be obtained with a wavelet transform which shows (panel (c)) that the signal with frequency 10 Hz ends at  $t \sim 7.5$  and the 30 Hz starts at that point as can also be confirmed from the line plot in panel (a). The colour is the magnitude of energy in the particular frequency. This information from wavelet spectrograms helps with added understanding of a particular signal and has been applied to oceanographic data in this thesis.

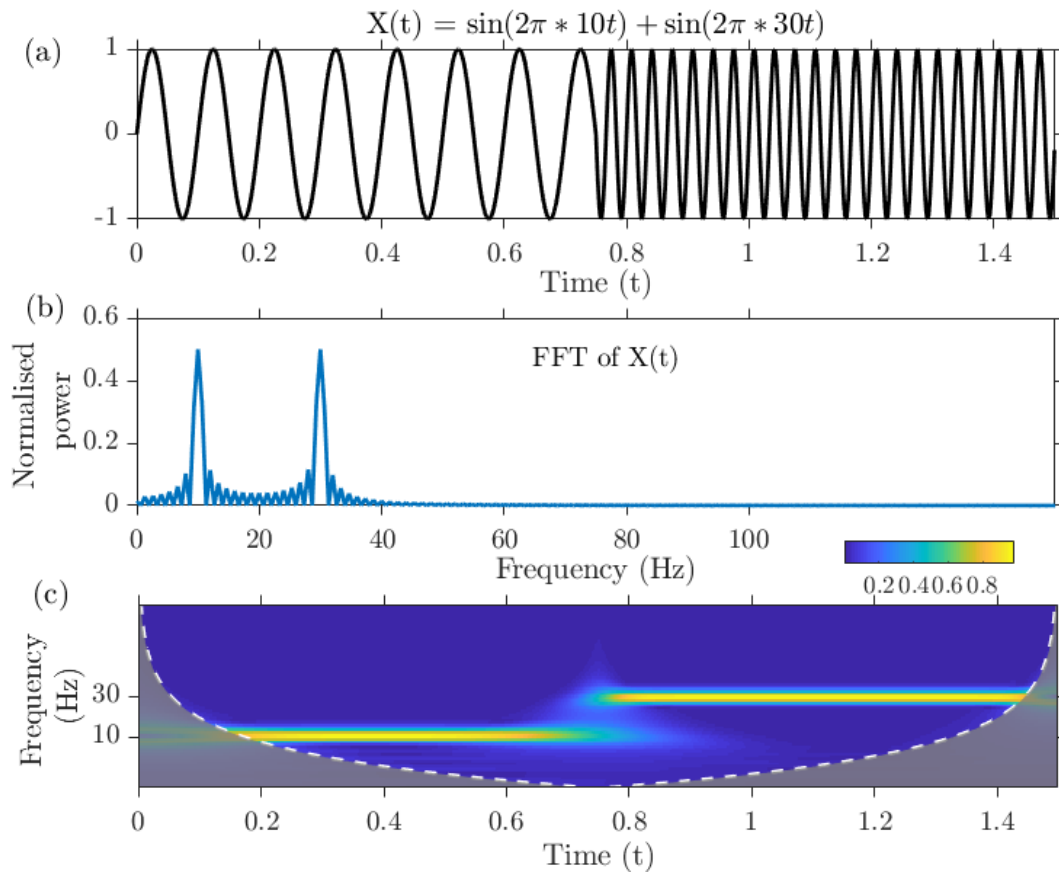


Figure 5.13: An example of using wavelet analysis on a simple sinusoidal signal with two different frequencies. (a) A signal of two frequencies (10 Hz and 30 Hz). (b) A Fourier transform of the signal only gives us two peaks at the frequencies of the signal. (c) A wavelet transform gives information about the frequencies in the signal and their time dependence.

### 5.7.2 Accessing the dataset

WHOI surface meteorology and air-sea flux data are available in

<http://uop.whoi.edu/projects/Bengal/>. Upper-ocean temperature, salinity, and turbu-

lence data measured using  $\chi$  pods are available in <https://doi.org/10.6084/m9.figshare.7416440>.

# Conclusions

\*\*\*

*Every end is the beginning of something.*

This thesis has presented two different kinds of work: (a) nonlinear nonmodal fluid stability and the importance of viscosity stratification and (b) observations of geophysical turbulence in the Bay of Bengal. The connection between the two is not immediately apparent, but ideas from one part of the work have served as inspiration for the other part and can serve as future work directions. Nonmodal stability analysis itself is a broad area of research, and we deliberately chose a simple channel flow as our model study rather than working with a real-life complicated system like ocean turbulence. The understanding and the abilities that have been developed via work in this thesis shall be soon extended to study more ocean-like flows. Observations relevant to the ocean and atmosphere that are currently not understood can ignite further fundamental questions of fluid stability and the tools of nonlinear stability could prove to be useful.

We have first developed a theory of nonlinear nonmodal analysis for viscosity-stratified flows. The adjoint viscosity-stratified Navier-Stokes and the adjoint viscosity-stratified scalar equations have been derived in this thesis for the first time to our knowledge. We have developed, from scratch, a fluid flow solver which can simulate stratified flows in a three-dimensional channel (plane Poiseuille flow) and is a strong multi-purpose numerical tool. We have also developed a nonlinear optimisation tool for viscosity-stratified nonlinear optimisation which is only a slight modification of already existing techniques, but includes the effects of varying viscosity. Using this tool, we have studied the effects of viscosity variations as a simple function of temperature in a channel flow. We calculate the

linear and nonlinear optimal perturbations, which cause the highest perturbation energy for fixed initial energy and fixed target time of optimisation. If the times of optimisation were larger than those presented here, these optimal perturbations could represent, or be related to, those that cause the lowest Reynolds number transition to turbulence. We find that these optimal perturbations are sensitive to the various parameters of the flow like Reynolds number, time of optimisation, temperature difference across the channel walls etc. We find that the singular effects of viscosity stratification result in unique localisation of linear and nonlinear optimal perturbations on the hotter or the less viscous wall. We find that the linear and the nonlinear optimal perturbations differ in shape and also the degree of localisation varies. The nonlinear optimal tends to efficiently use the lift-up mechanism to transiently grow in energy. This mechanism is totally absent in the linear optimal, where disturbance growth is displayed by the fast-acting Orr mechanism. In case of the nonlinear optimal, a shift of the dynamics from the hot to the cold wall, and a strengthening and persistence of the inflectional profile at that wall are seen, and this, we expect, will prove relevant to how the transition to turbulence differs in a viscosity-varying flow from that in the constant viscosity flow. We provide a physical description of this process. We thus demonstrate the power of the nonlinear optimisation technique in tracking the complete physics in such problems and note its importance in transition to turbulence. Given that it is a relatively new technique, we hope that this thesis will ignite interest in understanding viscosity-varying and other flows in this context. We plan to extend this work to understand our observations in the Bay of Bengal, where the turbulent eddy viscosity has been seen to be a strong function of depth and time.

In the second half of the thesis, we have presented a year-long dataset of turbulence in the Bay of Bengal as measured by  $\chi$ pods. We have presented a detailed analysis of the turbulence signals and have commented on its importance for the Indian monsoon. This work was done as a project of the ASIRI-OMM program to better understand the Bay of Bengal and its impact on the Indian monsoon. We show that there is a seasonality to turbulence in the Bay and as earlier thought, turbulence is not limited to the upper 20m of the ocean but it can penetrate as deep as 65m of the ocean. This presents an interesting area of study of the amount of heat exchange between the upper ocean and the deeper thermocline in the Bay, an open question even for the whole of the world's oceans. The depth-dependence of turbulence in the Bay is surprising in the sense that even a

cyclone could not generate appreciable mixing below 60m of depth as opposed to the oceans where much deeper mixing have been observed. This points to the importance of the near-surface freshwater-induced salinity stratification in capping the transfer of momentum from the surface to deeper depths. A suppressed phase of turbulence has been observed where the Bay below the mixed layer remains quiescent for 3-5 months which is visibly correlated to the existence of strong salinity gradients in the upper ocean. This suppression of turbulence is of interest in fundamental fluid transition and will be taken up for study using the numerical tools that we have developed. We have also shown a low-intensity diurnal signal of turbulence in the Bay which could also act as an important source of mixing of heat during the suppressed phase of turbulence. We could not, however, reproduce this diurnal signal using a numerical model but we strongly suspect that this signal is related to the diurnally periodic winds which is a huge land-sea breeze extending to more than 400km into the interior of the ocean. The presence of land boundaries on three sides of the Bay could play an important role in sustaining this month-long land-sea breeze and the diurnal turbulence in the summer monsoon months.

## 7.1 Future directions

When we look around us, we realise that shear flow in combination with viscosity variation is very common. Understanding the transition to turbulence in these flows is a big question, and the first part of this thesis could provide the first stepping-stone to a number of problems that could have both academic interest and industrial usefulness. For example, viscous flow through pipelines still presents a challenge to oil-drilling industries. If using the technique of nonlinear adjoint optimisation, the loss of pumping energy to viscous losses or turbulence could be minimised, this presents an economical advantage. Another study which could have potential is that of the effect of boundary conditions, specifically periodic heating and cooling, on the transient growth mechanisms and the transition to turbulence. Because we have used a small subcritical Reynolds number, the flow did not transition to turbulence and the mechanisms presented in this thesis could be investigated with higher Reynolds numbers. We could study Couette flow instead of channel flow, which has a simpler shear profile, to understand the effect and interaction of viscosity with a different shear profile. The Couette flow system is unique in the sense

that it goes to turbulence despite being linearly stable at any Reynolds number, i.e., all perturbation eigenmodes, taken individually, decay exponentially. We have only studied a certain viscosity-stratification model and an extension of the present numerical methods to a different viscosity model is not a difficult task.

The second part of this thesis could ignite some further studies like investigations into the spatial dependence of turbulent mixing in the Bay of Bengal. The Bay is an important influence in the Indian monsoon system and a better understanding could only improve the forecast abilities of the monsoon. An interesting signal that has been observed is the buoyancy suppression of turbulence which will be definitely followed up as it needs much more understanding, both theoretically and also its practical implication in the heat exchange between the atmosphere and the deeper ocean. This suppression of turbulence could also be further investigated using tools of nonlinear simulations and stability. Another interesting question of study is the vertically propagating internal wave signal which could be investigated with regards to the Bay to understand the transfer of wind-imparted energy to the deeper ocean and where and how it causes mixing. As mentioned earlier, in the ocean, it is the eddy viscosity, and not the molecular viscosity, whose variation in space and time is of importance. Given that the eddy viscosity is a construct, new stability methods will need to be devised to study this case.

# Bibliography

\*\*\*

- (2020). European Centre for Medium-Range Weather Forecasts. <https://www.ecmwf.int/en/forecasts/datasets/reanalysis-datasets/era5>.
- Abergel, F. and Temam, R. (1990). On some control problems in fluid mechanics. *Theoretical and Computational Fluid Dynamics*, 1(6):303–325.
- Alford, M. H. (2003). Redistribution of energy available for ocean mixing by long-range propagation of internal waves. *Nature*, 423(6936):159–162.
- Alford, M. H., Cronin, M. F., and Klymak, J. M. (2012). Annual cycle and depth penetration of wind-generated near-inertial internal waves at ocean station Papa in the northeast Pacific. *Journal of Physical Oceanography*, 42(6):889–909.
- Alford, M. H., Peacock, T., MacKinnon, J. A., Nash, J. D., Buijsman, M. C., Centurioni, L. R., Chao, S.-Y., Chang, M.-H., Farmer, D. M., Fringer, O. B., et al. (2015). The formation and fate of internal waves in the South China Sea. *Nature*, 521(7550):65–69.
- Arratia, C., Caulfield, C., and Chomaz, J.-M. (2013). Transient perturbation growth in time-dependent mixing layers. *Journal of Fluid Mechanics*, 717:90–133.
- Balaguru, K., Taraphdar, S., Leung, L. R., and Foltz, G. R. (2014). Increase in the intensity of postmonsoon Bay of Bengal tropical cyclones. *Geophysical Research Letters*, 41(10):3594–3601.
- Barkley, D. (2016). Theoretical perspective on the route to turbulence in a pipe. *J. Fluid Mech*, 803(1).
- Barkley, D. and Tuckerman, L. S. (2005). Computational study of turbulent laminar patterns in Couette flow. *Physical Review Letters*, 94(1):014502.
- Batchelor, G. (1959). Small-scale variation of convected quantities like temperature in

- turbulent fluid Part 1. General discussion and the case of small conductivity. *Journal of Fluid Mechanics*, 5(1):113–133.
- Batchelor, G. K. and Townsend, A. A. (1949). The nature of turbulent motion at large wave-numbers. *Proceedings of the Royal Society of London. Series A. Mathematical and Physical Sciences*, 199(1057):238–255.
- Beal, L., Vialard, J., Roxy, M., Li, J., Andres, M., Annamalai, H., Feng, M., Han, W., Hood, R., Lee, T., et al. (2020). A roadmap to IndOOS-2: Better observations of the rapidly-warming Indian Ocean. *Bulletin of the American Meteorological Society*.
- Becherer, J. and Moum, J. N. (2017). An efficient scheme for onboard reduction of moored  $\chi$ pod data. *Journal of Atmospheric and Oceanic Technology*, 34(11):2533–2546.
- Bewley, T. R. (2012). *Numerical Renaissance: simulation, optimization, & control*. Renaissance Press.
- Bewley, T. R., Temam, R., and Ziane, M. (2000). A general framework for robust control in fluid mechanics. *Physica D: Nonlinear Phenomena*, 138(3-4):360–392.
- Bhat, G., Gadgil, S., Kumar, P. H., Kalsi, S., Madhusoodanan, P., Murty, V., Prasada Rao, C., Babu, V. R., Rao, L., Rao, R., et al. (2001). Bobmex: The Bay of Bengal monsoon experiment. *Bulletin of the American Meteorological Society*, 82(10):2217–2243.
- Böberg, L. and Brosa, U. (1988). Onset of turbulence in a pipe. *Zeitschrift für Naturforschung A*, 43(8-9):697–726.
- Bogucki, D., Domaradzki, J. A., and Yeung, P. (1997). Direct numerical simulations of passive scalars with  $Pr > 1$  advected by turbulent flow. *Journal of Fluid Mechanics*, 343:111–130.
- Bouffard, D. and Wüest, A. (2019). Convection in lakes. *Annual Review of Fluid Mechanics*, 51:189–215.
- Bowden, K. (1965). Horizontal mixing in the sea due to a shearing current. *Journal of Fluid Mechanics*, 21(1):83–95.
- Brandt, L. (2014). The lift-up effect: the linear mechanism behind transition and turbulence in shear flows. *European Journal of Mechanics-B/Fluids*, 47:80–96.
- Brandt, L. and Henningson, D. S. (2001). Transition of streamwise streaks in zero pressure gradient boundary layers. In *Second Symposium on Turbulence and Shear Flow*

*Phenomena*. Begel House Inc.

- Butler, K. M. and Farrell, B. F. (1992). Three-dimensional optimal perturbations in viscous shear flow. *Physics of Fluids A: Fluid Dynamics*, 4(8):1637–1650.
- Canuto, C., Hussaini, M. Y., Quarteroni, A., and Zang, T. A. (2007). *Spectral methods: fundamentals in single domains*. Springer Science & Business Media.
- Capet, X., McWilliams, J. C., Molemaker, M. J., and Shchepetkin, A. (2008). Mesoscale to submesoscale transition in the California Current System. Part I: Flow structure, eddy flux, and observational tests. *Journal of Physical Oceanography*, 38(1):29–43.
- Case, K. (1960). Stability of inviscid plane Couette flow. *The Physics of Fluids*, 3(2):143–148.
- Chaudhuri, D., Sengupta, D., D’Asaro, E., Venkatesan, R., and Ravichandran, M. (2019). Response of the salinity-stratified bay of bengal to cyclone phailin. *Journal of Physical Oceanography*, 49(5):1121–1140.
- Chavez, F., Strutton, P., Friederich, G., Feely, R., Feldman, G., Foley, D., and McPhaden, M. (1999). Biological and chemical response of the equatorial Pacific Ocean to the 1997-98 el niño. *Science*, 286(5447):2126–2131.
- Cherian, D., Shroyer, E., Wijesekera, H., and Moum, J. (2020). The seasonal cycle of upper-ocean mixing at 8N in the Bay of Bengal. *Journal of Physical Oceanography*, 50(2):323–342.
- Cherubini, S. and De Palma, P. (2013). Nonlinear optimal perturbations in a couette flow: bursting and transition. *Journal of Fluid Mechanics*, 716:251–279.
- Cherubini, S., De Palma, P., Robinet, J.-C., and Bottaro, A. (2010). Rapid path to transition via nonlinear localized optimal perturbations in a boundary-layer flow. *Physical Review E*, 82(6):066302.
- Cherubini, S., De Palma, P., Robinet, J.-C., and Bottaro, A. (2011). The minimal seed of turbulent transition in the boundary layer. *Journal of Fluid Mechanics*, 689:221–253.
- Chiang, T.-L., Wu, C.-R., and Oey, L.-Y. (2011). Typhoon Kai-Tak: An ocean’s perfect storm. *Journal of Physical Oceanography*, 41(1):221–233.
- Chikkadi, V., Sameen, A., and Govindarajan, R. (2005). Preventing transition to turbulence: A viscosity stratification does not always help. *Physical Review Letters*, 95(26):264504.

- Corrsin, S. (1951). On the spectrum of isotropic temperature fluctuations in an isotropic turbulence. *Journal of Applied Physics*, 22(4):469–473.
- Dabiri, J. O. (2010). Role of vertical migration in biogenic ocean mixing. *Geophysical Research Letters*, 37(11).
- D’Asaro, E. A. (2003). The ocean boundary layer below Hurricane Dennis. *Journal of Physical Oceanography*, 33(3):561–579.
- Davidson, P. A. (2013). *Turbulence in rotating, stratified and electrically conducting fluids*. Cambridge University Press.
- Dennis Jr, J. E. and Schnabel, R. B. (1996). *Numerical methods for unconstrained optimization and nonlinear equations*. SIAM.
- Di Prima, R. and Habetler, G. (1969). A completeness theorem for non-selfadjoint eigenvalue problems in hydrodynamic stability. *Archive for Rational Mechanics and Analysis*, 34(3):218–227.
- Dillon, T. M. and Caldwell, D. R. (1980). The Batchelor spectrum and dissipation in the upper ocean. *Journal of Geophysical Research: Oceans*, 85(C4):1910–1916.
- Durski, S. M., Glenn, S. M., and Haidvogel, D. B. (2004). Vertical mixing schemes in the coastal ocean: Comparison of the level 2.5 Mellor-Yamada scheme with an enhanced version of the K profile parameterization. *Journal of Geophysical Research: Oceans*, 109(C1).
- Eckhardt, B., Schneider, T. M., Hof, B., and Westerweel, J. (2007). Turbulence transition in pipe flow. *Annu. Rev. Fluid Mech.*, 39:447–468.
- Egbert, G. and Ray, R. (2000). Significant dissipation of tidal energy in the deep ocean inferred from satellite altimeter data. *Nature*, 405(6788):775–778.
- Ekman, V. W. (1905). On the influence of the earth’s rotation on ocean-currents.
- Ellingsen, T. and Palm, E. (1975). Stability of linear flow. *The Physics of Fluids*, 18(4):487–488.
- Emanuel, K. (2003). Tropical cyclones. *Annual review of earth and planetary sciences*, 31(1):75–104.
- Fairall, C. W., Bradley, E. F., Hare, J. E., Grachev, A. A., and Edson, J. B. (2003). Bulk parameterization of air-sea fluxes: Updates and verification for the COARE algorithm. *Journal of Climate*, 16(4):571–591.

- Foures, D., Caulfield, C., and Schmid, P. (2013). Localization of flow structures using  $\infty$ -norm optimization. *Journal of Fluid Mechanics*, 729:672–701.
- Foures, D., Caulfield, C., and Schmid, P. J. (2014). Optimal mixing in two-dimensional plane Poiseuille flow at finite Péclet number. *Journal of Fluid Mechanics*, 748:241–277.
- Fourier, J. B. J. (1822). *Théorie analytique de la chaleur*. F. Didot.
- Gaspar, P., Grégoris, Y., and Lefevre, J.-M. (1990). A simple eddy kinetic energy model for simulations of the oceanic vertical mixing: Tests at station papa and long-term upper ocean study site. *Journal of Geophysical Research: Oceans*, 95(C9):16179–16193.
- Gibson, C. and Schwarz, W. (1963). The universal equilibrium spectra of turbulent velocity and scalar fields. *Journal of Fluid Mechanics*, 16(3):365–384.
- Gibson, C. H. (1968). Fine structure of scalar fields mixed by turbulence. i. zero-gradient points and minimal gradient surfaces. *The Physics of Fluids*, 11(11):2305–2315.
- Godfrey, J. and Lindstrom, E. (1989). The heat budget of the equatorial western Pacific surface mixed layer. *Journal of Geophysical Research: Oceans*, 94(C6):8007–8017.
- Gordon, A. L., Shroyer, E., and Murty, V. (2017). An Intrathermocline Eddy and a tropical cyclone in the Bay of Bengal. *Scientific Reports*, 7:46218.
- Govindarajan, R. (2004). Effect of miscibility on the linear instability of two-fluid channel flow. *International Journal of Multiphase Flow*, 30(10):1177–1192.
- Govindarajan, R. and Sahu, K. C. (2014). Instabilities in viscosity-stratified flow. *Annual Review of Fluid Mechanics*, 46:331–353.
- Grant, H., Moilliet, A., and Stewart, R. (1959). A spectrum of turbulence at very high Reynolds number. *Nature*, 184(4689):808–810.
- Grant, H., Moilliet, A., and Vogel, W. (1968). Some observations of the occurrence of turbulence in and above the thermocline. *Journal of Fluid Mechanics*, 34(3):443–448.
- Grant, H., Stewart, R., and Moilliet, A. (1962). Turbulence spectra from a tidal channel. *Journal of Fluid Mechanics*, 12(2):241–268.
- Gregg, M. (1987). Diapycnal mixing in the thermocline: A review. *Journal of Geophysical Research: Oceans*, 92(C5):5249–5286.
- Gregg, M. (1989). Scaling turbulent dissipation in the thermocline. *Journal of Geophysical Research: Oceans*, 94(C7):9686–9698.
- Gregg, M., D’Asaro, E., Riley, J., and Kunze, E. (2018). Mixing efficiency in the ocean.

- Annual Review of Marine Science*, 10:443–473.
- Gregg, M. and Meagher, T. (1980). The dynamic response of glass rod thermistors. *Journal of Geophysical Research: Oceans*, 85(C5):2779–2786.
- Hallberg, R. and Gnanadesikan, A. (2006). The role of eddies in determining the structure and response of the wind-driven Southern Hemisphere overturning: Results from the Modeling Eddies in the Southern Ocean (MESO) project. *Journal of Physical Oceanography*, 36(12):2232–2252.
- Hamilton, J. M., Kim, J., and Waleffe, F. (1995). Regeneration mechanisms of near-wall turbulence structures. *Journal of Fluid Mechanics*, 287:317–348.
- Hayes, S., Mangum, L., Picaut, J., Sumi, A., and Takeuchi, K. (1991). TOGA-TAO: A moored array for real-time measurements in the tropical Pacific Ocean. *Bulletin of the American Meteorological Society*, 72(3):339–347.
- Held, I. M. (1985). Pseudomomentum and the orthogonality of modes in shear flows. *Journal of the atmospheric sciences*, 42(21):2280–2288.
- Henningson, D. S., Lundbladh, A., and Johansson, A. V. (1993). A mechanism for bypass transition from localized disturbances in wall-bounded shear flows. *Journal of Fluid Mechanics*, 250:169–207.
- Hill, D. (1995). Adjoint systems and their role in the receptivity problem for boundary layers. *Journal of Fluid Mechanics*, 292:183–204.
- Hopf, E. (1948). A mathematical example displaying features of turbulence. *Communications on Pure and Applied Mathematics*, 1(4):303–322.
- Hosom, D. S., Weller, R. A., Payne, R. E., and Prada, K. E. (1995). The IMET (Improved Meteorology) ship and buoy systems. *Journal of Atmospheric and Oceanic Technology*, 12(3):527–540.
- Hoyos, C. D. and Webster, P. J. (2007). The role of intraseasonal variability in the nature of Asian monsoon precipitation. *Journal of Climate*, 20(17):4402–4424.
- Hughes, K. G., Moum, J. N., and Shroyer, E. L. (2020). Evolution of the velocity structure in the diurnal warm layer. *Journal of Physical Oceanography*, 50(3):615–631.
- Ivey, G., Winters, K., and Koseff, J. (2008). Density stratification, turbulence, but how much mixing? *Annu. Rev. Fluid Mech.*, 40:169–184.
- Jensen, T. G. (2003). Cross-equatorial pathways of salt and tracers from the north-

- ern Indian Ocean: Modelling results. *Deep Sea Research Part II: Topical Studies in Oceanography*, 50(12-13):2111–2127.
- Jiménez, J. (2013). How linear is wall-bounded turbulence? *Physics of Fluids*, 25(11):110814.
- Johnson, G. C., McPhaden, M. J., and Firing, E. (2001). Equatorial Pacific Ocean horizontal velocity, divergence, and upwelling. *Journal of Physical Oceanography*, 31(3):839–849.
- Jose, S., Brandt, L., and Govindarajan, R. (2020). Localisation of optimal perturbations in variable viscosity channel flow. *International Journal of Heat and Fluid Flow*, 85:108588.
- Kaminski, A., Caulfield, C., and Taylor, J. (2014). Transient growth in strongly stratified shear layers. *Journal of Fluid Mechanics*, 758.
- Kaminski, A., Caulfield, C., and Taylor, J. (2017). Nonlinear evolution of linear optimal perturbations of strongly stratified shear layers. *Journal of Fluid Mechanics*, 825:213–244.
- Kelvin, L. (1887). Stability of fluid motion: rectilinear motion of viscous fluid between two parallel plates. *Phil. Mag*, 24(5):188–196.
- Kerswell, R. (2005). Recent progress in understanding the transition to turbulence in a pipe. *Nonlinearity*, 18(6):R17.
- Kerswell, R. (2018). Nonlinear nonmodal stability theory. *Annual Review of Fluid Mechanics*, 50:319–345.
- Klymak, J. M. and Moum, J. N. (2007). Oceanic isopycnal slope spectra. Part II: Turbulence. *Journal of Physical Oceanography*, 37(5):1232–1245.
- Kolmogorov, A. N. (1941). The local structure of turbulence in incompressible viscous fluid for very large reynolds numbers. *Cr Acad. Sci. URSS*, 30:301–305.
- Kraichnan, R. H. (1968). Small-scale structure of a scalar field convected by turbulence. *The Physics of Fluids*, 11(5):945–953.
- Kühnen, J., Song, B., Scarselli, D., Budanur, N. B., Riedl, M., Willis, A. P., Avila, M., and Hof, B. (2018). Destabilizing turbulence in pipe flow. *Nature Physics*, 14(4):386–390.
- Kundu, P. and Cohen, L. (1990). Fluid mechanics, 638 pp. *Academic, Calif.*

- Kunze, E. (2019). Biologically generated mixing in the ocean. *Annual Review of Marine Science*, 11:215–226.
- Kunze, E., Dower, J. F., Beveridge, I., Dewey, R., and Bartlett, K. P. (2006). Observations of biologically generated turbulence in a coastal inlet. *Science*, 313(5794):1768–1770.
- Kunze, E. and Toole, J. M. (1997). Tidally driven vorticity, diurnal shear, and turbulence atop Fieberling Seamount. *Journal of Physical Oceanography*, 27(12):2663–2693.
- Lamb, K. G. (2004). Nonlinear interaction among internal wave beams generated by tidal flow over supercritical topography. *Geophysical Research Letters*, 31(9).
- Landahl, M. (1980). A note on an algebraic instability of inviscid parallel shear flows. *Journal of Fluid Mechanics*, 98(2):243–251.
- Large, W. G., McWilliams, J. C., and Doney, S. C. (1994). Oceanic vertical mixing: A review and a model with a nonlocal boundary layer parameterization. *Reviews of Geophysics*, 32(4):363–403.
- Lee, J., Jung, S. Y., Sung, H. J., and Zaki, T. A. (2013). Effect of wall heating on turbulent boundary layers with temperature-dependent viscosity. *Journal of Fluid Mechanics*, 726:196–225.
- Legg, S. and Huijts, K. M. (2006). Preliminary simulations of internal waves and mixing generated by finite amplitude tidal flow over isolated topography. *Deep Sea Research Part II: Topical Studies in Oceanography*, 53(1-2):140–156.
- Leipper, D. F. (1967). Observed ocean conditions and Hurricane Hilda, 1964. *Journal of the Atmospheric Sciences*, 24(2):182–186.
- Levitus, S., Antonov, J. I., Boyer, T. P., and Stephens, C. (2000). Warming of the world ocean. *Science*, 287(5461):2225–2229.
- Li, Y., Han, W., Ravichandran, M., Wang, W., Shinoda, T., and Lee, T. (2017). Bay of Bengal salinity stratification and Indian summer monsoon intraseasonal oscillation: 1. Intraseasonal variability and causes. *Journal of Geophysical Research: Oceans*, 122(5):4291–4311.
- Lilly, J. M. and Olhede, S. C. (2010). On the analytic wavelet transform. *IEEE Transactions on Information Theory*, 56(8):4135–4156.
- Lilly, J. M. and Olhede, S. C. (2012). Generalized Morse wavelets as a superfamily of analytic wavelets. *IEEE Transactions on Signal Processing*, 60(11):6036–6041.

- Luchini, P. and Bottaro, A. (2014). Adjoint equations in stability analysis. *Annual Review of Fluid Mechanics*, 46.
- Mack, L. M. (1984). Boundary-layer linear stability theory. *AGARD Report No. 709*.
- MacKinnon, J., Alford, M., Pinkel, R., Klymak, J., and Zhao, Z. (2013). The latitudinal dependence of shear and mixing in the Pacific transiting the critical latitude for PSI. *Journal of Physical Oceanography*, 43(1):3–16.
- Marcotte, F. and Caulfield, C. (2018). Optimal mixing in two-dimensional stratified plane Poiseuille flow at finite Péclet and Richardson numbers. *Journal of Fluid Mechanics*, 853:359–385.
- Mater, B. D. and Venayagamoorthy, S. K. (2014). The quest for an unambiguous parameterization of mixing efficiency in stably stratified geophysical flows. *Geophysical Research Letters*, 41(13):4646–4653.
- McDougall, T. J. and Barker, P. M. (2011). Getting started with TEOS-10 and the Gibbs Seawater (GSW) oceanographic toolbox. *SCOR/IAPSO WG*, 127:1–28.
- McPhaden, M. and Foltz, G. (2013). Intraseasonal variations in the surface layer heat balance of the central equatorial Indian Ocean: The importance of zonal advection and vertical mixing. *Geophysical Research Letters*, 40(11):2737–2741.
- McPhaden, M. J. (1999). Genesis and evolution of the 1997-98 El Niño. *Science*, 283(5404):950–954.
- McPhaden, M. J., Busalacchi, A. J., Cheney, R., Donguy, J.-R., Gage, K. S., Halpern, D., Ji, M., Julian, P., Meyers, G., Mitchum, G. T., et al. (1998). The Tropical Ocean-Global Atmosphere observing system: A decade of progress. *Journal of Geophysical Research: Oceans*, 103(C7):14169–14240.
- Mcphaden, M. J., Meyers, G., Ando, K., Masumoto, Y., Murty, V., Ravichandran, M., Syamsudin, F., Vialard, J., Yu, L., and Yu, W. (2009). RAMA: the research moored array for African–Asian–Australian monsoon analysis and prediction. *Bulletin of the American Meteorological Society*, 90(4):459–480.
- Melet, A., Hallberg, R., Legg, S., and Polzin, K. (2013). Sensitivity of the ocean state to the vertical distribution of internal-tide-driven mixing. *Journal of Physical Oceanography*, 43(3):602–615.
- Monismith, S. G., Koseff, J. R., and White, B. L. (2018). Mixing efficiency in the presence

- of stratification: When is it constant? *Geophysical Research Letters*, 45(11):5627–5634.
- Monokrousos, A., Bottaro, A., Brandt, L., Di Vita, A., and Henningson, D. S. (2011). Nonequilibrium thermodynamics and the optimal path to turbulence in shear flows. *Physical Review Letters*, 106(13):134502.
- Moore, A. M. and Kleeman, R. (1999). Stochastic forcing of ENSO by the intraseasonal oscillation. *Journal of Climate*, 12(5):1199–1220.
- Moulin, A. J., Moum, J. N., and Shroyer, E. L. (2018). Evolution of turbulence in the diurnal warm layer. *Journal of Physical Oceanography*, 48(2):383–396.
- Moum, J. N. (1990). Profiler measurements of vertical velocity fluctuations in the ocean. *Journal of Atmospheric and Oceanic Technology*, 7(2):323–333.
- Moum, J. N. (2015). Ocean speed and turbulence measurements using Pitot-static tubes on moorings. *Journal of Atmospheric and Oceanic Technology*, 32(7):1400–1413.
- Moum, J. N. (2020). Variations in ocean mixing from seconds to years. *Annual Review of Marine Science*, 13.
- Moum, J. N., de Szoeke, S. P., Smyth, W. D., Edson, J. B., DeWitt, H. L., Moulin, A. J., Thompson, E. J., Zappa, C. J., Rutledge, S. A., Johnson, R. H., et al. (2014). Air-sea interactions from westerly wind bursts during the November 2011 MJO in the Indian Ocean. *Bulletin of the American Meteorological Society*, 95(8):1185–1199.
- Moum, J. N. and Nash, J. D. (2009). Mixing measurements on an equatorial ocean mooring. *Journal of Atmospheric and Oceanic Technology*, 26(2):317–336.
- Moum, J. N., Perlin, A., Nash, J. D., and McPhaden, M. J. (2013). Seasonal sea surface cooling in the equatorial Pacific cold tongue controlled by ocean mixing. *Nature*, 500(7460):64–67.
- Munk, W. H. (1966). Abyssal recipes. In *Deep Sea Research and Oceanographic Abstracts*, volume 13, pages 707–730. Elsevier.
- Narasimha, R. (1983). Relaminarization—magnetohydrodynamic and otherwise. *AIAA Progress in Astronautics and Aeronautics*, 84:30–52.
- Narasimha, R. and Sreenivasan, K. (1979). Relaminarization of fluid flows. In *Advances in Applied Mechanics*, volume 19, pages 221–309. Elsevier.
- Nash, J. D., Kunze, E., Toole, J. M., and Schmitt, R. W. (2004). Internal tide reflection and turbulent mixing on the continental slope. *Journal of Physical Oceanography*,

- 34(5):1117–1134.
- Obukhov, A. (1941). On the distribution of energy in the spectrum of turbulent flow. In *Dokl. Akad. Nauk SSSR*, volume 32, pages 22–24.
- Obukhov, A. (1949). Structure of the temperature field in turbulent flows. *Dokl. Akad. Nauk. SSSR*, 39.
- Orr, W. M. (1907). The stability or instability of the steady motions of a perfect liquid and of a viscous liquid. Part II: A viscous liquid. In *Proceedings of the Royal Irish Academy. Section A: Mathematical and Physical Sciences*, volume 27, pages 69–138.
- Orszag, S. A. (1971). Accurate solution of the Orr-Sommerfeld stability equation. *Journal of Fluid Mechanics*, 50(4):689–703.
- Osborn, T. and Crawford, W. (1980). An airfoil probe for measuring turbulent velocity fluctuations in water. In *Air-Sea Interaction*, pages 369–386. Springer.
- Osborn, T. R. (1980). Estimates of the local rate of vertical diffusion from dissipation measurements. *Journal of Physical Oceanography*, 10(1):83–89.
- Osborn, T. R. and Cox, C. S. (1972). Oceanic fine structure. *Geophysical & Astrophysical Fluid Dynamics*, 3(1):321–345.
- Osborn, T. R. and Lueck, R. G. (1985a). Turbulence measurements from a towed body. *Journal of Atmospheric and Oceanic Technology*, 2(4):517–527.
- Osborn, T. R. and Lueck, R. G. (1985b). Turbulence measurements with a submarine. *Journal of Physical Oceanography*, 15(11):1502–1520.
- Perlin, A. and Moum, J. N. (2012). Comparison of thermal variance dissipation rates from moored and profiling instruments at the equator. *Journal of Atmospheric and Oceanic Technology*, 29(9):1347–1362.
- Polak, E. (1971). *Computational methods in optimization: a unified approach*, volume 77. Academic press.
- Polak, E. and Ribiere, G. (1969). Note sur la convergence de méthodes de directions conjuguées. *ESAIM: Mathematical Modelling and Numerical Analysis-Modélisation Mathématique et Analyse Numérique*, 3(R1):35–43.
- Polzin, K. L., Toole, J. M., and Schmitt, R. W. (1995). Finescale parameterizations of turbulent dissipation. *Journal of Physical Oceanography*, 25(3):306–328.
- Pope, S. (2000). *Turbulent Flows*. Cambridge University Press.

- Potter, M. C. and Graber, E. (1972). Stability of plane Poiseuille flow with heat transfer. *The Physics of Fluids*, 15(3):387–391.
- Prasanna Kumar, S., Muraleedharan, P., Prasad, T., Gauns, M., Ramaiah, N., De Souza, S., Sardesai, S., and Madhupratap, M. (2002). Why is the Bay of Bengal less productive during summer monsoon compared to the Arabian Sea? *Geophysical Research Letters*, 29(24):88–1.
- Preziosi, L., Chen, K., and Joseph, D. D. (1989). Lubricated pipelining: stability of core-annular flow. *Journal of Fluid Mechanics*, 201:323–356.
- Pringle, C. C. and Kerswell, R. R. (2010). Using nonlinear transient growth to construct the minimal seed for shear flow turbulence. *Physical Review Letters*, 105(15):154502.
- Pringle, C. C., Willis, A. P., and Kerswell, R. R. (2012). Minimal seeds for shear flow turbulence: using nonlinear transient growth to touch the edge of chaos. *Journal of Fluid Mechanics*, 702:415–443.
- Pujiana, K., Moum, J. N., and Smyth, W. D. (2018). The role of turbulence in redistributing upper-ocean heat, freshwater, and momentum in response to the MJO in the Equatorial Indian Ocean. *Journal of Physical Oceanography*, 48(1):197–220.
- Pujiana, K., Moum, J. N., Smyth, W. D., and Warner, S. J. (2015). Distinguishing ichthyogenic turbulence from geophysical turbulence. *Journal of Geophysical Research: Oceans*, 120(5):3792–3804.
- Rabin, S., Caulfield, C., and Kerswell, R. (2012). Triggering turbulence efficiently in plane Couette flow. *Journal of Fluid Mechanics*, 712:244–272.
- Rahaman, H., Ravichandran, M., Sengupta, D., Harrison, M. J., and Griffies, S. M. (2014). Development of a regional model for the North Indian Ocean. *Ocean Modelling*, 75:1–19.
- Ranganathan, B. T. and Govindarajan, R. (2001). Stabilization and destabilization of channel flow by location of viscosity-stratified fluid layer. *Physics of Fluids*, 13(1):1–3.
- Ray, R. D. and Mitchum, G. T. (1996). Surface manifestation of internal tides generated near Hawaii. *Geophysical Research Letters*, 23(16):2101–2104.
- Rayleigh, L. (1880). On the stability, or instability, of certain fluid motions. *Proc. London Math. Soc.*, 9:57–70.
- Rayleigh, L. (1916). LIX. on convection currents in a horizontal layer of fluid, when

- the higher temperature is on the under side. *The London, Edinburgh, and Dublin Philosophical Magazine and Journal of Science*, 32(192):529–546.
- Reddy, S. C. and Henningson, D. S. (1993). Energy growth in viscous channel flows. *Journal of Fluid Mechanics*, 252:209–238.
- Reddy, S. C., Schmid, P. J., Baggett, J. S., and Henningson, D. S. (1998). On stability of streamwise streaks and transition thresholds in plane channel flows. *Journal of Fluid Mechanics*, 365:269–303.
- Reddy, S. C., Schmid, P. J., and Henningson, D. S. (1993). Pseudospectra of the Orr-Sommerfeld operator. *SIAM Journal on Applied Mathematics*, 53(1):15–47.
- Reynolds, O. (1883). XXIX. An experimental investigation of the circumstances which determine whether the motion of water shall be direct or sinuous, and of the law of resistance in parallel channels. *Philosophical Transactions of the Royal Society of London*, (174):935–982.
- Rudnick, D. L., Boyd, T. J., Brainard, R. E., Carter, G. S., Egbert, G. D., Gregg, M. C., Holloway, P. E., Klymak, J. M., Kunze, E., Lee, C. M., et al. (2003). From tides to mixing along the Hawaiian Ridge. *Science*, 301(5631):355–357.
- Rudnick, D. L., Davis, R. E., Eriksen, C. C., Fratantoni, D. M., and Perry, M. J. (2004). Underwater gliders for ocean research. *Marine Technology Society Journal*, 38(2):73–84.
- Saji, N., Goswami, B., Vinayachandran, P., and Yamagata, T. (1999). A dipole mode in the tropical Indian Ocean. *Nature*, 401(6751):360–363.
- Sameen, A. and Govindarajan, R. (2007). The effect of wall heating on instability of channel flow. *Journal of Fluid Mechanics*, 577:417–442.
- Schäfer, P. and Herwig, H. (1993). Stability of plane Poiseuille flow with temperature dependent viscosity. *International Journal of Heat and Mass transfer*, 36(9):2441–2448.
- Schlichting, H. (1933). Berechnung der Anfachung kleiner störungen bei der Plattenströmung. *ZAMM*, 13(171-174):50.
- Schmid, P. J. (2007). Nonmodal stability theory. *Annual Review of Fluid Mechanics*, 39:129–162.
- Schmid, P. J. and Brandt, L. (2014). Analysis of fluid systems: Stability, receptivity, sensitivity. lecture notes from the flow-Nordita summer school on advanced instability

- methods for complex flows, Stockholm, Sweden, 2013. *Applied Mechanics Reviews*, 66(2).
- Schmid, P. J., Henningson, D. S., and Jankowski, D. (2002). Stability and transition in shear flows. *Applied mathematical sciences*, vol. 142. *Appl. Mech. Rev.*, 55(3):B57–B59.
- Schott, F. A., Xie, S.-P., and McCreary Jr, J. P. (2009). Indian ocean circulation and climate variability. *Reviews of Geophysics*, 47(1).
- Sengupta, D., Bharath Raj, G., and Shenoi, S. (2006). Surface freshwater from Bay of Bengal runoff and Indonesian throughflow in the tropical Indian Ocean. *Geophysical Research Letters*, 33(22).
- Sengupta, D., Goswami, B., and Senan, R. (2001). Coherent intraseasonal oscillations of ocean and atmosphere during the Asian summer monsoon. *Geophysical Research Letters*, 28(21):4127–4130.
- Sengupta, D. and Ravichandran, M. (2001). Oscillations of Bay of Bengal sea surface temperature during the 1998 summer monsoon. *Geophysical Research Letters*, 28(10):2033–2036.
- Sengupta, D., Senan, R., Goswami, B., and Vialard, J. (2007). Intraseasonal variability of equatorial Indian Ocean zonal currents. *Journal of Climate*, 20(13):3036–3055.
- Servain, J., Busalacchi, A. J., McPhaden, M. J., Moura, A. D., Reverdin, G., Vianna, M., and Zebiak, S. E. (1998). A pilot research moored array in the tropical Atlantic (PIRATA). *Bulletin of the American Meteorological Society*, 79(10):2019–2032.
- Shay, T. J. and Gregg, M. (1986). Convectively driven turbulent mixing in the upper ocean. *Journal of Physical Oceanography*, 16(11):1777–1798.
- Shroyer, E. L., Nash, J. D., Waterhouse, A. F., and Moum, J. N. (2018). Measuring ocean turbulence. In *Observing the Oceans in Real Time*, pages 99–122. Springer.
- Shroyer, E. L., Rudnick, D. L., Farrar, J. T., Lim, B., Venayagamoorthy, S. K., St. Laurent, L. C., Garanaik, A., and Moum, J. N. (2016). Modification of upper-ocean temperature structure by subsurface mixing in the presence of strong salinity stratification. *Oceanography*, 29(2):62–71.
- Sikka, D. and Gadgil, S. (1980). On the maximum cloud zone and the ITCZ over Indian longitudes during the southwest monsoon. *Monthly Weather Review*, 108(11):1840–1853.

- Smyth, W., Moum, J., Li, L., and Thorpe, S. (2013). Diurnal shear instability, the descent of the surface shear layer, and the deep cycle of equatorial turbulence. *Journal of Physical Oceanography*, 43(11):2432–2455.
- Sommerfeld, A. (1908). Ein beitrage zur hydrodynamischen erklärung der turbulenten flussigkeitsbewegung. *Atti Congr. Int. Math. 4th*.
- Sree Lekha, J., Buckley, J., Tandon, A., and Sengupta, D. (2018). Subseasonal dispersal of freshwater in the northern Bay of Bengal in the 2013 summer monsoon season. *Journal of Geophysical Research: Oceans*.
- Sreenivasan, K. R. (1996). The passive scalar spectrum and the Obukhov-Corrsin constant. *Physics of Fluids*, 8(1):189–196.
- Stacey, M. T., Monismith, S. G., and Burau, J. R. (1999). Observations of turbulence in a partially stratified estuary. *Journal of Physical Oceanography*, 29(8):1950–1970.
- Stommel, H. and Fedorov, K. (1967). Small scale structure in temperature and salinity near timor and mindanao. *Tellus*, 19(2):306–325.
- Sutherland, G., Marié, L., Reverdin, G., Christensen, K. H., Broström, G., and Ward, B. (2016). Enhanced turbulence associated with the diurnal jet in the ocean surface boundary layer. *Journal of Physical Oceanography*, 46(10):3051–3067.
- Taylor, G. I. (1938). The spectrum of turbulence. *Proceedings of the Royal Society of London A: Mathematical, Physical and Engineering Sciences*, 164:476–490.
- Taylor, J. R. (2008). *Numerical simulations of the stratified oceanic bottom boundary layer*. PhD thesis, UC San Diego.
- Tennekes, H. and Lumley, J. L. (2018). *A first course in turbulence*. MIT press.
- Thakur, R., Shroyer, E. L., Govindarajan, R., Farrar, J. T., Weller, R. A., and Moum, J. N. (2019). Seasonality and buoyancy suppression of turbulence in the Bay of Bengal. *Geophysical Research Letters*, 46(8):4346–4355.
- Thomas, L. N., Tandon, A., and Mahadevan, A. (2008). Submesoscale processes and dynamics. *Ocean modeling in an Eddying Regime*, pages 17–38.
- Tollmien, W. (1930). Über die entstehung der turbulenz. In *Vorträge aus dem Gebiete der Aerodynamik und verwandter Gebiete*, pages 18–21. Springer.
- Trefethen, L. N. and Embree, M. (2005). *Spectra and pseudospectra: the behavior of nonnormal matrices and operators*. Princeton University Press.

- Trefethen, L. N., Trefethen, A. E., Reddy, S. C., and Driscoll, T. A. (1993). Hydrodynamic stability without eigenvalues. *Science*, 261(5121):578–584.
- Tuckerman, L. S., Kreilos, T., Schrobsdorff, H., Schneider, T. M., and Gibson, J. F. (2014). Turbulent-laminar patterns in plane Poiseuille flow. *Physics of Fluids*, 26(11):114103.
- Varma, D. and Mathur, M. (2017). Internal wave resonant triads in finite-depth non-uniform stratifications. *Journal of Fluid Mechanics*, 824:286–311.
- Vavaliaris, C., Beneitez, M., and Henningson, D. S. (2020). Optimal perturbations and transition energy thresholds in boundary layer shear flows. *Phys. Rev. Fluids*, 5:062401.
- Vermach, L. and Caulfield, C. (2018). Optimal mixing in three-dimensional plane Poiseuille flow at high Péclet number. *Journal of Fluid Mechanics*, 850:875–923.
- Vincent, E. M., Lengaigne, M., Madec, G., Vialard, J., Samson, G., Jourdain, N. C., Menkes, C. E., and Jullien, S. (2012). Processes setting the characteristics of sea surface cooling induced by tropical cyclones. *Journal of Geophysical Research: Oceans*, 117(C2).
- Waleffe, F. (1997). On a self-sustaining process in shear flows. *Physics of Fluids*, 9(4):883–900.
- Waleffe, F. (2009). Exact coherent structures in turbulent shear flows. In *Turbulence and Interactions*, pages 139–158. Springer.
- Wall, D. and Wilson, S. (1996). The linear stability of channel flow of fluid with temperature-dependent viscosity. *Journal of Fluid Mechanics*, 323:107–132.
- Wang, D., McWilliams, J. C., and Large, W. G. (1998). Large-eddy simulation of the diurnal cycle of deep equatorial turbulence. *Journal of Physical Oceanography*, 28(1):129–148.
- Warner, S. J., Becherer, J., Pujiana, K., Shroyer, E. L., Ravichandran, M., Thangaprakash, V., and Moum, J. N. (2016). Monsoon mixing cycles in the Bay of Bengal: A year-long subsurface mixing record. *Oceanography*, 29(2):158–169.
- Warner, S. J. and Moum, J. N. (2019). Feedback of mixing to ENSO phase change. *Geophysical Research Letters*, 46(23):13920–13927.
- Weller, R., Farrar, J., Seo, H., Prend, C., Sengupta, D., Lekha, J. S., Ravichandran, M., and Venkatesen, R. (2019). Moored observations of the surface meteorology and

- air-sea fluxes in the northern bay of bengal in 2015. *Journal of Climate*, 32(2):549–573.
- Woods, J. (1968). Wave-induced shear instability in the summer thermocline. *Journal of Fluid Mechanics*, 32(4):791–800.
- Woolnough, S., Vitart, F., and Balmaseda, M. (2007). The role of the ocean in the Madden-Julian oscillation: Implications for MJO prediction. *Quarterly Journal of the Royal Meteorological Society*, 133(622):117–128.
- Wunsch, C. and Ferrari, R. (2004). Vertical mixing, energy, and the general circulation of the oceans. *Annu. Rev. Fluid Mech.*, 36:281–314.
- Yeung, P., Xu, S., and Sreenivasan, K. (2002). Schmidt number effects on turbulent transport with uniform mean scalar gradient. *Physics of Fluids*, 14(12):4178–4191.
- Yih, C.-S. (1967). Instability due to viscosity stratification. *Journal of Fluid Mechanics*, 27(02):337–352.
- Zonta, F., Marchioli, C., and Soldati, A. (2012). Modulation of turbulence in forced convection by temperature-dependent viscosity. *Journal of Fluid Mechanics*, 697:150–174.
- Zuccher, S., Luchini, P., and Bottaro, A. (2004). Algebraic growth in a Blasius boundary layer: optimal and robust control by mean suction in the nonlinear regime. *Journal of Fluid Mechanics*, 513:135–160.